The time-domain numerical solution of Maxwell's electromagnetic equations, via the fourth order Runge-Kutta discontinuous Galerkin method.

Boat, Matthew

The Time-Domain Numerical Solution of Maxwell's Electromagnetic Equations, via the Fourth Order Runge-Kutta Discontinuous Galerkin Method

Matthew Boat
Civil and Computational Engineering
University of Wales Swansea
Singleton Park
Swansea SA2 8PP
United Kingdom

April 2008

Summary

This thesis presents a high-order numerical method for the Time-Domain solution of Maxwell's Electromagnetic equations in both one- and two-dimensional space.

The thesis discuses the validity of high-order representation and improved boundary representation.

The majority of the theory is concerned with the formulation of a high-order scheme which is capable of providing a numerical solution for specific two-dimensional scattering problems.

Specifics of the theory involve the selection of a suitable numerical flux, the choice of appropriate boundary conditions, mapping between coordinate systems and basis functions.

The effectiveness of the method is then demonstrated through a series of examples.

Acknowledgements

I would like to write a few personal lines thanking the people who allowed me to get to this situation. The first thanks has to go to my teacher Professor Ken Morgan, who has showed me great patience and helped me whenever he could. I must also thank Professor O. Hassan and Dr P. Ledger for their help.

Swansea University, as a whole, provided me with invaluable support, and I would like to thank the University for its support over the years. I must also thank BAE systems and EPSRC for their monetary support.

I would also like to pay a special thank you to Pat and Bernard for their continual help and support and all of my family. And Lisa, my love, a special thank-you to you, for being with me. Thanks all.

Contents

List of Figures

Chapter 1

Introduction

1.1 Background

Electromagnetic theory, in all its forms, has captivated many of the great minds, including such luminaries as Descartes, Newton and Albert Einstein.

The mathematical theory associated with electromagnetism consists of a set of equations accredited to Maxwell. The Maxwell equations govern the flow of electromagnetic phenomena. Solutions to the equation set allow for an understanding of many physical, real life occurrences.

Michael Faraday (1791-1867) is attributed with the discovery that electromagnetic forces are generated by fields originating from charged objects [1]. Further to Faraday's discovery, James Clerk Maxwell (1831-1879) established that electromagnetic disturbances, emitted from a source, traveled in a form that can be regarded as having wave like properties. The combination of these theories resulted in a set of equations termed the Maxwell equations.

The above describes a very brief summary of classical electromagnetic theory, conducted primarily in the 19th century. What is electromagnetism? There are various forms of electromagnetic waves; x-rays, television-rays, microwaves and light are all types of electromagnetic wave, differing only with respect to the magnitude of the wavelength associated with the propagating wave. The wide ranging implications of electromagnetic waves is thus clearly apparent.

It has now been realised that the implications of electromagnetism are more widespread than first thought, to illustrate consider some of the following, modern, applications.

Communication in most forms, varying from mobile phones to television to military purposes, is dependent upon antennae. Antennae are employed for transmitting electromagnetic waves and are often seen in highly visible areas so that no obstacles interfere with the waves. Should this interference occur then the electromagnetic wave becomes scattered.

The ability to provide an electronic system that is impervious to the interference provided by other electronic devises (as exhibited on airplanes, when mobile phones are required to be switched off) will greatly enhance the design capabilities of systems.

Of interest to the medical world is the absorption of electromagnetic waves. Consider the fact that the obstacle of interference is a human brain, then it becomes desirable to find the effects, if any, of absorbing the waves.

The detection of objects, via electromagnetic waves, is also possible and prevalent to this thesis. In this employment, the waves can be used to find objects varying from land mines to ancient cities. A closely linked application is radar. The ability to find and track military objects is of great importance to defence agencies. The radar profile of an object emerges from the scattering of an electromagnetic wave. It is clearly important to have the ability to predict a profile to allow recognition. An opposing, but equally important skill, is the ability to minimise the radar profile observed.

It is, therefore, plain to see that electromagnetic theory has a massive bearing on day to day life and has many interesting and important applications.

1.2 Methods employed for the solution of electromagnetic problems

Generally, the electromagnetic problems encountered, for which a solution is of interest, are complex. The equation set that needs to be solved, requires the solution of a set of partial differential equations. An analytical solution to a set a partial differential equations is only available for a relatively small, relatively non-complex, set of problems. The possibility of an exact solution is further decreased by the appearance of either complex geometry or difficult, associated, boundary conditions. These two factors increase the complexity of the equations thereby making the equations harder to solve. The need to devise methods that provide accurate and efficient solutions to complex and diverse electromagnetic problems is a necessity.

Before the advent of numerical methods, experimental and theoretical procedures were the foremost methods employed to solve problems in electromagnetics. The problems that could be considered, using such traditional methods, were of a low complexity. Theoretical methods, by their nature, tend to be limited in application to problems which involve simple geometries. Experimental methods can be expensive and put constraints on the design cycle of a product.

To address these issues computational methods are now employed where relevant. By definition, computational methods yield only approximate solutions, however these methods provide fast and cheap solutions to problems.

At present a numerical scheme provides the best method with which to solve the problems associated with Maxwell's equations. The idea of employing such methods is that electromagnetic problems simulated upon a computer will provide fast, highly accurate, approximations to very complex problems.

Once numerical schemes have been decided upon, the analyst has many decisions to make. The two major concerns are accuracy of approximation and speed of computation. The analyst attempts to influence certain factors with the goal of controlling the accuracy and efficiency of the scheme.

Recent years have witnessed an increase in the speed of computation (facilitated by an impressive advancement in computer technology), whilst the accuracy of the approximation has seen improvement courtesy of improved domain representation and high-order approximation, amongst other factors. The accuracy of the results achieved via these numerical methods, is measured against existing exact analytical solutions.

One such area that requires the use of numerical methods for an adequate solution, is the calculation of the radar profile for electromagnetic scattering problem. The challenge presented by these problems is of great interest. For the frequencies of interest, the wavelength of the waves is extremely short when compared to the scatterer. So, even given the capabilities of the modern computer and today's computational techniques, this is still a problem of massive interest.

1.3 Numerical methods

Numerical methods are employed to supply approximate solutions to electromagnetic problems (amongst others). The use of numerical methods is now so widespread, that when numerical solutions to partial differential equations are sought, any newly devised scheme should offer an advantage over existing techniques. The improvement(s) may be exhibited in computational cost or in an increase in the accuracy of the scheme. The analyst, ever seeking improved solutions to Maxwell's equations via a numerical method, encounters many possibilities. Depending upon the method of approximation, certain requirements have to be strictly adhered to, which can limit the efficiency or accuracy of a scheme.

A numerical method that allows the practitioner room for manoeuver is the finite element method [2]. The finite element method was initially developed for use in the aerospace industry, to find the strains and stresses placed on an aircraft during flight. The correct application of the finite element method can provide highly accurate and computationally efficient approximate solutions to partial differential equations.

The fact that the finite element method yields approximate solutions to, say, Maxwell's equa-

tions, and that these solutions are acquired with the aid of computer technology, naturally infers that the practitioner will seek ever more efficient and accurate solutions. The continual advancement of applicable technology suggests that improvement may be achieved on two fronts: one a theoretical advancement of the numerical scheme, the other, improvement of existing technologies.

It is clear that the efficiency/computational cost, combined with the accuracy of the solution, is paramount to the implementation of a numerical scheme. These factors are of continual thought to the programmer. The concept of compromise, regarding cost, efficiency and accuracy, is therefore necessarily introduced. Generally, whilst considering numerical methods, improvement in one aspect tends to have an adverse consequence in another area. To exemplify consider a typical example of the compromise in numerical schemes when seeking a solution to Maxwell's equations: The numerical method employed may ably represent a complex solution domain, however the accurate representation of this domain may have adverse consequences for the efficiency of the scheme (due to the complex representation) and vice-versa. Hence a factor to consider when a numerical scheme is to be employed, is that any perceived improvements do not adversely affect the quality of the scheme in another area and thereby reduce the overall excellence of the scheme. Such considerations are not limited to such simplistic concepts as to which method to employ, they permeate throughout the numerical scheme and are inclusive of such topics as matrix inversion, choice of numerical integration etc. Therefore, care is need in all areas so that the practitioner does not err.

1.4 Computer Methods for Scattering Problems

At present, there exists a number of computer methods that can be employed to solve electromagnetic scattering problems. A most popular method is the finite difference (FD) method. The FD method is highly regarded due to the efficiency of a particular implementation, the Yee scheme [3]. The Yee scheme provides an extremely fast method capable of producing accurate solutions in the time domain. The method fails however when anything other than a pointwise approximation of the solution is required. Therefore, the method is unable to provide highly accurate solutions for complex geometries (which occur in real life situations).

In the frequency domain, high order elements [4] have provided a means for efficient modelling of multilayer structures. A recent trend has seen the employment of fast multipole techniques, another method that sees vast employment is the Method of Moments [5]. This method however becomes expensive in storage and CPU time for large scale problems . Although currently limited in application, fast multipole techniques show that large scale scattering simulations can be undertaken with available computer resources.

Clearly, an important consideration is the accuracy and reliability of the numerical scheme. To ensure accuracy and reliability, a large number of efficient and accurate error estimators have been developed. These estimators allow the quantification of the error for problems without analytical solutions (therefore of great interest).

1.5 Objective of the Thesis

The objective of this thesis is to present a new numerical method suitable for the numerical solution to Maxwell's electromagnetic equations in the time domain. In particular this thesis presents the implementation of a method suitable for the solution of Maxwell's equations in the time domain using a new boundary representation. The method employed for the solution of Maxwell's equations is called the Runge Kutta discontinuous Galerkin method (discussed in detail in chapter three).

The problems under consideration are in both one- and two-dimensional space. For the numerical scheme in two-dimensional space, only triangles comprise the solution domain. Using this method it is hoped that the scattering of large electromagnetic problems can be found with a high degree of accuracy. The method is to be detailed in the subsequent chapters.

1.6 Outline of Thesis

Brief detail is now given to describe the chapters present in this thesis.

- Chapter Two: This may be considered as an introductory chapter to the underlying mathematical procedures of electromagnetic theory.

- Chapter Three: This chapter discuses the fundamentals of the scheme to be employed for the solution of Maxwell's equations, raising issues such as approximating functions, and discretisation. The chapter concludes by discussing the numerical scheme that is to be employed.

- Chapter Four: Here the one-dimensional case is discussed, and the results obtained are presented and analysed.

- Chapter Five: The theory is now extended to consider two-dimensional problems involving the scattering of an electromagnetic wave, the results which accompany these problems are then considered.

- Chapter Six: A new method that truncates the infinite computational domain is presented. Also presented is the theory of blending. The results obtained from the imposition of these theories are then presented.

- Chapter Seven: The conclusion, and suggestions for further research, are presented.

Chapter 2

Preliminaries

2.1 Basic Electromagnetics

Maxwell's equations govern electromagnetic phenomena. The equations provide the relation between the electric and magnetic field intensity vectors $\boldsymbol{E}^*$ and $\boldsymbol{H}^*$. The equations also provide a relation between the fields and the properties of the medium in which they propagate. The full set of equations can be written as

$$\text{div } \mathbf{D}^* = \gamma^* \tag{2.1}$$

$$\text{div } \mathbf{B}^* = 0 \tag{2.2}$$

$$\text{curl } \mathbf{H}^* = \mathbf{J}_c^* + \frac{\partial \mathbf{D}^*}{\partial t} \tag{2.3}$$

$$\text{curl } \mathbf{E}^* = -\frac{\partial \mathbf{B}^*}{\partial t} \tag{2.4}$$

It remains to specify the constitutive equations and the equation that conserves charge, the latter formally known as the equation of continuity. These equations are represented by

$$\boldsymbol{D}^* = \epsilon^* \boldsymbol{E}^* \qquad \boldsymbol{B}^* = \mu^* \boldsymbol{H}^* \qquad \boldsymbol{J}^* = \sigma^* \boldsymbol{E}^* \tag{2.5}$$

$$\text{div } \mathbf{J}_c^* = -\frac{\partial \gamma^*}{\partial t} \tag{2.6}$$

where $\boldsymbol{B}^*$ is the magnetic flux density vector, $\boldsymbol{J}_c^*$ is the electric current density vector, $\boldsymbol{D}^*$ is the electric flux density vector and γ^* is the electric charge density. Here ϵ^*, μ^*, and σ^* represent the permittivity, permeability and conductivity of the medium respectively. The superscript $*$ indicates a

dimensional quantity.

A simplification of this governing set of equations is readily obtainable by making six basic assumptions. These assumptions take into consideration the nature of the materials that are to be examined. These assumptions are made throughout this thesis

- The electric charge density is zero, i.e. $\gamma^* = 0$;
- The materials are assumed to be non-lossy[1];
- Material conductivity is negligible, i.e. $\sigma^* = 0$;
- The permittivity and permeability do not vary in time;
- The medium obeys Ohm's Law $\boldsymbol{J}_c^* = \sigma^* \boldsymbol{E}^*$;
- Problems are considered in two space dimensions only[2].

With these assumptions, in conjunction with the constitutive relations, it can be shown that the governing equations may be re-written as

$$\text{curl } \mathbf{H}^* = \epsilon^* \frac{\partial \mathbf{E}^*}{\partial t} \tag{2.7}$$

$$\text{curl } \boldsymbol{E}^* = -\mu^* \frac{\partial \mathbf{H}^*}{\partial t} \tag{2.8}$$

$$\text{div } \epsilon^* \mathbf{E}^* = 0 \tag{2.9}$$

$$\text{div } \mu^* \mathbf{H}^* = 0 \tag{2.10}$$

This reduction of Maxwell's equations to two curl and two divergence equations, represents the form adopted to attempt an approximate numerical solution to given problems. The reduced set of equations now only involve expressions of the electric $\boldsymbol{E}^*$ and magnetic $\boldsymbol{H}^*$ field intensity vectors and two properties of the material. The numerical solution of these four equations is the goal of this thesis. It is assumed that the divergence equations are satisfied at some initiall time $t = 0$ [6].

2.1.1 Reduction to two-dimensional space

The representation of Maxwell's equations in an even more simplistic manner is of direct relevance to the problems encountered in Chapter Five. The equation set (2.7-2.10) can be reduced further

[1] no dissipation of electromagnetic energy

[2] This property is independent of the material assumption

if the solutions are sought in two spatial dimensions only. Determining approximate solutions in two-dimensional space suggests that a decomposition, in to transverse electric (TE) and transverse magnetic (TM) polarised waves, be considered.

In three dimensional space, the electric field is $\boldsymbol{E}^* = (E_x^*, E_y^*, E_z^*)$ relating to a Cartesian coordinate system. Similarly, the magnetic field is given by $\boldsymbol{H}^* = (H_x^*, H_y^*, H_z^*)$. When considering a TE polarisation, variables of interest reduce to E_x^*, E_y^* and H_z^*, while for the TM case H_x^*, H_y^* and E_z^* are required.

Transverse electric and magnetic waves

For problems in two dimensional space, it is possible to simplify the analysis by solving for a specific polarisation. One can simplify the problem by employing decomposition into a transverse electric (TE) and transverse magnetic (TM) polarisation. For example, if it assumed that for a TE polarisation the electric waves are contained in the plane of incidence, this implies that E_z, and therefore H_x and H_y, are zero. Clearly this reduces the number of electric components that need to be found. Reconsidering equation (2.8), to reconstruct the magnetic field for a TE polarisation, yields

$$\mu^* \frac{\partial H_z^*}{\partial t} = -\frac{\partial E_y^*}{\partial x} + \frac{\partial E_x^*}{\partial y} \tag{2.11}$$

$$\epsilon^* \frac{\partial E_y^*}{\partial t} = -\frac{\partial H_z^*}{\partial x} \tag{2.12}$$

$$\epsilon^* \frac{\partial E_x^*}{\partial t} = \frac{\partial H_z^*}{\partial y} \tag{2.13}$$

Hence, once $\boldsymbol{E}$ has been determined we can find $\boldsymbol{H}$ for a TE polarisation. Similarly, for a TM polarisation one assumes the z component of the magnetic field to be zero (the x and y components of the electric field are also zero). As the transverse magnetic wave is such that the magnetic waves are contained in the plane of incidence, this in turn recasts the electric field of equation (2.7) as follows

$$\epsilon^* \frac{\partial E_z^*}{\partial t} = \frac{\partial H_y^*}{\partial x} - \frac{\partial H_x^*}{\partial y} \tag{2.14}$$

$$\mu^* \frac{\partial H_y^*}{\partial t} = \frac{\partial E_z^*}{\partial x} \tag{2.15}$$

$$\mu^* \frac{\partial H_x^*}{\partial t} = -\frac{\partial E_z^*}{\partial y} \tag{2.16}$$

This completes the procedure for constructing a TM polarisation.

2.2 Scattering problems

The simulation of scattering of electromagnetic waves by various objects is of intense interest and the emphasis of this thesis. This interest becomes particulary apparent in the aerospace industry, where information regarding objects such as aeroplanes is desired.

Essentially, scattering problems occur when an electromagnetic wave, generated by a source located in the far field, impinges upon an object. As a result of the interaction between wave and object (technically referred to as a scatterer), the wave is reflected off the scatterer. Knowledge of the precise behavior of the reflected, or scattered wave, then becomes desirable.

Mathematically a scattering problem necessitates a domain that extends to infinity. The infinite domain presents a problem, in computational simulation, as, by definition, it is impossible to represent. A suitable truncation scheme needs to be introduced to mimic the infinite domain, this is discussed at relevant points throughout the thesis. The thesis concerns itself with the numerical solution of outgoing waves only.

2.2.1 The two-dimensional scattering problem

Consider the following problem: An, incident, electromagnetic wave, generated by a source in the far field, interacts with a perfectly conducting obstacle (the scatterer). The scatterer is assumed to be situated in free space. The unknown, desirable, quantities are the electric and magnetic field intensity vectors. The field vectors are expressed relative to a Cartesian coordinate system $O_{x^*y^*z^*}$. The unknown field vectors are of the form $\boldsymbol{E}^* = (E_x^*, E_y^*, E_z^*)$ and $\boldsymbol{H}^* = (H_x^*, H_y^*, H_z^*)$, with E_z^* or H_z^* zero depending a TE or TM polarisation.

The incident wave

The problems of interest, in this thesis, involve the interaction between plane electromagnetic waves generated by a source in the far field. The mathematical nature of the incident wave, adopted in this thesis, is given by

$$\boldsymbol{U}^i = \delta \begin{bmatrix} -\sin\theta \\ \cos\theta \\ 0 \end{bmatrix} e^{-i\omega(x\cos\theta + y\sin\theta)} \tag{2.17}$$

Where $\boldsymbol{U}^i$ is the incident field vector. Here θ is the angle of incidence and it is assumed and that the angle of incidence is zero, hence the incident wave propagates along the x axis. Also, δ is either 1,

for TE simulations or -1 for TM simulations.

2.3 Scattered field formulation

A mathematical system that represents the scattering problem is derived by considering, for two spatial dimensions, the (x^*, y^*) plane as the plane of incidence for the scattered electromagnetic waves.

2.3.1 Non-Dimensional form

Consider the non-dimensional form of Maxwell's equations as detailed in [7]. This form of the equations becomes the starting point from which a numerical solution is to be found in this thesis. To achieve the non-dimensional form, dimensionless variables are introduced.

$$x_j = x_j^*/L^* \qquad t = t^*/L^*\sqrt{\epsilon_0\mu_0} \qquad \epsilon = \epsilon^*/\epsilon_0 \tag{2.18}$$

and

$$E_j = E_j^*/E_a^i \qquad H_j = H_j^*/H_a^i \qquad \mu = \mu^*/\mu_0 \tag{2.19}$$

where L^* denotes a representative length scale associated with the problem, ϵ_0 and μ_0 denote the dielectric permittivity and magnetic permeability of free space and $j = 1, 2$ (as the problem is posed in two-dimensional space). The amplitude of the incident electric wave is denoted by E_a^i.

Decomposition into incident and scattered waves

As scattering problems are under consideration, it is convenient to decompose the field vectors into incident and scattered components, as

$$\boldsymbol{E} = \boldsymbol{E}^s + \boldsymbol{E}^i \qquad \boldsymbol{H} = \boldsymbol{H}^s + \boldsymbol{H}^i \tag{2.20}$$

where the superscripts s and i denote the scattered and known incident fields respectively. The determination of the scattered field components is now the objective.

2.3.2 Conservation form

For the purpose of this thesis, it is desirable to express the Maxwell equations in conservation form. The dimensionless, conservation form maybe written as

$$\frac{\partial \boldsymbol{U}}{\partial t} + \bigtriangledown \cdot \boldsymbol{F}(\boldsymbol{U}) = \mathbf{S} \tag{2.21}$$

where $\boldsymbol{U}$ is the unknown vector and $\boldsymbol{S}$ is a source term. The source term encountered in this thesis is generally zero. The flux term, for two dimensional space, $\boldsymbol{F}(\boldsymbol{U}) = [F_1(\boldsymbol{U}), F_2(\boldsymbol{U})]$, has been introduced in equation (2.21), we therefore have, for the unknown, $\boldsymbol{U}$, and the flux, $\boldsymbol{F}(\boldsymbol{U})$

$$\boldsymbol{U} = \begin{pmatrix} \epsilon \boldsymbol{E}^s \\ \mu \boldsymbol{H}^s \end{pmatrix}, F^i(\boldsymbol{U}) = \begin{pmatrix} -\boldsymbol{e_i} \times \boldsymbol{H} \\ \boldsymbol{e_i} \times \boldsymbol{E} \end{pmatrix} \tag{2.22}$$

where $\boldsymbol{e}_i$ signify the Cartesian unit vectors. The unknown field vectors and flux variables reduce, for TE case, to

$$\boldsymbol{U} = \begin{pmatrix} E_x^s \\ E_y^s \\ H_z^s \end{pmatrix}, \quad \boldsymbol{F}^1(\boldsymbol{U}) = \begin{pmatrix} 0 \\ H_z^s \\ E_y^s \end{pmatrix}, \quad \boldsymbol{F}^2(\boldsymbol{U}) = \begin{pmatrix} -H_z^s \\ 0 \\ -E_x^s \end{pmatrix},$$

and for the TM case we have,

$$\boldsymbol{U} = \begin{pmatrix} H_x^s \\ H_y^s \\ E_z^s \end{pmatrix}, \quad \boldsymbol{F}^1(\boldsymbol{U}) = \begin{pmatrix} 0 \\ -E_z^s \\ -H_y^s \end{pmatrix}, \quad \boldsymbol{F}^2(\boldsymbol{U}) = \begin{pmatrix} E_z^s \\ 0 \\ H_x^s \end{pmatrix},$$

It is advantageous to define a unified formulation

$$\boldsymbol{U} = \begin{pmatrix} U_x \\ U_y \\ U_z \end{pmatrix}, \quad \boldsymbol{F}^1(\boldsymbol{U}) = \delta \begin{pmatrix} 0 \\ U_z \\ U_y \end{pmatrix}, \quad \boldsymbol{F}^2(\boldsymbol{U}) = \delta \begin{pmatrix} -U_z \\ 0 \\ -U_x \end{pmatrix},$$

yielding, for the TE case

$$\delta = 1 \quad U_x = E_x^s \quad U_y = E_y^s \quad U_z^s = H_z \tag{2.23}$$

for the TM case we have

$$\delta = -1 \quad U_x = H_x^s \quad U_y = H_y^s \quad U_z = E_z^s \tag{2.24}$$

This representation of the variables is of direct relevance as it has implications for the designing of a computer code. A code can be written which amalgamates both the TE and TM schemes into one single code, with little effort and computational cost.

2.3.3 Boundary conditions

To achieve an accurate solution to any problem represented by differential equations, boundary conditions need to be considered. Boundary conditions, that are particular to electromagnetism, allow for the accurate modeling of problems such as resistive sheets, material interfaces, impedance boundaries and perfectly conducting walls. Poor specification and implementation of boundary conditions will result in a significant loss of accuracy.

The two boundary conditions, encountered at the extremities of the computational domain, in this thesis are:

Far field

An important consideration in the scattering of electromagnetic waves is the behavior of the scattered wave at the outer limits of the computational domain. At a suitable distance from the scattering object the (scattered) electric and magnetic field components consist of outgoing waves only. It is therefore important to accurately represent this behaviour. A number of possible methods exist for the truncation of an infinite domain. Some of these methods include the coupling of the finite element process with a boundary integral approach which is then capable of approximating the terms at infinity.

The issue of how to properly devise the required far field boundary condition has received much attention in the past. Some of the more complex schemes that are employed involve radiation boundary conditions based on a localisation of the Dirchlet to Neumann (DtN) map [8, 9], or an asymptotic expansion of the far field solution [10]. A simplistic method involves the use of characteristic boundary conditions [11], this method however is only accurate for a close to perpendicular incidence of the wave. Other, alternative, methods involve the use of of buffer or sponge layers. In these methods, the waves are either damped [12], accelerated to supersonic conditions [13], decelerated [14] or a combination of the three [15]. For an informative review of these papers I refer the reader to [16].

Perfect electrical conductor

A perfect electrical conductor (PEC), is employed to simulate regions of infinite conductivity. In the event that the scatterer equates to a perfect electrical conductor, and that an electromagnetic wave impinges upon this body [3], then certain assumptions can be made. These assumptions, that no tangential electric or normal magnetic field can exist, are mathematically represented by the following equations

$$\mathbf{n} \times \mathbf{E} = 0 \qquad \mathbf{n} \cdot \mathbf{H} = 0 \tag{2.25}$$

where $\mathbf{n} = (n_x, n_y)$ is the associated outward surface normal.

[3] the fields are unable to penetrate the body

Chapter 3

The Finite Element Method

3.1 Introduction

To begin, this Chapter presents and briefly discusses the finite element method as a whole. A familiarity of the method is assumed, therefore the basic concepts shall not see much investigation. The chapter continues with topics that are specific to the method employed in this thesis, they are identified and considered in further depth.

The sections that follow involve subjects that in some capacity relate to the numerical scheme employed in this thesis, for example h- and p-type analysis. The chapter evolves by detailing the theory required for the evaluation of an integral.

The time evolution algorithm is discussed in some detail. The discontinuous Galerkin method is then brought to the fore. The properties of the numerical scheme, both advantageous and detrimental, are included in this discussion, culminating with a chronological evolution of the method.

The chapter progresses with the theory required to provide a numerical solution to the Maxwell equations. From this theory all the solutions to Maxwell's equations, in this thesis, are derived. Following the discussion of the aforementioned method, the emphasis tends toward the discontinuous nature of the FEM to be employed. Upon encountering the final topics of the chapter, an understanding on how information is passed between elements is achieved.

3.2 Brief discussion concerning the finite element method

The finite element method is a numerical method that can be employed to provide approximate solutions to partial differential equations. The origins of the finite element method can traditionally be traced to Courant [17] who, in 1947, employed piecewise approximations in order to determine

unknown variables. Subsequently, due to the method's success, numerous mathematical concepts, such as boundary condition representation and assembly, were incorporated into the scheme. These acquisitions, amongst others, clearly enhance the ability of the finite element method, allowing for a higher accuracy in the solution, whilst simultaneously providing a strong mathematical spine.

The finite element method revolves around the basic concept of splitting a would be computational domain into a series of polygons, termed elements. For a two-dimensional problem, these elements are typically triangles or quadrilaterals. If required, a mesh can consist of a hybrid of these two.

This thesis involves itself with the numerical solution of Maxwell's equations upon a discretised domain consisting of triangular elements. The method employed in this thesis involves determining the numerical solution is upon each element of the computational domain. Combining the solutions from each element[1] yields an approximate solution over the entire computational domain.

Three intricacies of the method, that are important to the numerical scheme employed in this thesis, are the selection of a basis function, with which to represent the unknown variable on the element, adequate representation of boundary conditions and the nature of the element which is to tile the computational domain (this later point only relevant for the two-dimensional case).

Electrical problems were first considered, with the idea of solving them via the finite element method, by Arlett and Zienkiewicz [18]. The finite element method was considered for electrical problems due to the fact that the method allows for the treatment of material inhomogeneity without code alteration. The FE method can also allow for the treatment of diverse geometries by using triangles to tile the domain and, traditionally, has a low memory requirement (due to sparse matrices) [19].

Since the advent of the finite element method it is clear that rapid advancements, in the important areas such as accuracy and efficiency, have been made. The method has evolved. These advancements, including high-order and complex domain representation, are apparent in the finite element scheme that is to be employed in this thesis [20]. But, also, as the finite element method grows, and new schemes become realised, so the complexity of the schemes increase. As a result of the increase in complexity, new problems inhibit the analyst. A typical problem being the ability to determine a suitable procedure to employ, out of the multitude that exist, and then efficiently applying it. But first, consider some fundamental concepts of the finite element method.

3.2.1 Spatial discretisation

For practical applications, the requirement of modeling complex geometries means that unstructured mesh methods are particularly attractive. Unstructured meshes involve a tiling of the domain with

[1] termed assembly

triangular elements (in two-dimensional space, tetrahedra in three-dimensional space). Generating complex geometries is a non-trivial task. The difficulties occur, primarily, as a consequence of the shape of the solution domain. The initial concern is the choice of element, specifically which element to employ, and the implications of this choice upon the scheme. The elements that comprise the mesh each have their own attributes.

Triangular elements used to be synonymous with a low-order representation, due to the lack of a suitable, accompanying, high-order basis. Triangular elements are capable of yielding fast results whilst simultaneously representing, due to their nature, a complex domain.

Conversely high-order representation tends to involve rectangular elements, but, by their nature, these elements fail to accurately model complex geometries [4].

This thesis concerns itself with high-order approximation upon an unstructured, triangular, mesh.

3.3 Mappings and the resulting Jacobian

The finite element method places a strong emphasis on the transformation between coordinate systems, the formulation employed in this thesis relies heavily on such mappings. Any mappings that occur are so that a general element, in the computational domain, may be mapped to a local, bounded, element. A simplicity and , in this thesis an increase in efficiency, arises as a result of these mappings.

Any mappings that are employed in this thesis provide a one-to-one relationship between coordinate systems [21].

Isoparametric mappings[2] can be used to transform general elements, from the solution domain, to what is termed a normalised domain. The basis that is subsequently to be employed must then be defined upon this normalised element.

Specifically, for the two-dimensional problem encountered in a subsequent chapter, the transformation theory is employed twice. The two-dimensional problem, considered in this thesis, necessitates the use of a high-order representation applied to an unstructured grid. Therefore, as a consequence of the basis, two transformations must occur. These transformations are now investigated.

The first mapping occurs for the reasons defined above. A second mapping is required so that a coordinate system can be provided in which the basis is well-defined and bounded by constant limits. The second mapping involves a transformation from a local triangular element to another normalised element, this time the unit square.

To devise an efficient high-order scheme, the basis function should endeavor to be formulated from a tensor-product of one-dimensional functions. If a basis is so comprised, the evaluation of the

[2]A mapping where the geometry and the field variable are represented to the same degree

integrals, and any associated mathematics, becomes simplified.

The general Jacobian

As mappings have been introduced, it naturally follows that their consequences should be discussed. A Jacobian arises as a result of a mapping between coordinate systems. The mathematical form of a Jacobian is derived from the relation between the coordinate spaces.

Upon completion of a mapping, any formulae defined in terms of the original cartesian coordinate system, (x, y), needs to be suitably amended and expressed in terms of the new coordinate system (ξ, η) say.

Here an example details how the derivative of a basis function can be expressed with regard to the normalised coordinate system. The chain-rule facilitates the change in coordinate systems.

$$\frac{\partial N_i^e}{\partial \xi} = \frac{\partial N_i^e}{\partial x}\frac{\partial x}{\partial \xi} + \frac{\partial N_i^e}{\partial y}\frac{\partial y}{\partial \xi} \tag{3.1}$$

A derivative with respect to η is similarly given. The matrix form of the transformation is thus given as

$$\begin{pmatrix} \frac{\partial N_i^e}{\partial \xi} \\ \frac{\partial N_i^e}{\partial \eta} \end{pmatrix} = \begin{pmatrix} \frac{\partial x}{\partial \xi} & \frac{\partial y}{\partial \xi} \\ \frac{\partial x}{\partial \eta} & \frac{\partial y}{\partial \xi} \end{pmatrix} \begin{pmatrix} \frac{\partial N_i^e}{\partial x} \\ \frac{\partial N_i^e}{\partial y} \end{pmatrix} = [J] \begin{pmatrix} \frac{\partial N_i^e}{\partial x} \\ \frac{\partial N_i^e}{\partial y} \end{pmatrix} \tag{3.2}$$

The Jacobian matrix, J, is readily determined from the transformation. Inversion of the Jacobian matrix provides the relation

$$\begin{pmatrix} \frac{\partial N_i^e}{\partial x} \\ \frac{\partial N_i^e}{\partial y} \end{pmatrix} = [J^{-1}] \begin{pmatrix} \frac{\partial N_i^e}{\partial \xi} \\ \frac{\partial N_i^e}{\partial \eta} \end{pmatrix} \tag{3.3}$$

A final consideration, arising from the mapping process, is the exact form of the integral in terms of the new coordinate system. A change of coordinate system results in an amendment to the infinitesimal area (line in one-dimensional and volume in three dimensional) element, $dxdy$.

$$dxdy = det[J]d\xi d\eta \tag{3.4}$$

resulting in the integral

$$\int\int_{x_l}^{x_u} \frac{\partial N_i^e}{\partial x} N_j^e dxdy = \int\int_{-1}^{+1} J^{-1}\frac{\partial N_i^e}{\partial \xi} det[J]d\xi d\eta \tag{3.5}$$

Note the constant limits, providing an integral which is more efficient to evaluate.

3.4 Temporal discretisation

Employing time domain schemes, in particular long-time integration for electromagnetic problems, has proven, recently, to be computationally more efficient than other finite element methods (frequency domain) [22, 23]. It has been proposed, in [24], that for the long-time integration of Maxwell's equations, higher-order numerical methods provide the most cost-effective approach [25]. The problems in this thesis are advanced, in time, via the explicit fourth order Runge-Kutta algorithm (other possibilities do exist, such as the Euler forward-step method, or indeed the second-order Runge-Kutta algorithm).

In numerical analysis the Runge-Kutta methods are considered an important family of iterative methods for the approximation of ordinary differential equations. These techniques were developed in the year 1900 (circa) by the mathematicians C. Runge and M. Kutta.

3.4.1 The fourth-order Runge-Kutta temporal algorithm

An investigation of the Runge-Kutta algorithm is to follow. Let an initial value problem be defined as

$$y' = f(t, y), \qquad y(t_0) = y_0 \tag{3.6}$$

Suppose that y_n is the value of the variable at time t_n. The fourth-order Runge-Kutta method then takes y_n and t_n and calculates an approximation for y_{n+1} at a brief time later, $t_n + h$. The formula is defined by

$$y_{n+1} = y_n + \frac{1}{6}(k_1 + 2K_2 + 2K_3 + k_4) \tag{3.7}$$

$$t_{n+1} = t_n + h \tag{3.8}$$

where y_{n+1} is the RK4 approximation of $y(t_{n+1})$ and

- $k_1 = hf(t_n, y_n)$
- $k_2 = hf(t_n + \frac{h}{2}, y_n + \frac{h}{2}k_1)$
- $k_3 = hf(t_n + \frac{h}{2}, y_n + \frac{h}{2}k_2)$

- $k_4 = hf(t_n + h, y_n + hk_3)$

Therefore, the next value (y_{n+1}) is determined by the present value of y_n plus the product of the size of the interval h and an estimated slope. The slope is a weighted average of slopes

- k_1 is the slope at the beginning of the interval
- k_2 is the slope at the midpoint of the interval, using slope k_1 to determine the value of y at the point $t_n + h/2$ using Eulers method
- k_3 is again the slope of the midpoint, but now using k_2 to determine the y-value
- k_4 is the slope at the end of the interval, with its y-value determined using k_3

When the four slopes are averaged, more weight is given to the slopes at the midpoint

$$slope = \frac{k_1 + 2K_2 + 2K_3 + k_4}{6} \tag{3.9}$$

The fourth-order part of the method means that the error per step is on the order of h^5, while the total accumulated error has order h^4.

A problem for consideration, encountered when seeking time-domain solutions, is that errors can accumulate with time. This implies that large scale scattering becomes very complex if not impossible.

3.5 *hp*-type methods

The fundamental concepts of the *hp*-type methods appear in the method that is to be used in this thesis, for the numerical solution of Maxwell's equations. It would therefore be advantageous to state the main concepts of these methods.

The methods referred to as *h*-type methods focus on element size. A polynomial of set degree is chosen to represent the desired unknown over each element, whereupon an improving solution is achieved via a diminishing element. The approximate solution tends to the exact solution, as h, the element length, tends to zero.

Conversely, *p*-adaptivity methods employ a fixed element mesh. Continually increasing the order, p, of the polynomial results in a continual increase in the accuracy of the solution.

In general it has been determined that *p*-adaptivity methods appear less computationally expensive when directly compared to finding a solution upon finer meshes [26]. This statement is investigated in subsequent chapters.

For a detailed analysis of spectral/hp methods I refer the reader to [27, 28] and the references therein.

3.6 Evaluation of integrals

A solution to a variational statement (discussed shortly) involves the evaluation of integrals. Upon expressing an integral in the desired form (any procedures such as mappings, that are required, are performed), how is the integral to be evaluated? The integrals encountered in this thesis are approximated. The approximation is a result of quadrature formulae. The quadrature formulae are substituted in place of the integral. The quadrature formulae, and hence what they approximate, are readily determined via a computer or computers. Clearly the formulae are perfectly suited to computer implementation [29]. The quadrature employed, for the numerical solution of integrals, in this thesis, is due to Gauss.

Gaussian quadrature formulae are considered the foremost accurate procedures available for numerically evaluating an integral [29]. Quadrature formulae rely on the fact that the relevant data is available at specific, pre-determined points. The quadrature points are dictated by the choice of Gaussian quadrature, their number increase (along with the computational cost) with respect to the order of the approximating polynomial. In general, integrals in one- and two-dimensional space can be approximated by a summation of terms. Bearing this in mind it becomes important that the bases selected for the approximation can be expressed in terms of a tensor-product, as the computational cost, when employing Gaussian quadrature, can be kept to a minimum.

$$\int_{-1}^{1} G(\nu)d\nu = W_0 G_0(\eta_0) + \cdots + W_n G_n(\eta_n) = \sum_{m=1}^{nip} G_m(\eta) W_m(\eta) \tag{3.10}$$

where $W_m(\nu)$ and $W_n(\eta)$ are the associated integration weights of the quadrature. The sampling points, $\eta_0, \ldots, \eta_n$, are again determined by the choice of quadrature. This form of the integral is entirely suitable for computer implementation.

3.7 Analytical solutions

Any results that are acquired from a numerical scheme will have to be verified. The verification is performed by comparing the numerical solutions against any existing analytical solutions of the problem. The work conducted by Balanis [30] allows for analytical solutions, relevant to the problems encountered in this thesis, across the given computational domain, to be derived.

3.7.1 The Courant-Friedrichs-Lewy number

The Courant-Friedrichs-Lewy number provides a condition for partial differential equations to be convergent. In many explicit time-marching schemes, the time-step meet certain requirements. If these requirements are not met the approximate solution will produce incorrect results. The CFL condition is given by

$$\frac{\Delta T}{\Delta x} = C \tag{3.11}$$

and the constant C depends upon the equation, or equation set to be solved, not on ΔT or Δx. The CFL number can be a very limiting constraint on the time step (ΔT decreases as the order of approximation increases). The CFL number is something that will be investigated where relevant.

3.8 The discontinuous Galerkin finite element method

The discontinuous Galerkin method may be considered as an amalgam of two schemes, in that the method combines features from both finite volume methods and finite element methods.

The finite volume similarities appear in the form of numerical fluxes. Numerical fluxes are essential to the success of finite volume methods and are incorporated in the discontinuous Galerkin method for similar reasons, to provide a communication between contiguous elements. It is worth noting that the scheme employed in this thesis, is devised in such a way that when piecewise constant approximations are used for the spatial discretisation and the forward Euler method is employed for the temporal discretisation, a standard finite volume scheme is obtained.

The FE similarities arise as the computational domain of interest is discretised into elements, and the numerical solution is then sought upon each element of the discretised computational domain [31]. The discontinuous Galerkin method employs completely discontinuous piecewise polynomials for the numerical solution and the test functions, defined upon each element in turn. Therefore the numerical solution is discontinuous at element interfaces.

3.8.1 Chronology of the Discontinuous Galerkin scheme

The evolution of the discontinuous Galerkin method, in accordance with Cockburn, Karniadakis and Shu [26], is now presented. The discussion is not complete, in that it neglects to include areas of non-direct relevance to this thesis.

The name discontinuous Galerkin first appeared in a paper produced by Delfour and Trochu as early as 1981 [32]. The method however existed previously, only lacking in name. The first study of

the discontinuous Galerkin (DG) method, as it later became known, can be traced to Reed and Hill [33]. The equation under consideration at the time was the independent linear hyperbolic neutron transport equation. It was noted that the linearity of the equation, allied to the smoothness of the solution, permitted an approximate solution to be defined upon each element of the solution domain. The method was then readily applied to ordinary differential equations by LeSaint and Raviart [34]. The analysis of the method, with regards to ordinary differential equations has not relented, many papers provide a detailed analysis of this topic [35, 36].

The first comprehensive analysis of discontinuous finite element methods for two-dimensional linear hyperbolic equations was performed by Lesaint and Raviart [34]. They provided a convergence of $(\Delta x)^{k=1}$, for the scheme on general triangulations. A subsequent proof, for the rate of convergence upon general triangulations, was derived by Johnson and Pitkaränta [37], who proved, numerically, that the rate of convergence, for general triangulations, was $(\Delta x)^{k+1/2}$, where k is the order of the approximating function. This rate of convergence was later shown to be optimal by Peterson [38]. The stability and accuracy properties, of the method, have rigorously been proven in such papers as [39, 40, 41, 42]

The culmination of the research conducted in this area allowed for the discontinuous Galerkin method to be readily applied to such diverse areas as gas-dynamics, oil recovery, meteorology, turbulent flows, weather forecasting and electromagnetism amongst others.

3.8.2 Other discontinuous Galerkin methods

The discontinuous Galerkin method has since been suitably amended to find numerical solutions to other types of problem. For example the local discontinuous Galerkin method proposed by Cockburn and Shu [43], seeks solutions to second, third and even higher order partial differential equations. The LDG method is capable of this by applying the DG method a relevant number of times. The DG method also sees employment in the solution of elliptic problems.

The quadrature-free [29] implementation of the discontinuous Galerkin method appears most promising, and is worth considering for further research, for the following reason. Discontinuous Galerkin methods insist that the integrals are evaluated with quadrature formulas. This insistence increases the memory requirements of the scheme. The quadrature-free DG method avoids the use of quadrature formulas, hence improving the efficiency of the scheme. A quadrature-free formulation involves a set of matrices, the same for each element, that allow the area and boundary integrals to be calculated analytically. The quadrature-free method therefore provides low storage requirements and ameliorates the concern of cost, at no loss of accuracy, whilst maintaining the ability to model complex geometries.

3.8.3 The discontinuous Galerkin method for Maxwell's equations

Important advancements, in terms of solving Maxwell's equations via a DG scheme, were achieved by Warburton and Karniadakis [44]. They provide a discretisation of the Maxwell equations by employing the DG method. Warburton [45] extended this discretisation to involve unstructured hp-finite elements, which is of particular relevance to this thesis. A discontinuous spectral method has been introduced by Kopriva, Woodruff and Hussaini [46]. This theory is also of relevance to the work in this thesis.

3.8.4 Concerning the discontinuous Galerkin method: advantages and disadvantages

The discontinuous Galerkin method can be considered as a robust and compact finite element method that provides an excellent framework for large-scale, time-dependent problems that require high-order accuracy on unstructured grids [47, 24]. The high-order, time-domain and unstructured aspects of the scheme are the most desirable qualities.

An important characteristic of the discontinuous Galerkin method, that distinguishes it from traditional finite element methods, is the lack of continuity between the numerical solution within each element. That the elements in the formulation are considered as completely separate entities, necessitates that the solution within each element be built anew. The numerical solution is acquired from information contained in each element and the boundary data of a neighbouring element(s) only.

The discontinuous nature of the elements, the ability to treat each element as unique, suggests that the basis functions are defined in a completely discontinuous polynomial space. It becomes apparent that as a result of the discontinuous nature of the basis functions, a unique flexibility is acquired. This flexibility allows for a freedom in which to chose the degree of approximation for each element, irrespective of the order of a contiguous element (p-adaptivity). The advantage being the ability to investigate areas of high interest thoroughly. Conversely regions of low interest can be represented by a low order approximation and, thereby, increase the efficiency of the scheme. This suggests that a computational domain could be constructed, in two dimensional space, of a hybrid mesh of both triangles and quadrilaterals. The flexibility also allows the discontinuous Galerkin method to employ arbitrary sized triangulations (h-adaptivity), allowing for mesh refinement in particular areas of interest [48, 49].

The local data structure of the discontinuous Galerkin scheme results in a formulation with a high parallel efficiency. The discontinuous Galerkin method also exhibits an insensitivity to the smoothness of the mesh [50]. As there exists a complete decoupling of elements, the inclusion of a heteroge-

neous collection of materials is dealt with in a natural way, their specification, in the relevant element, is all that is required.

The DG method does exhibit some disadvantages however. These problems become clear upon implementation. The discontinuous Galekin scheme must store the coefficients associated with the judiciously chosen basis. As high-order representation is often required or desired, the coefficients become numerous and the high storage and computational requirements become apparent [51].

3.9 The Runge-Kutta discontinuous Galerkin method

Problems of interest, in computational electromagnetics, share similarities in that they are generally computationally very large with respect to the computational wavelength, and include complex geometries. The accurate modeling of such complex problems involves an analysis over a long duration, thus implying that high-order methods be considered to generate a solution to Maxwell's equations in the time-domain. Chavent and Salzano [52], to avoid implicit time discertisations (computationally inefficient due to the need of evaluating at each time-step), devised the first explicit version of the DG method. This method however failed upon analysis [3]. Another explicit scheme needed to be derived.

The Runge-Kutta discontinuous Galerkin (RKDG) method was first introduced by Cockburn and Shu [53]. Cockburn and Shu showed that the RKDG method is perfectly suited in providing high-order accurate solutions to scalar hyperbolic conservation laws [54]. The recognition that high-order schemes significantly enhance the quality of the solution demanded that they be considered [55, 56]. The culmination of extensive work performed upon RKDG schemes resulted in a paper, [57], that provided RKDG techniques for the numerical solution of conservation laws.

Standard spectral methods provide high-order numerical solutions. Although these methods are highly accurate for smooth functions, their failing quality is a dependence upon a simplistic solution domain; they suffer on complex geometries [55, 58]. To address this deficiency, spectral methods evolved to incorporate spectral element methods [59]. Spectral elements consist of tiling the computational domain with quadrilaterals in two dimensions (hexahedral in three dimensions). The undesirable consequence of such a discretisation is that the solution domain consists of a structured mesh, and is therefore, only a moderate improvement. Natural evolution of the scheme led to the idea of non-conforming elements [60]. Non-conforming elements can be employed to extend the spectral discretisation to more complex geometries, although this increases the computational cost and lessens the adaptive capability. It can therefore be understood that the derivation of a new high-order finite element method suitable for unstructured grids, at a computationally low cost, was essential.

[3] the method was unstable for $\frac{\Delta t}{\Delta x} = c, a constant$

Much of the work in the area of high-order approximations on unstructured grids, for time dependent problems, have involved modal expansions [22, 25, 55, 44].

Traditionally the prevailing methods, when the geometry is complex, are low order finite element or finite volume methods (high-order finite volume methods [61, 62] for unstructured grids do exist but they are rather complex and expensive [31]) . These methods were employed for the reasons detailed in Chapter One. It is well known that triangular elements are much more adept at representing complex solution domains. As expected, the extension of a low-order approximation to that of a higher order is non-trivial. Attempting to derive a high-order basis from a low-order basis generally results in ill-conditioning. The ill-conditioning arises due to linear dependence of the basis. Alternatively, collapsing the corners of spectral elements (quadrilaterals) onto a triangular domain is not a possibility for hyperbolic equations, as time-step restrictions are introduced that are unacceptable [63]; something new was needed. Intuition suggests that an amalgamation of the two theories would provide an excellent solution. The idea is to extend the spectral element method to incorporate triangular elements. The incorporation of triangular elements, into spectral methods, would result in an increase in the complexity of the domain representation, whilst maintaining a high order of representation. This theory would be of interest for further research.

3.10 The traditional Galerkin method

In order that the numerical scheme to be employed is fully understood, the Galerkin finite element method is now analysed. It will become apparent that the discontinuous Galerkin method applies the traditional Galerkin method to each element of the discretised computational domain in turn.

3.10.1 The variational formulation

The variational statement [64], that accompanies the DG formulation, is derived by applying the Galerkin procedure to each individual element of the computational domain. Consider a system of equations in dimensionless, conservation form, ably represented by equation (2.21). The solution to equations (2.7) and (2.8) is of interest as, for the reasons given in Chapter Two, equations (2.9) and (2.10) are assumed to be satisfied.

The computational domain, Ω, is partitioned into a collection of non-overlapping elements T_i. The elements must tile the entire solution domain, hence $\bigcup_{i=1}^{Ne} T_i = \Omega$ where Ne represents the total number of elements. The variational statement is achieved upon multiplication of equation (2.21) by a test function and by introducing a weighting function (for Galerkin methods the test and

weighting functions inhabit the same space, Φ_a, to be discussed shortly). Therefore, multiplying by a test function W and then integrating over each element, e, [22], we obtain, for two-dimensional space

$$\int_{\Omega_e} \frac{\partial \boldsymbol{U}^e}{\partial t} W d\Omega + \sum_{i=1}^{2} \int_{\Omega_e} \frac{\partial \boldsymbol{F}_i^e}{\partial x_i} W d\Omega = \mathbf{0} \tag{3.12}$$

Where $\boldsymbol{U}^e$ is the unknown vector and $\boldsymbol{F}^e$ is the previously defined flux term over each element e . To be in accordance with Galerkin, the test function exists in the same finite element space, Φ_a, as the approximate solution. The space, Φ_a, is a finite-dimensional subspace of the space of discontinuous functions. The exact solution, $\boldsymbol{U}^e$, in each element is approximated by $\boldsymbol{U}_a^e \epsilon \Phi_a$. Applying Gauss' divergence theorem (integration by parts in one-dimensional space) to equation (3.12) yields the weak variational [64] formulation.

$$\int_{\Omega_e} \frac{\partial \boldsymbol{U}_a^e}{\partial t} W d\Omega + \int_{\partial\Omega_e} \boldsymbol{F}_n^e W d\Gamma - \sum_{i=1}^{2} \int_{\Omega_e} \frac{\partial W}{\partial x_i} \boldsymbol{F}_i^e(\boldsymbol{U}_a^e) d\Omega = \mathbf{0} \tag{3.13}$$

where

$$\boldsymbol{F}_n = \sum_{i=1}^{nDim} n_i \boldsymbol{F}_i(\boldsymbol{U}_a^e) \tag{3.14}$$

here n_i represents the outward normal. The connection between neighbouring elements depends upon how the boundary conditions are enforced. The chapters that follow provide procedures that adroitly present a means of solution to this variational statement, equation (3.13).

3.10.2 The approximate solution

In the discontinuous Galerkin formulation, a numerical solution $\boldsymbol{U}_a^e$ is sought within each element. The approximate solution is given as a linear combination of a basis function weighted by unknown degrees of freedom.

$$\boldsymbol{U} \approx \sum_{e=1}^{Ne} \boldsymbol{U}_a^e = \sum_{e=1}^{Ne} \sum_{j=0}^{P} a_j N_j(x_1) \tag{3.15}$$

where a_j denote the unknown degrees of freedom and $N_j(x_1), j = 0, 1, \ldots, P$ denote the set of basis polynomials such that P is the highest order of the polynomial. The coefficients, a_j, now become the desired, and sought, unknowns.

3.10.3 Discontinuous space

The space, Φ_a, in which the problem is to be posed is now considered. By definition, a continuous function space is not the natural place to pose the problems encountered in this thesis. The natural alternative is a formulation where Φ_a contains discontinuous elements[4]. Then each element that tiles the computational domain has polynomials defined within that element. These polynomials are zero outside of that element. We define

$$\Phi_a = \{W \in L_2(\Omega) : W|\, T_i \in \mathcal{P}(T_i)\, \forall\, T_i\} \tag{3.16}$$

where $\mathcal{P}(\Omega)$ is the polynomial space defined on the domain Ω [22].

3.11 Upwind schemes

When evaluating for the boundary integral upon internal edges, the flux terms are not uniquely defined. The loss of uniqueness is a result of employing a discontinuous approximation polynomial (defined over each element only). The flux function is therefore evaluated in terms of a consistent numerical flux. The numerical flux depends upon both interface states and, as a result, introduces a necessary coupling between elements. As the Maxwell equations are a system of equations, an approximate or exact Riemann solver must be employed (as opposed to a monotone flux for single set of equations) [65].

The family of upwind schemes, whose origins can be traced to Courant, Reeves and Isaacson, are directed towards the introduction of physical properties of flow into the discretised formulation. Upwind schemes are dependent upon the hyperbolicity of the equation [66]. If an equation set, Maxwell's equations for example, exhibit a hyperbolic nature then certain properties can be incorporated into the numerical scheme. Information is propagated along characteristics. The characteristics are determined by the eigenvalues of the associated Jacobian matrix. The signs of these eigenvalues dictate the direction of propagation. For the Maxwell equation set, due to their linearity, the eigenvalues are constant and, as a consequence of their hyperbolicity, the e-values are real, so determining the numerical flux is not so demanding.

Upwind schemes allow for the calculation of discontinuous solutions, so lend themselves perfectly to the discontinuous Galerkin method. The schemes differ with respect to the amount of physical information incorporated into the discretisation process.

[4]Continuous function spaces are neglected due to the possibility of large banded matrices that result as a consequence of overlapping support

Upwind schemes provide the platform from which more accurate schemes can be derived. The two foremost being the flux difference splitting and flux vector splitting [66]. Flux difference splitting involves the splitting of $\boldsymbol{U}$, as is done in this thesis, and flux vector splitting involves $\boldsymbol{F}$ being split.

For a hyperbolic system of equations an approximate Riemann solver would be employed [22].[5] The numerical flux chosen for this thesis is due to Roe [67].

The general mathematical form of the Roe flux is discussed shortly, and we see its specific imposition, for one and two dimensional cases, in Chapters Four (page 39) and Five (page 71).

The numerical flux is clearly of great importance. Basically, the numerical flux takes into account the direction of propagation of the wave at the element interface, and allows for a passing of information between elements [51].

3.11.1 Other numerical fluxes

Numerous possibilities exist for the choice of the numerical flux alternatives to the Roe flux employed in this thesis, are now considered, Two that come to mind are the Godunov flux and the Lax-Friedrichs flux. There exists basically two approaches to extending the theory one being flux difference splitting, of which some examples are the schemes are, Godunov [68], Osher [69], Harten, Lax, and van Leer [70] and Roe [67] (the numerical flux choosen for this thesis). The other approach is flux vector splitting, some examples of which are due to Stegerand Warming [71] and van Leer [72]. However, as the degree of the approximation increases the choice of numerical flux has diminishing effect on the quality of the approximation [73].

3.11.2 Characteristic flux decomposition

Physical properties of flow can be incorporated into the numerical scheme via a characteristic decomposition. The method is detailed here for a general case, and will be employed when considering the one- and two-dimensional problems in the subsequent chapters that follow. Following the outline detailed by Sherwin [74], consider the set of equations

$$\frac{\partial \boldsymbol{U}}{\partial t} + \frac{\partial \boldsymbol{F}_i(\boldsymbol{U})}{\partial x_i} = 0 \qquad i = 1, ndim \tag{3.17}$$

In non-conservative form the equation becomes

$$\frac{\partial \boldsymbol{U}}{\partial t} + \boldsymbol{A}_n \frac{\partial \boldsymbol{U}}{\partial x_i} = 0 \qquad i = 1, ndim \tag{3.18}$$

[5] As opposed to an exact solver, the names are self explanatory

where $\boldsymbol{A}_n$ is a Jacobian matrix whose entries are constant. $\boldsymbol{A}_n$ is given by,

$$\boldsymbol{A}_n = \sum_{i=1}^{dim} n_i \frac{\partial \boldsymbol{F}_i}{\partial \boldsymbol{U}} \tag{3.19}$$

The Jacobian matrix $\boldsymbol{A}_n$ can be decoupled into a diagonal matrix $\boldsymbol{D}$ of eigenvalues, in the form

$$\boldsymbol{L}\boldsymbol{A}_n\boldsymbol{R} = \boldsymbol{D} \tag{3.20}$$

and

$$\boldsymbol{R}\boldsymbol{D}\boldsymbol{L} = \boldsymbol{A}_n \tag{3.21}$$

Here the columns $\boldsymbol{L}$ and $\boldsymbol{R}$ are the left and right eigenvectors of $\boldsymbol{A}_n$ respectively. The eigenvalues are derived from the characteristic equation

$$|\lambda I - \boldsymbol{A}_n| = 0 \tag{3.22}$$

where the size of I, the identity matrix, depends upon the dimension of space in which the Maxwell equations are to be solved. Substituting (3.21) into (3.18) implies that

$$\frac{\partial \boldsymbol{U}}{\partial t} + \boldsymbol{R}\boldsymbol{D}\boldsymbol{L}\frac{\partial \boldsymbol{U}}{\partial x} = 0 \tag{3.23}$$

When $\boldsymbol{A}_n$ is symmetric, as is the case for the Maxwell equations, $\boldsymbol{L} = \boldsymbol{R}$, and so we can write

$$\boldsymbol{R}\boldsymbol{A}_n\boldsymbol{R}^{-1} = \boldsymbol{D} \tag{3.24}$$

Let the solution's of equation to (3.22) be

$$\lambda_1 = u \qquad \lambda_2 = -u \tag{3.25}$$

the corresponding eigenvectors $\boldsymbol{x}_1$ and $\boldsymbol{x}_2$ satisfy

$$\boldsymbol{A}\boldsymbol{x}_1 = \lambda_1\boldsymbol{x}_1 \qquad \boldsymbol{A}\boldsymbol{x}_2 = \lambda_2\boldsymbol{x}_2 \tag{3.26}$$

Assume

$$\boldsymbol{x}_1 = \begin{bmatrix} x_1^1 \\ x_1^2. \end{bmatrix} \qquad \boldsymbol{x}_2 = \begin{bmatrix} x_2^1 \\ x_2^2 \end{bmatrix} \tag{3.27}$$

Then the matrix $\boldsymbol{R}$ can be defined by

$$\boldsymbol{R} = [\boldsymbol{x}_1 \quad \boldsymbol{x}_2] = \begin{bmatrix} x_1^1 & x_2^1 \\ x_1^2 & x_2^2 \end{bmatrix} \tag{3.28}$$

with the inverse

$$\boldsymbol{R}^{-1} = \frac{1}{x_1^1 x_2^2 - x_1^2 x_2^1} \begin{bmatrix} x_2^2 & -x_2^1 \\ -x_1^2 & x_1^1 \end{bmatrix} \tag{3.29}$$

It can now be shown

$$\boldsymbol{R}\boldsymbol{A}_n\boldsymbol{R}^{-1} = \begin{bmatrix} \lambda_1 & 0 \\ 0 & \lambda_2 \end{bmatrix} = \boldsymbol{D} \tag{3.30}$$

where $\boldsymbol{D}$ gives the diagonal matrix and $\boldsymbol{R}^{-1}\boldsymbol{R} = \boldsymbol{I}$. Let $\boldsymbol{U} = \boldsymbol{R}\boldsymbol{V}$ and pre-multiply the equation by $\boldsymbol{R}^{-1}$ the resulting equation yields

$$\frac{\partial \boldsymbol{V}}{\partial t} + \boldsymbol{R}^{-1}\boldsymbol{A}_n\boldsymbol{R}\frac{\partial \boldsymbol{V}}{\partial x} = 0 \tag{3.31}$$

where $\boldsymbol{V} = [V_1, V_2]$ are the Riemann invariants. It follows that

$$\frac{\partial V_1}{\partial t} + \frac{\partial V_1}{\partial x} = 0 \tag{3.32}$$

and

$$\frac{\partial V_2}{\partial t} - \frac{\partial V_2}{\partial x} = 0 \tag{3.33}$$

hence

$$\frac{\partial x}{\partial t} = 1, -1 \tag{3.34}$$

This implies that V_1 and V_2 are constant. Again, from $\boldsymbol{U} = \boldsymbol{R}\boldsymbol{V}$ we get, for the electromagnetic

case

$$V_1 = \frac{1}{2}[\boldsymbol{E} + \boldsymbol{H}] \qquad V_2 = \frac{1}{2}[\boldsymbol{E} - \boldsymbol{H}] \tag{3.35}$$

These are the Riemann invariants.

3.11.3 Mathematical representation of the Roe flux

The Roe flux [67] is represented mathematically by

$$\tilde{\boldsymbol{F}}^{roe}\left(\boldsymbol{U}^L, \boldsymbol{U}^R\right) = \frac{1}{2}[\left(\boldsymbol{F}_n{}^R + \boldsymbol{F}_n{}^L\right) - |\boldsymbol{A}|\left(\boldsymbol{U}^R - \boldsymbol{U}^L\right)] \tag{3.36}$$

and is used at all internal boundaries in this thesis. Here $\boldsymbol{U}^L$ and $\boldsymbol{U}^R$ represent the values on the left- and right-hand-side of the interface and $\boldsymbol{F}_n$ is defined in equation (3.14). The matrix $\boldsymbol{A}$ is defined by

$$\boldsymbol{A} = \boldsymbol{P}^{-1}\Gamma\boldsymbol{P} \tag{3.37}$$

and

$$|\boldsymbol{A}| = \boldsymbol{P}^{-1}\,|\Gamma|\,\boldsymbol{P} \tag{3.38}$$

where $\boldsymbol{P}$ is a matrix whose columns are the eigenvectors of $\boldsymbol{A}$, and Γ is a matrix whose diagonal entries are the eigenvalues of $\boldsymbol{A}$. The modulus of the matrix $\boldsymbol{A}$ is taken to ensure that the correct direction of propagation is assured (upstream).

3.12 The Rankine-Hugoniot condition

When a discontinuity exists between elements, the relation between the flow variables on either side of the discontinuity is provided by the Rankine-Hugoniot equation. Consider the following, one-dimensional equation (similar to equation (3.17))

$$\frac{\partial U}{\partial t} + \frac{F(U)}{\partial x} = 0 \tag{3.39}$$

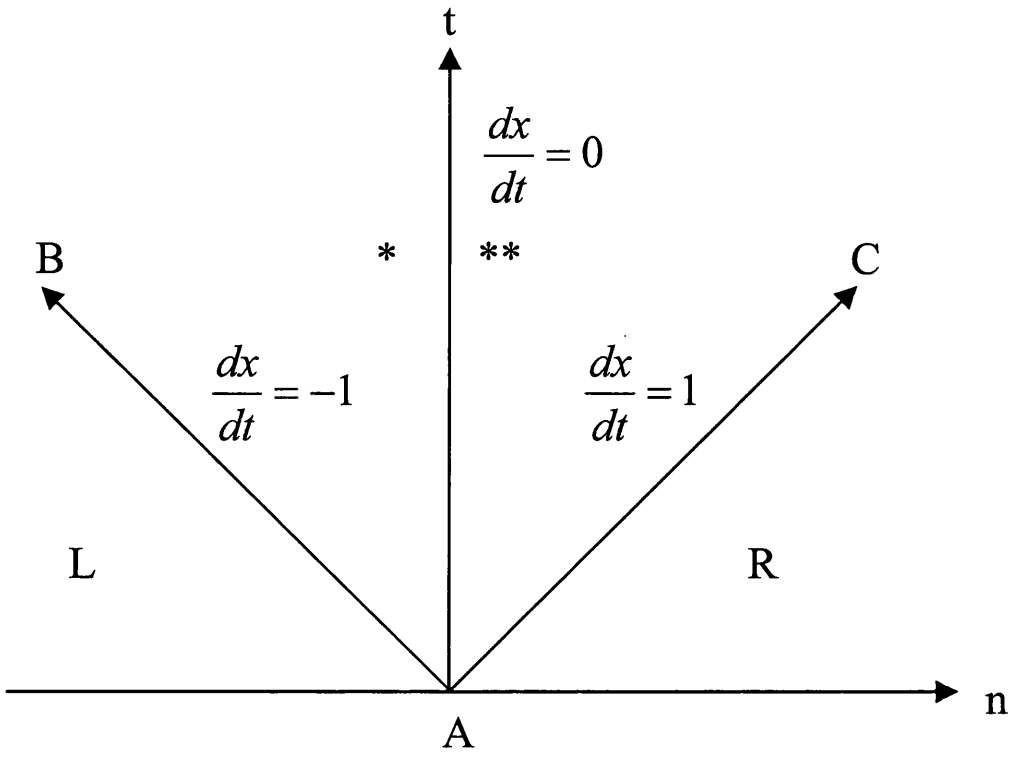

Figure 3.1: The dimensionless characteristics

here $x(t)$ is the shock and must satisfy the Rankine-Hugoniot condition.

$$\lambda_i = \dot{x} = \frac{[F(U)]}{[U]} \tag{3.40}$$

where λ is the eigenvalue, $\dot{x}$ is the shock speed, whose direction is determined by the sign associated with it. Also, $[u] = u(x_+) - u(x_-)$ and $[F(u)] = F(u(x_+)) - F(u(x_-))$.

Another advantage of employing the dimensionless form of Maxwell's equations is that the following eigenvalues are achieved.

$$\lambda_1, = -1 \qquad \lambda_2 = 0, \qquad \lambda_3 = 1 \tag{3.41}$$

The derivation of which shall be discussed when considering the solution of Maxwell's equations in two dimensions. Employing the relevant Rankine-Hugoniot jump equations across each characteristic direction, yields the equations for each boundary flux function, be it a PEC boundary or a far field boundary or an internal boundary.

The simplest manner of enforcing the non-reflective boundary condition (at the far field) is obtained by splitting the flux into characteristic components and grouping the components according to whether their associated wave is entering or leaving the plane. The Rankine-Hugoniot condition provides the theory which allows for imposition of this far field boundary condition. The Rankine-Hugoniot condition can also be employed for the PEC boundary condition and inter-element formulation.

Chapter 4

The One-Dimensional Problem

4.1 Introduction

This chapter presents the theory required to express Maxwell's one-dimensional equations in a form such that an approximate solution, via the Runge-Kutta discontinuous Galerkin method, can be determined. Methods by which numerical approximations to given problems will also be addressed.

The variational statement, introduced in the previous chapter, is recalled, with the precise one-dimensional form subsequently investigated. The major interest in the one-dimensional variational statement is directed toward the boundary integral. Implementation of the boundary conditions is also considered.

The accuracy and efficiency of any scheme is highly dependent upon specifying an apt basis. The basis employed here is chosen as a consequence of its properties. The basis is capable of providing high-order accuracy and is efficient at doing so. To maximise the benefits of the selected basis, a mapping is required. The transformation, from the global x-coordinate system to a local ξ-coordinate system, and the resultant Jacobian, are discussed.

The integrals that comprise the final form of the one-dimensional variational statement are considered individually. Numerical evaluation of each integral is achieved via Gaussian quadrature. The chapter continues with a discussion of the implementation of the Runge-Kutta discontinuous Galerkin scheme.

A verification of the convergence of the scheme is performed and convergence of the L^2 and semi-norm are considered.

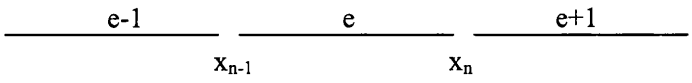

Figure 4.1: A one-dimensional discontinuous discretisation

4.2 A one dimensional example

Normalising (the vacuum speed of light is unity i.e. $\varepsilon_0 = \mu_0 = 1$ and the lengths are scaled with respect to a selected length scale) the one-dimensional Maxwell equations yields a respective electric and magnetic field of

$$\boldsymbol{E} = (E, 0, 0) \qquad \boldsymbol{H} = (0, H, 0) \tag{4.1}$$

The fields are sought in the domains $\Omega \times T$. Here Ω represents the entire spatial solution domain, $0 \leq x_1 \leq L$ and T the temporal domain such that $0 \leq t \leq T$. An approximate solution, $\boldsymbol{U}_a$, to this problem is desired.

The one-dimensional example considered here introduces the basis framework so that the two-dimensional example, considered in the next chapter can be fully understood.

As the intention[1] of this example is to introduce the particulars of the scheme, the need to consider two materials, free space and a dielectric region, is not required. However, the interested reader will note that the incorporation of a dielectric is trivial and depends upon element identification (as each element is considered independently).

4.2.1 Domain discretisation

The spatial discretisation, for one-dimensional space, consists of a union of non-overlapping line elements as exhibited in figure (4.1). A typical element, e, shall be partitioned by (x_{n-1}, x_n), where n is the element index. The length, h_e, of this element is given by $h_e = x_n - x_{n-1}$.

4.2.2 The variational statement

The previous Chapter exemplified the procedure necessary to derive the multi-dimensional variational statement, however, it remains to investigate the areas specific to one-dimensional space.

[1] clearly note the sole intention, also *hp* analysis

The main interest lies with the appearance of the boundary integral. The boundary integral is introduced via integration by parts. For the one-dimensional problem equation (3.13) implies[2]

$$\int_{\Omega_e} \frac{\partial \boldsymbol{U}_a}{\partial t} N_i \, \mathrm{d}x = \int_{\Omega_e} \boldsymbol{F}(\boldsymbol{U}_a) \frac{\partial N_i}{\partial x} \, \mathrm{d}x + \int_{\Gamma_e} n_x \boldsymbol{F}(\boldsymbol{U}_A) N_i \, d\Gamma \tag{4.2}$$

The simplified, one-dimensional, representation is

$$\int_{\Omega_e} \frac{\partial \boldsymbol{U}_a}{\partial t} N_i \, \mathrm{d}x = \int_{\Omega_e} \boldsymbol{F}(\boldsymbol{U}_a) \frac{\partial N_i}{\partial x} \, \mathrm{d}x - [\tilde{\boldsymbol{F}}(\boldsymbol{U}_a) N_i]_{x_n} + [\tilde{\boldsymbol{F}}(\boldsymbol{U}_a) N_i]_{x_{n-1}} \tag{4.3}$$

where $\tilde{\boldsymbol{F}}$ is the numerical flux, which has replaced the flux term. At an interface between two elements[3], the flux vector is dependant upon the values of $\boldsymbol{U}_a$ (approximate solution in each element) in both elements (the approximate solution, $\boldsymbol{U}_a$, is assumed to be discontinuous at the end points of each element). The two values of $\boldsymbol{U}_a$, at the element interface, are given by $\boldsymbol{U}_a^{e-1}$ and $\boldsymbol{U}_a^{e+1}$, which correspond to the left and right elements, at a given, internal, element interface, respectively. With this knowledge therefore, the boundary flux maybe correctly expressed as $\boldsymbol{F}(\boldsymbol{U}_a^{e-1}, \boldsymbol{U}_a^{e+1})$. This formulation completes the spatial discretisation whilst simultaneously providing for a communication between elements.

4.3 The one-dimensional basis

Various possibilities from which to select a basis exist. However, the quality and efficiency, of a method is strongly dependant upon the choice of basis. The basis employed for this one-dimensional example must satisfy some pre-requisites, in that it must be both efficient and high-order accurate.

Legendre polynomials, are selected as the basis function, which adhere to these demands. Legendre polynomials are capable of high-order approximation and provide excellent efficiency because of their L^2-orthogonality property over the range $[-1, 1]$. To improve the benefits of employing Legendre polynomials as a basis, they ought to be standardised. Standardising the basis entails introducing a local domain; let ξ, such that $\xi \in [-1, 1]$ be the new local coordinate of this local domain. All operations are then performed with respect to this domain [21].

[2]It is taken that we will consider each element individually, hence the superscript notation e will be omitted unless required for clarity.

[3]the ends of the element, i.e. x_{n-1} and x_n, in this one-dimensional case

4.3.1 The local element

To facilitate numerical operations, each element, e, in the computational domain is mapped to a local element $\tilde{e} \in [-1, 1]$. A simplicity arises as a result of transferring all the operations to the normalised local element, in that they become easier to perform i.e. integration between constant limits. The mapping between the two coordinate systems is defined by the transformation

$$\xi = \frac{2(x - x_c^e)}{h^e} \qquad x_c^e = \frac{x_{e-1} + x_e}{2} \tag{4.4}$$

where x_c is the coordinate value at the centre of the element in the original coordinate system. The relevance of this expression becomes apparent when considering how element shape functions are to be formulated in terms of the local coordinate ξ. The right hand side derivative in equation (4.3) is recast as

$$\frac{dN}{dx} = \frac{dN}{d\xi}\frac{d\xi}{dx} = \frac{dN}{d\xi}\frac{2}{h_e} \tag{4.5}$$

where the derivative, $d\xi/dx$, is obtained from equation (4.4).

4.3.2 Legendre polynomials

The Legendre polynomials are generated through the expression [75]

$$L_j(\xi) = \frac{1}{2^{(j-1)}} \sum_{i=0}^{j} \begin{pmatrix} j \\ i \end{pmatrix} \begin{pmatrix} j \\ j-i \end{pmatrix} (\xi - 1)^{j-i}(\xi + 1)^i \tag{4.6}$$

This formula allows for the j^th order polynomial to be generated. Inspection of equation (4.3) reveals the derivative of the Legendre polynomial, with respect to ξ, is also required. The derivative is evaluated by the relation

$$b_{1,j}\frac{dL_j(\xi)}{d\xi} = b_{2,j}L_j(\xi) + b_{3,j}L_{j-1}(\xi) \tag{4.7}$$

where

$$b_{1,j} = 2j(1 - \xi^2) \qquad b_{2,j} = -2j^2\xi \qquad b_{3,j} = 2j^2 \tag{4.8}$$

4.3.3 The revised approximate solution

In light of the above, the revised approximate solution, in each element is then defined as

$$\boldsymbol{U}_a^e = \sum_{j=0}^{P} a_j N_j(x_1) \tag{4.9}$$

where

$$N_j(x_1) = L_m(\frac{2(x - x_c^e)}{h^e}) \tag{4.10}$$

4.4 The 1-D line integral

Each integral in the variational statement must be recast in terms of the local coordinate ξ. The line-integral from equation (4.3), this now becomes

$$\int_e \boldsymbol{F}(\boldsymbol{U}_a)\frac{\partial N}{\partial x}\, dx = \int_{-1}^{1} \boldsymbol{F}(\boldsymbol{U}_a)\frac{\partial N}{\partial \xi}\frac{2}{h^e}|J|\, d\xi \tag{4.11}$$

Substituting equation (4.5) into the above integral it follows that

$$\int_e \boldsymbol{F}(\boldsymbol{U}_a)\frac{\partial N}{\partial x}\, dx = \int_{-1}^{1} \boldsymbol{F}(\boldsymbol{U}_a)\frac{\partial N}{\partial \xi}\, d\xi \tag{4.12}$$

4.5 The mass matrix

The matrix on the left hand side of equation (4.3) is referred to as the mass matrix. The orthogonality property of the Legendre polynomial has positive consequences with regard to the efficiency of the scheme. The benefits of the orthogonality become clear when considering the mass matrix. Employing the Legendre polynomials, as the basis, results in an integral of the form

$$\int_1^{-1} L_m(v)L_n(v)dv = \frac{2}{2m+1}\delta_{mn} \tag{4.13}$$

where $\delta_{mn} = 1$ if m is equal to n and zero otherwise. This means that the mass matrix is diagonal and therefore easily invertible.

4.6 The one-dimensional Roe flux

An important consideration is the treatment and enforcement of the boundary terms. One type of boundary condition that must be enforced is the inter-element condition. This type of boundary condition is enforced via the numerical flux. The one-dimensional form of formula (3.36), due to Roe, is employed. The derivation of the Roe flux starts with an examination of the Jacobian matrix $\boldsymbol{A}$. The one-dimensional Jacobian matrix follows, from equation (3.19), as

$$\boldsymbol{A} = \frac{\partial \boldsymbol{F}}{\partial \boldsymbol{U}} \tag{4.14}$$

For this problem the entries of the Jacobian matrix$\mathbf{A}$ can readily be determined as

$$\boldsymbol{A} = \begin{pmatrix} 0 & 1 \\ 1 & 0 \end{pmatrix} \tag{4.15}$$

The eigenvalues of $\boldsymbol{A}$ are given by $\lambda = \pm 1$.[4] Following the procedure detailed in Chapter Three,

$$\mathbf{R} = \begin{pmatrix} 1 & 1 \\ 1 & -1 \end{pmatrix}, \qquad \mathbf{R}^{-1} = -\frac{1}{2}\begin{pmatrix} -1 & 1 \\ 1 & 1 \end{pmatrix}$$

The diagonal matrix $|\Gamma|$ is given by

$$|\Gamma| = \begin{pmatrix} 1 & 0 \\ 0 & 1 \end{pmatrix}$$

We are now in a position to define $|\boldsymbol{A}|$, an integral part of the Roe flux, which is defined as

$$|\boldsymbol{A}| = \boldsymbol{R}^{-1}|\Gamma|\boldsymbol{R} = \begin{pmatrix} 1 & 0 \\ 0 & -1 \end{pmatrix}$$

Substituting $|\boldsymbol{A}|$ into formula (3.13) results in the final form of the Roe flux. The unknown terms are now given by the electric and magnetic fields only,

$$\mathbf{F}(\mathbf{U}_L, \mathbf{U}_R) = \frac{1}{2}\left(\begin{pmatrix} H_L \\ E_L \end{pmatrix} + \begin{pmatrix} H_R \\ E_R \end{pmatrix} - \begin{pmatrix} 1 & 0 \\ 0 & -1 \end{pmatrix}\begin{pmatrix} E_R - E_L \\ H_R - H_L \end{pmatrix}\right) \tag{4.16}$$

[4] From the characteristic equation

Reducing the expression above gives the numerical flux to be:

$$\mathbf{F}(\mathbf{U}_L, \mathbf{U}_R) = \frac{1}{2}(\begin{pmatrix} H_L + H_R \\ E_L + E_R \end{pmatrix} + \begin{pmatrix} E_L - E_R \\ H_R - H_L \end{pmatrix}) \tag{4.17}$$

This form of the numerical flux is incorporated directly into the numerical scheme.

The final form is a system of time evolution equations, and is, here, advanced in time via the fourth-order Runge-Kutta algorithm.

4.7 L^2 Norm

The convergence, $||\boldsymbol{e}||_L$, rates of the scheme can be measured in the L^2 to give information about the convergence behaviour of the scheme. The L^2 norm is given by

$$||\boldsymbol{e}||_L = \frac{\sqrt{\int_{-1}^{1}(\boldsymbol{E} - \boldsymbol{e})^2}}{\sqrt{\int_{-1}^{1}\boldsymbol{E}^2}} \tag{4.18}$$

where $\boldsymbol{E}$ is the exact, known, solution and $\boldsymbol{e}$ is the numerical solution.

4.8 Specification of the Problem

The problem under consideration is a one-dimensional problem where a plane single frequency incident wave is propagated and impinges upon a perfectly conducting obstacle, information regarding the scattered field is then desired.

The integrals

The mass matrix and the line-integral are evaluated via Gaussian quadrature as is the boundary integral. The mass matrix can be determined before the scheme is advanced in time. After acquiring the mass matrix, its inversion is trivial, mere division. It then follows to evaluate the line-integral. Finally, upon identification, the boundary conditions are then evaluated. The scheme is then forwarded in time. But the interest in the one-dimensional case lies with the boundary conditions. Understanding how the conditions are enforced is essential to understanding the scheme. The first boundary acts as the PEC, which clearly relies upon the incident ray.

The excitation is given as

$$E = H = \cos(\frac{2\pi t}{\lambda}) \tag{4.19}$$

this is directly incorporated into the scheme.

4.9 Results

The results achieved from the theory are now presented. The results serve more as a validation process, as this example has been investigated on previous occasions. For the results expressed in tabular form it can be taken that, unless otherwise stated, the wavelength, λ, is equal to two and that the scheme is run for 2000 steps with a time increment of $\Delta t = 0.01$ (resulting in a CFL that is well within the required limits). When the problem is performed under these conditions, and for this duration, a steady state is achieved.

The tables that follow provide the results obtained for various forms of analysis. The first six tables provide information concerning the minimum number of elements required, per wavelength, for an acceptable solution.

The tables also provide the corresponding error analysis which yields the reasoning as to the quantity of elements to employ. Noting the norms, it can be seen, for example, that a cubic approximation requires 4 elements per wavelength as 3 elements per wavelength results in an increase in the L^2-norm. These results are depicted visually in figure (4.10) through to figure (4.20) (note that the constant order approximation is not considered as it can be seen, from the relevant table, that a large number of elements per wavelength are required.

It is interesting to note that an examination of figures (4.17) and (4.19) reveals that, due to the computational cost involved, further analysis of an order five approximation is not required, as near identical results are obtained.

4.9.1 Exact solution

For the examples considered here, the verification often involves a comparison with an exact solution. The exact solution employed for this particular case is contained within the one-dimensional code and is in the form of a planar wave given by

$$E = H = \cos(\frac{2\pi t}{\lambda}) \tag{4.20}$$

4.9.2 Tables of results

For a constant order approximation the required number of elements per wavelength is given by

Elements per lambda	Element size	Total elements	L^2-Norm	$H-1$-Norm
160	0.0125	1600	0.3966	0.0321
120	0.0167	1200	0.4001	0.0339
60	0.0333	600	0.5314	0.0453

For a linear order polynomial the number of elements required is deduced from

Elements per lambda	Element size	Total elements	L^2-Norm	$H-1$-Norm	Time taken (seconds)
25	0.08	250	0.0309	0.0119	9.03
20	0.01	200	0.0360	0.0137	7.27
10	0.2	100	0.0993	0.0284	4.22
9	0.22222	90	0.1238	0.0382	2.01

Similarly for a quadratic polynomial

Elements per lambda	Element size	Total elements	L^2-Norm	$H-1$-Norm	Time taken (seconds)
6	0.33333	60	0.0405	0.0127	5.09
5	0.4	50	0.04120	0.0129	4.12
4	0.5	40	0.0582	0.0175	3.08

A cubic polynomial representation yields

Elements per lambda	Element size	Total elements	L^2-Norm	$H-1$-Norm	Time taken (seconds)
4	0.5	40	0.0312	0.0128	8.28
3	0.6667	30	0.0372	0.0190	6.92
2	0.1	20	0.0691	0.0335	4.12

For an order 4 polynomial

Elements per lambda	Element size	Total elements	L^2-Norm	$H-1$-Norm	Time taken (seconds)
3	0.6667	30	0.0316	0.0298	14.00
2	1.0	20	0.0353	0.0306	9.38
1	2.0	10	0.2560	0.0323	4.75

For an order 5 polynomial

Elements per lambda	Element size	Total elements	L^2-Norm	$H-1$-Norm	Time taken (seconds)
2	1.0	20	0.0309	0.0331	18.89
1	2.0	10	0.0661	0.0348	9.52

4.10 The lowest L^2 norms

The lowest achievable value for the L^2-norm is now presented. The results achieved are for a converged solution and the table presents the variation of the L^2 norm of the error. The table also provides the minimum number of steps required for a converged solution with the associated value of delta t. Initially the length of each element is $h = 0.1$, then in the next table couple, elements of length $h = 0.2$ are considered. For both examples the mesh consists of 100 line elements with $\lambda = 2.0$. All calculations are to six decimal places.

Order	Nstep	delta t	L^2-Norm
0	99	0.101010	0.589418
1	453	0.022075	0.04271
2	1190	0.008403	0.02615
3	2550	0.003922	0.020242
4	7980	0.001253	0.016934

For example if we require an order four approximation, the minimum number of steps that the code has to be run is 7980, using a time increment of 0.001253.

Therefore the corresponding CFL numbers, given by the Von Neumann analysis, are given by

Order	CFL number
0	1.01010
1	0.220751
2	0.084034
3	0.039216
4	0.012531

For the the following example the length of each element, is given by $h = 0.2$, in total there exists 50 elements. The length of the wave is given by $\lambda = 2.0$. Again all calculations are to six decimal places

Order	Nstep	delta t	L^2-Norm
0	40	0.25	0.6505312
1	200	0.05	0.079194
2	1115	0.008969	0.035018
3	2490	0.004016	0.0272218
4	3000	0.033333	0.0229184

The corresponding CFL numbers are given by

Order	CFL number
0	0.5
1	0.250
2	0.04843
3	0.02008
4	0.01667

4.11 The CFL number

The results to follow are those achieved via a mesh comprised with elements of length $h = 0.1$ and $h = 0.2$ respectively. The results do not provide the lowest L^2-norm but provide acceptable solutions. Viewing the results reveals that a factor of two permutates through the two tables, as the element length differs by a multiple of two it can be assumed that the number of steps (Nstep) and the time increment (delta t) approximately equate, resulting in very similar CFL numbers.

Order	Nstep	delta t	CFL	L^2-Norm	H-1 Norm
0	136	0.0735	1.4705	0.141799	0.2028
1	392	0.0255	0.5102	0.00884	0.0480
2	780	0.0128	0.2564	0.00402	0.0251
3	1258	0.0080	0.1590	0.00088	0.0239
4	1839	0.0054	0.1088	0.00023	0.0193
5	2501	0.004	0.080	0.00005	0.0191

The results obtained for $h = 0.1$

Order	Nstep	delta t	CFL	L^2-Norm	H-1 Norm
0	70	0.1429	1.4290	0.3750	0.2830
1	204	0.0490	0.4902	0.0045	0.2723
2	393	0.0254	0.2544	0.0025	0.0148
3	642	0.0156	0.1557	0.0011	0.0116
4	938	0.0107	0.1066	0.0008	0.0080
5	1329	0.0075	0.075	0.0008	0.0078

The results obtained for $h = 0.2$

Order	Nstep	delta t	CFL	L^2	H-1 Norm
0	35	0.28570	1.4286	0.6699	0.2028
1	96	0.1042	0.5208	0.2665	0.2001
2	201	0.0498	0.2488	0.0078	0.0190
3	320	0.0313	0.1563	0.0033	0.0132
4	470	0.0213	0.1064	0.0003	0.0062
5	639	0.0156	0.0782	0.0003	0.0063

The corresponding CFL numbers that yield solutions

Order	CFL	np/wavelength	Nstep
0	1.43	60	60/1.43=42
1	0.52	20	39
2	0.26	6	24
3	0.16	3	19
4	0.11	2	19
5	0.08	1	13

By analysing these tables, we are now in a position to select, if so desired, an order of approximation, a number of elements and a time-step that will provide the desired error that we are satisfied with. We will also be able to tell you how long this computation will take.

4.12 The real time taken to perform an analysis

The final table provides an insight into the operation time of the scheme. The table below proves that an order five approximation requires approximately double the real time when in comparison with an order four approximation.

Order	delta T	Nstep	Element length	No of el's	Time taken (seconds)
0	0.01	2000	0.5	500	5.0
1	0.01	2000	0.5	500	15.33
2	0.01	2000	0.5	500	47.49
3	0.01	2000	0.5	500	120.42
4	0.01	2000	0.5	500	270.66
5	0.01	2000	0.5	500	529.75

The above table, in conjunction with the previous results, therefore suggests that an order five approximation is avoidable as only marginal improvement in accuracy is achieved, but this at a large cost to the efficiency of the scheme.

Of the following, graphical, results only few are of direct relevance to the above tables. Figure (4.2) depicts the numerical convergence of the electric field on a mesh consisting of 128 elements. This figure, figure (4.2), shows that the desired exact solution, for this problem, can be achieved with an order two approximation.

4.12.1 Verifying the numerical solutions

4.12.2 Refinement

As discussed in the previous Chapter, it is of interest to investigate the benefit of h-type analysis over p-type analysis. This comparison is easily done in one-dimensional space as the line elements can be easily varied. To determine the most suitable refinement strategy, h or p, the computational accuracy of particular examples is to be compared. The comparison will centre around the number of unknowns required to obtain the desired numerical solution.

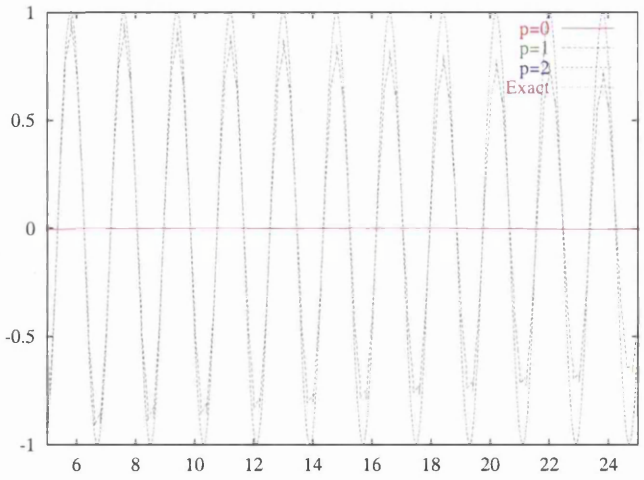

Figure 4.2: p-refinement on initial 128 element mesh: comparison of the convergence of the electric field with the exact solution

For the h-refinement strategies the initial mesh under consideration consists of 128 line elements, each of length of $h = 0.2$. The second and third meshes are obtained by refining this initial mesh by a factor of four and then sixteen. The polynomial that is employed uniformly over each mesh, is of order $p = 0$.

When investigating the p-refinement strategies, the spacing in the initial mesh is maintained, with numerical solutions achieved by employing polynomials of order $p = 0, 1, 2$ and $p = 3$.

The analysis reveals that it is more beneficial to increase the polynomial order (as opposed to refining the mesh). This conclusion is drawn by analysing figure (4.2) with figures (4.7) through to (4.9). These figures reveal that increasing the order of the approximation from $p = 0$ to $p = 2$ leads to convergence to the exact solution. The h-refinement figures show that the effect of splitting the mesh by a factor of 4 and then 16 fails to result in a converged solution, clearly a finer spacing is required for convergence using h-refinement.

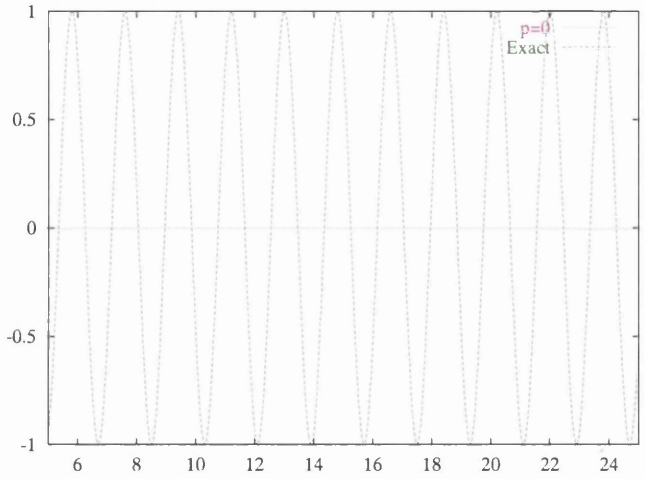

Figure 4.3: Numerical solution: solution details the comparison between p=0 polynomial and the exact solution on a mesh of 128 elements

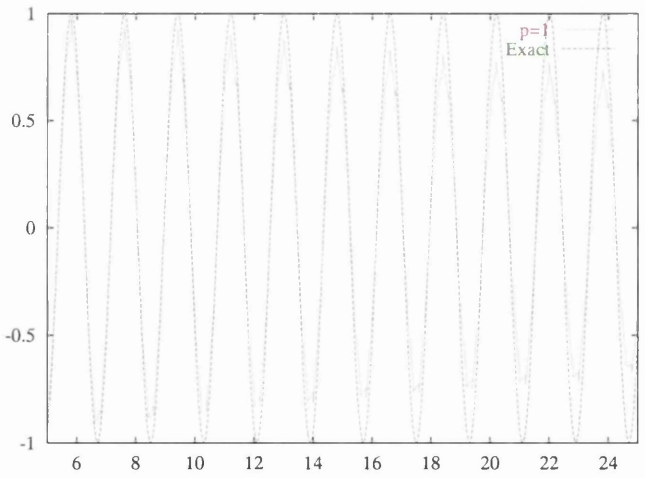

Figure 4.4: Numerical solution: solution details the comparison between p=1 polynomial and the exact solution on a mesh of 128 elements

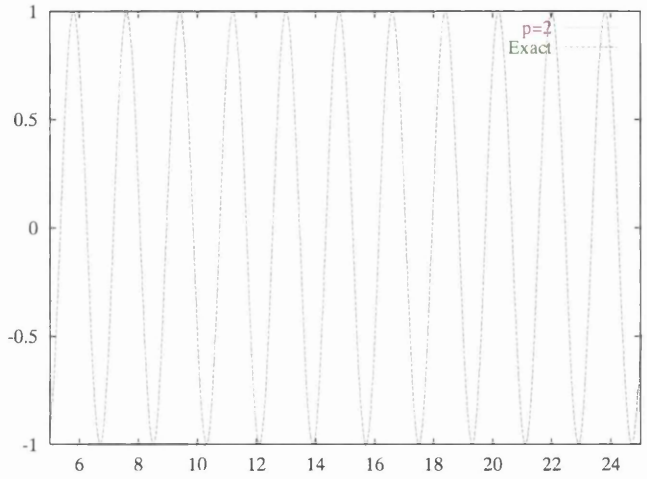

Figure 4.5: Numerical solution: solution details the comparison between p=2 polynomial and the exact solution on a mesh of 128 elements

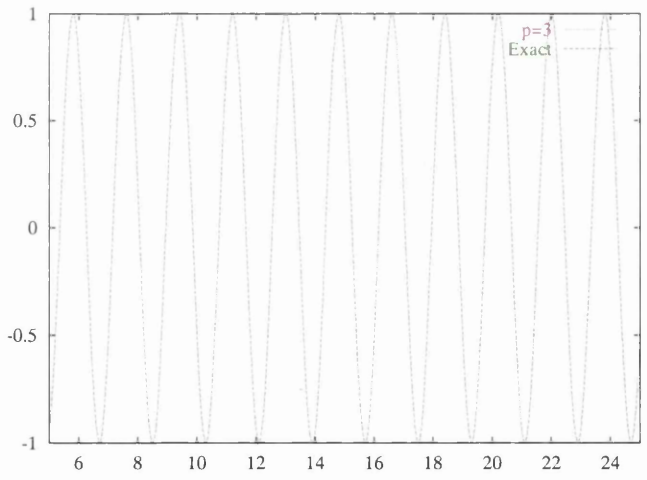

Figure 4.6: Numerical solution: solution details the comparison between p=3 polynomial and the exact solution on a mesh of 128 elements

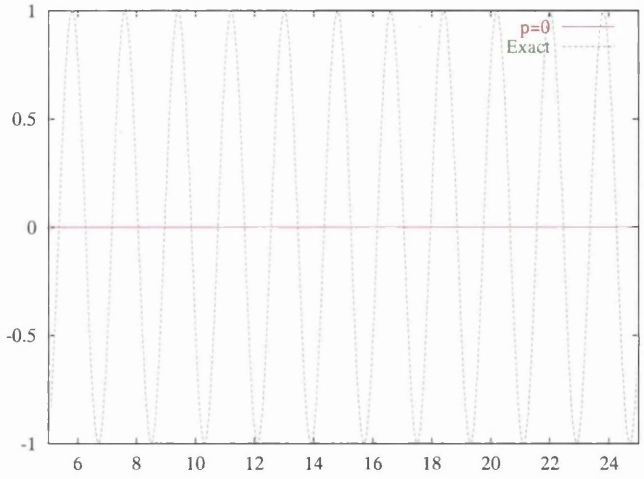

Figure 4.7: h-refinement: solution details the comparison between a p=0 polynomial and the exact solution upon a mesh of 128 elements

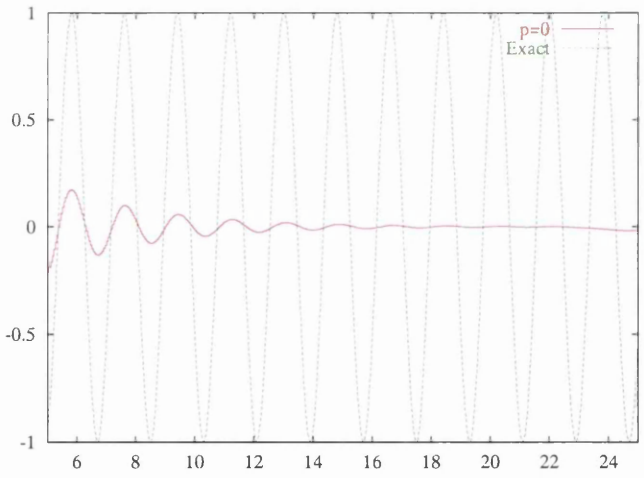

Figure 4.8: h-refinement mesh consists of 512 elements: solution details the comparison between a p=0 polynomial and the exact solution for the first h-refinement

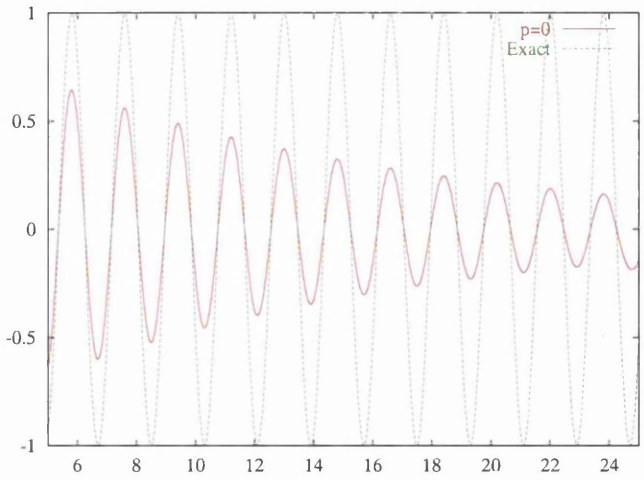

Figure 4.9: h-refinement mesh consists of 2048 elements: solution details the comparison between a p=0 polynomial and the exact solution upon the second h-refinement

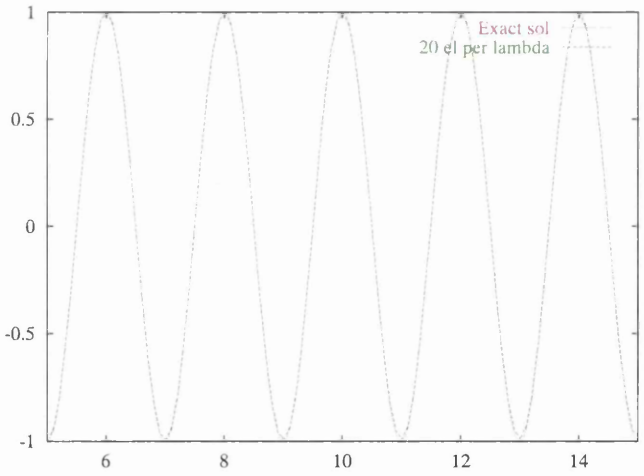

Figure 4.10: Comparison between exact solution and order 1 polynomial with 20 elements per wavelength

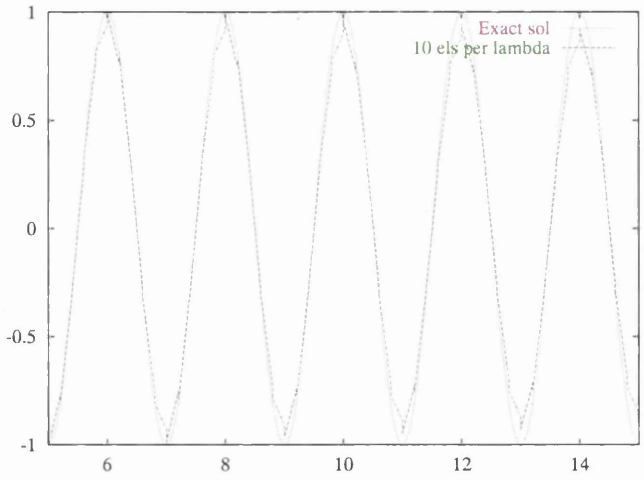

Figure 4.11: Comparison between exact solution and order 1 polynomial with 10 elements per wavelength

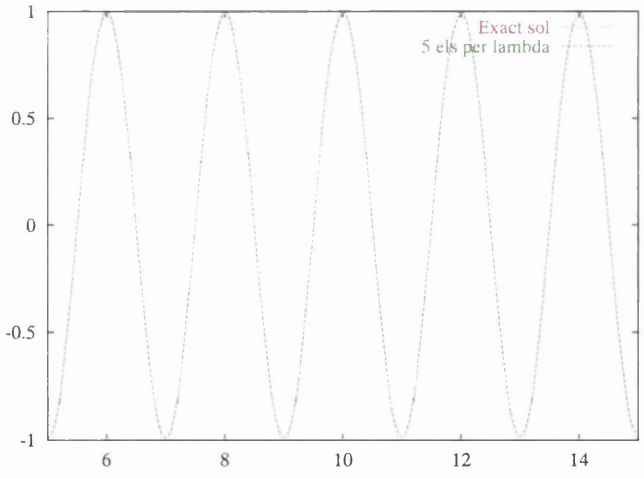

Figure 4.12: Comparison between exact solution and order 2 polynomial with 5 elements per wavelength

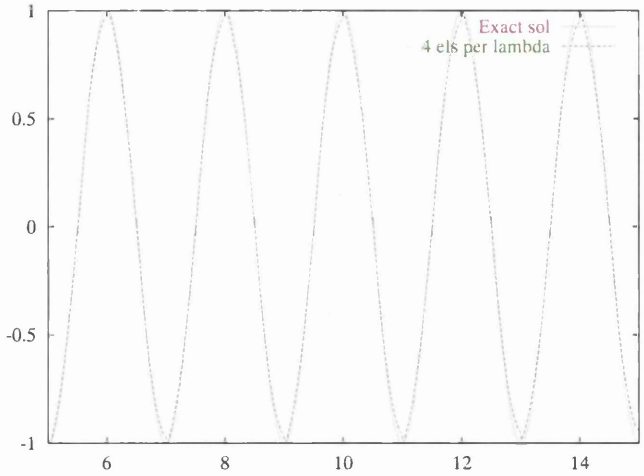

Figure 4.13: Comparison between exact solution and order 2 polynomial with 4 elements per wavelength

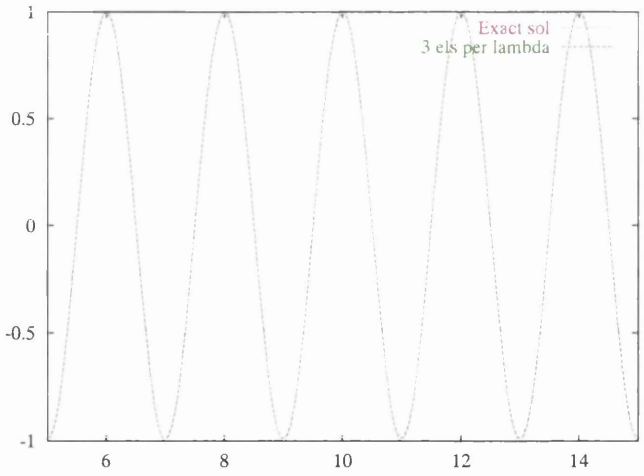

Figure 4.14: Comparison between exact solution and order 3 polynomial with 3 elements per wavelength

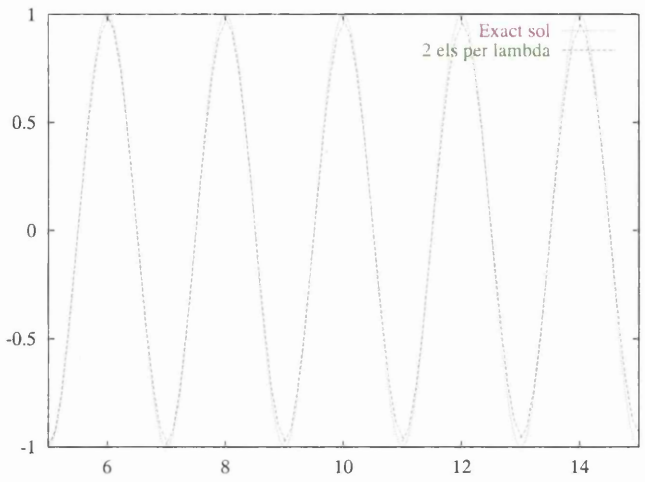

Figure 4.15: Comparison between exact solution and order 3 polynomial with 2 elements per wavelength

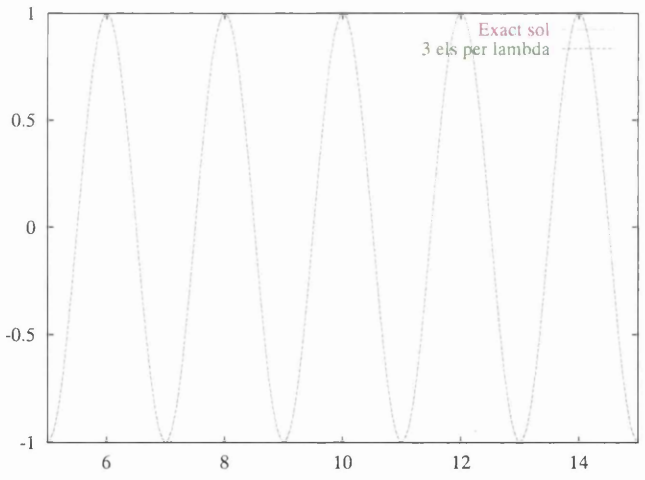

Figure 4.16: Comparison between exact solution and order 4 polynomial with 3 elements per wavelength

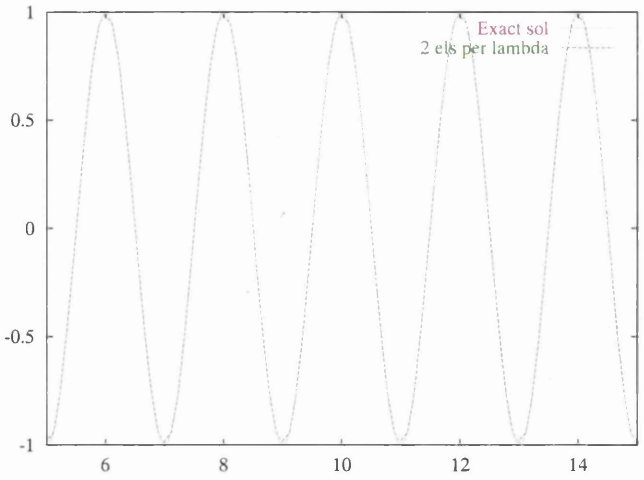

Figure 4.17: Comparison between exact solution and order 4 polynomial with 2 elements per wavelength

4.13 A Taylor-Galerkin comparison

The major differences with the Taylor-Galerkin finite element method and the RKDG method is that the temporal discretisation is based upon a truncated Taylor expansion, instead of the fourth-order Runge-Kutta algorithm. And the other other major difference is that for the spatial discretisation the approximate solution can be constructed by using elements that share and edge (in two dimensions, a face in three dimensions and a point in one-dimension). Therefore C^0 continuous bases can be employed.

The one-dimensional analysis concludes with a comparison between the RKDG scheme and the continuous, linear, Taylor-Galerkin scheme (TG). The Figures (4.21-4.24) provide the results achieved via the TG scheme. The results show that a minimum of 10 elements per wavelength is required for an acceptable solution, the TG scheme, employed here does not provide the option for p type higher-order representation, so should the case arrive when only 4 elements per wavelength are required then the TG scheme would not be of much assistance. The figure (4.13) shows that numerical solutions for this electrical length can be provided, if desired (here an order two approximation was required), via a Runge-Kutta discontinuous Galerkin scheme.

The Taylor-Galerkin scheme employed in the examples was provided by K. Morgan.

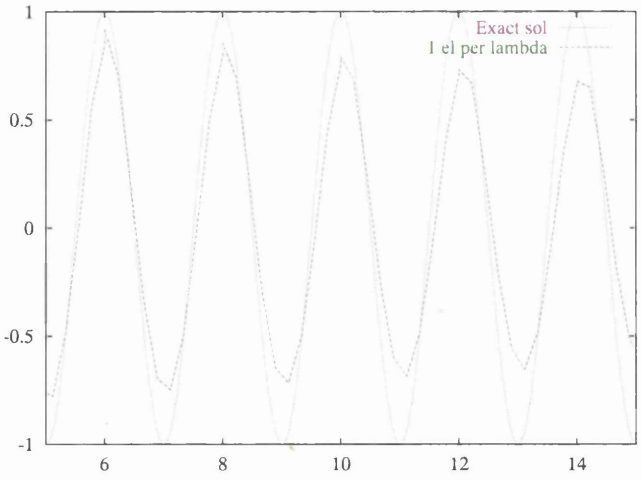

Figure 4.18: Comparison between exact solution and order 4 polynomial with 1 element per wavelength

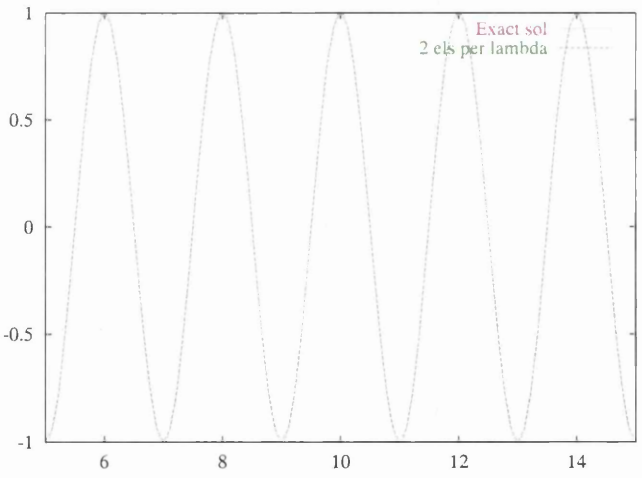

Figure 4.19: Comparison between exact solution and order 5 polynomial with 2 elements per wavelength

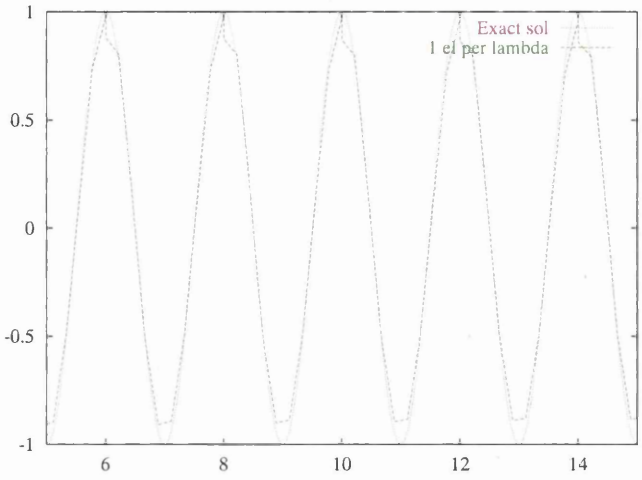

Figure 4.20: Comparison between exact solution and order 5 polynomial with 1 element per wavelength

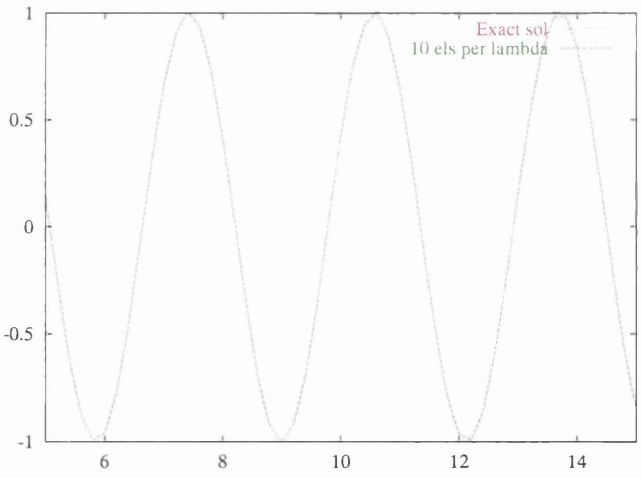

Figure 4.21: Comparison between exact solution and Taylor-Galerkin scheme with 10 elements per wavelength

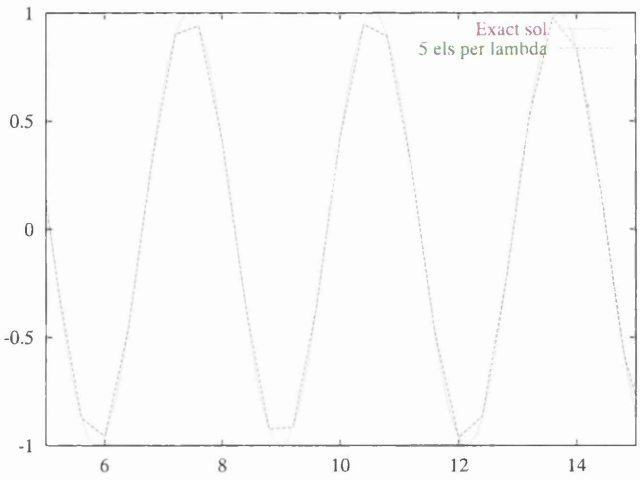

Figure 4.22: Comparison between exact solution and Taylor-Galerkin scheme with 5 elements per wavelength

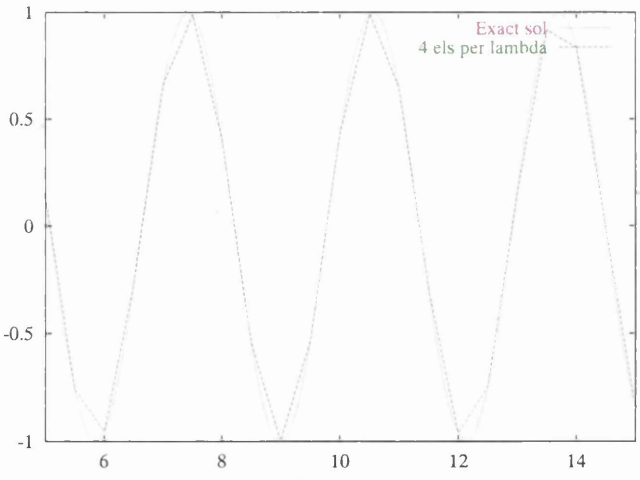

Figure 4.23: Comparison between exact solution and Taylor-Galerkin scheme with 4 elements per wavelength

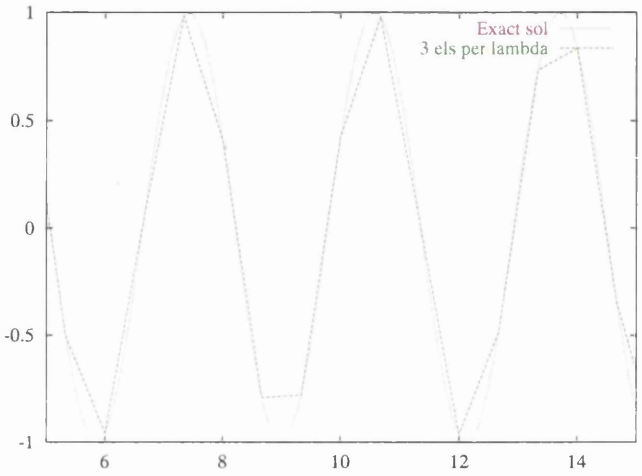

Figure 4.24: Comparison between exact solution and Taylor-Galerkin scheme with 3 elements per wavelength

Chapter 5

The Two-Dimensional Scattering Problem

5.1 Introduction

This chapter advances the theory required to provide a numerical solution to Maxwell's equations by building on the topics presented in previous chapters.

The chapter begins by describing the simulation. Then the variational statement that accompanies the problem is provided. A decision on which basis to employ is then made. The discussion, concerning the basis, will include any requirements placed upon the basis as a consequence of the finite element scheme. We continue by detailing the coordinate systems that are encountered in order to accommodate the basis. The various topics that the mappings raise are then considered.

Results are then produced and the scheme is verified.

5.2 Statement of problem

Scattering problems are considered in this chapter. Chapter Two saw the theory of transverse electric (TE) and transverse magnetic (TM) theory being investigated. Here the scattering problem, applicable to either of the polarisations, is presented. The problem under investigation is as defined in Chapter Two, with the unknowns being the respective two-dimensional electric and magnetic field vectors $\boldsymbol{E} = (E_x, E_y, E_z)$ and $\boldsymbol{H} = (H_x, H_y, H_z)$. The field vectors are reduced in accordance with the problem to be solved. The unknown fields are assumed to be decomposed into incident and scattered components, as specified by equation (2.20).

5.3 The two-dimensional problem

The variational statement, as it appears in equation (3.13), correctly represents the two-dimensional scattering problem: find $\boldsymbol{U}$ such that

$$\frac{d}{dt}\int_e \boldsymbol{U}_a^e W d\Omega = \int_e \sum_{j=1}^{2} \frac{\partial W}{\partial x_j}\boldsymbol{F}^j d\Omega - \int_{\Gamma_e} \boldsymbol{F}^n W d\Gamma \tag{5.1}$$

here the notation is consistent with Chapter Two, where Γ_e denotes the boundary of the element e. The introduction of the boundary term is a consequence of Gauss' rule (to be discussed next). In the boundary integral

$$\boldsymbol{F}^n = \sum_{j=1}^{2} n_j \boldsymbol{F}_j \tag{5.2}$$

where $\boldsymbol{n} = (n_x, n_y)$ is the unit outward normal vector.

5.4 The basis

To form a valid numerical scheme a basis must be specified. The basis is required to be high-order accurate and applicable to triangular elements. A basis that adheres to these requirements proved elusive until Karniadakis and Sherwin [74], followed by Warburton [45], described a basis suitable for constructing both L^2 and C^0 expansions. These expansions are based upon the original ideas of Dubiner [63].

The Dubiner bases

The original basis proposed by Dubiner [63] is capable of high-order representation and can be defined upon triangular elements. This basis is attractive as it has the additional benefit of L^2-orthogonality. However, Dubiner's basis is not directly applicable to a continuous triangular mesh[4], as attempting to apply the basis to triangular elements destroys the orthogonality property. To counter this problem, Dubiner needed to devise an alternate basis that was applicable to a continuous triangular mesh, whilst still maintaining a high-order representation. The new basis is an extension of the old basis and, as a consequence, retains partial orthogonality. The new basis is referred to as the modified Dubiner basis.

To summarise: the original basis is high-order accurate, and applicable to non-connected elements. Similarly, Dubiner's modified basis exhibits high-order accuracy and can be applied to a

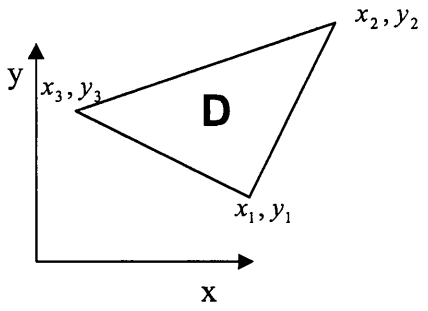

1. Original coordinate system

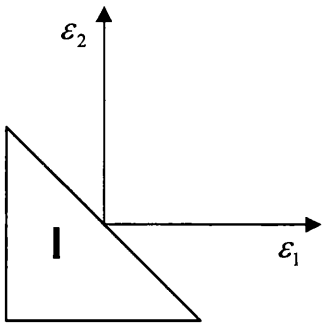

2. Coordinate system resulting from the first transformation

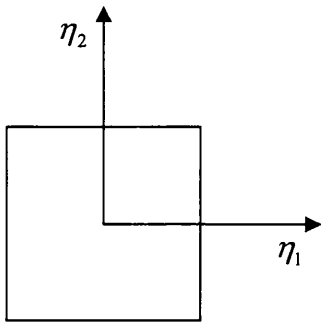

3. Coordinate system to facilitate the basis

Figure 5.1: The three coordinate systems encountered

continuous mesh, but at the cost of a decrease in orthogonality. However, the intrinsic nature of the discontinuous Galerkin method resolves the problem presented by the original Dubiner basis. Consider the fact that any basis that is to be employed, in a DG scheme, need not define a continuous basis (continuity of functions is not required for internal edges as discontinuous elements are employed). The conservativity property is automatically held [22] (L^2 expansions are required). Therefore the original Dubiner basis is perfectly suited to the scheme and is therefore the chosen basis.

5.5 Two coordinate systems

The basis proposed by Dubiner is a tensorial type of basis. The basis is a product of one- and two-dimensional tensors, this Dubiner referred to as a warped or general product [63] [1]. As the basis is so comprised, a suitable coordinate system, with independent limits, is a necessity. The need to employ such a coordinate system (although trivial in itself) introduces the majority of the mathematical complexity. To facilitate the numerical operations that are to be performed, such as differentiation and integration, two mappings are required [55].

Defining a suitable set of local coordinates, on which the Dubiner basis is well posed, involves each triangular element in the discretised computational domain being mapped to a reference triangle. Following this initial mapping, the second and final coordinate system arises from the mapping of the triangular element to a rectangular element, for clarity consider figure (5.1)

5.5.1 The first mapping

The first transformation is a mapping from a general triangle, $\boldsymbol{D} \subset R^2$, in the solution domain, to a local triangle, $\boldsymbol{I} \subset R^2$, in the cartesian (ξ_1, ξ_2) coordinate system (depicted in figure (5.1)).

During the mapping elements which comprise the computational domain are assumed initially to be straight sided. It is further assumed that a mapping, Ψ, from the $\boldsymbol{D}$ simplex to the $\boldsymbol{I}$ simplex has been established and is one to one and onto such that $\Psi : \boldsymbol{D} \rightarrow \boldsymbol{I}$.

Concepts of the first mapping

Figure (5.1) shows the triangle $\boldsymbol{D}$ with vertices V_1, V_2 and V_3, and with corresponding coordinates (x_1, y_1), (x_2, y_2) and (x_3, y_3). The counterclockwise numbering of the edges and vertices ensures a strictly positive Jacobian. The correspondence between the two coordinate systems is provided by the barycentric coordinates $(\lambda_1, \lambda_2, \lambda_3)$, where

$$\lambda_1(\boldsymbol{\xi}) = -\frac{\xi_1 + \xi_2}{2}, \quad \lambda_2(\boldsymbol{\xi}) = \frac{1 + \xi_1}{2}, \quad \lambda_3(\boldsymbol{\xi}) = \frac{1 + \xi_2}{2} \tag{5.3}$$

and

$$\lambda_1 + \lambda_2 + \lambda_3 = 1, \quad 0 \leq (\lambda_1, \lambda_2, \lambda_3) \leq 1 \tag{5.4}$$

[1] The distinction is made so as not to confuse the warped/ general tensor product (employed upon triangles) with the standard tensor product (upon quadrilaterals).

Any point in the triangle D can be expressed as a function of the barycentric coordinates and the vertices, by

$$\begin{bmatrix} x \\ y \end{bmatrix} = \sum_{i=1}^{3} \begin{bmatrix} x_i \\ y_i \end{bmatrix} \lambda_i \tag{5.5}$$

Equation (5.5) provides the required mapping between the coordinate systems. It is now possible to define the elements in terms of the new coordinate system. In a cartesian system, a triangular element would be defined as

$$T^2 = \{(\xi_1, \xi_2)| -1 \leq \xi_1, \xi_2; \xi_1 + \xi_2 \leq 0\}$$

and a quadrilateral element defined as,

$$Q^2 = \{(\xi_1, \xi_2)| -1 \leq \xi_1, \xi_2 \leq 1\}$$

Inspection reveals that the coordinates of the triangular region are not bounded by constant limits. This fact implies that another mapping is required. The second mapping serves to define a triangular region whose limits are bounded and constant. Upon completion of the second mapping, one-dimensional Gauss quadrature can be employed, with the two-dimensional nodal points appearing through a tensor product.

The quadrilateral region, Q^2, exhibits the required attribute of boundedness. Noting this, a suitable coordinate system would arise by mapping the local triangular domain to a local quadrilateral domain in a new coordinate system.

Why the need for constant limits? As a consequence of this stipulation, two mappings must occur and therefore the complexity of the scheme increases? The reasoning is two fold.

- The basis proposed by Dubiner consists of a product of tensors, which need constant bounded coordinates in order to computationally efficient.
- Numerical operations, such as integration and differentiation, can be performed more efficiently on a bounded system, as the limits of the integration are fixed.

To emphasise the latter point, consider the relationship between integration in the two known coordinate systems, i.e. after one mapping we have, for a smooth function $f(x, y)$

$$\int_D f(x,y)dxdy = \int_I f(\xi_1,\xi_2)\boldsymbol{J}d\xi_1 d\xi_2 = \int_{-1}^{1}\int_{-1}^{\xi_1+\xi_2=0} f(\xi_1,\xi_2)\boldsymbol{J}d\xi_1 d\xi_2 \tag{5.6}$$

The upper limit, of the final integral, is clearly variable, hence numerical integration becomes expensive and therefore avoidable. Equation (5.6) also serves to introduce the first of the two transformation Jacobians, $\boldsymbol{J}$.

The first Jacobian

For the first mapping, we have

$$DET(\boldsymbol{J}) = DET(\frac{\partial(x,y)}{\partial(\xi_1,\xi_2)}) = \begin{vmatrix} \frac{\partial x}{\partial \xi_1} & \frac{\partial y}{\partial \xi_1} \\ \frac{\partial x}{\partial \xi_2} & \frac{\partial y}{\partial \xi_2} \end{vmatrix} \tag{5.7}$$

where

$$\frac{\partial x}{\partial \xi_2} = \frac{x_3 - x_1}{2}, \quad \frac{\partial x}{\partial \xi_1} = \frac{x_2 - x_1}{2}, \quad \frac{\partial y}{\partial \xi_2} = \frac{y_3 - y_1}{2}, \quad \frac{\partial y}{\partial \xi_1} = \frac{y_2 - y_1}{2} \tag{5.8}$$

The determinate of the Jacobian is thus given by

$$DET(\boldsymbol{J}) = \frac{x_2 - x_1}{2}\frac{y_3 - y_1}{2} - \frac{x_3 - x_1}{2}\frac{y_2 - y_1}{2} \tag{5.9}$$

which is also equivalent to half the area of the element.

Divergence

In this new metric, the divergence of a vector field $\boldsymbol{F} = (F_x, F_y)$ becomes

$$\nabla \cdot \boldsymbol{F} = \frac{1}{\boldsymbol{J}}[\frac{\partial}{\partial \xi_1}(\boldsymbol{JF} \cdot \nabla \xi_1) + \frac{\partial}{\partial \xi_2}(\boldsymbol{JF} \cdot \nabla \xi_2)] \tag{5.10}$$

This provides a shorthand representation of the divergence in the new coordinate system.

5.5.2 The second mapping

The second mapping results in local elements with constant independent limits. The element defined in this final coordinate system has the local coordinates (η_1, η_2). This coordinate system is achieved from the transformation

$$\eta_1 = \frac{2(1+\xi_1)}{1-\xi_2} - 1 \qquad \eta_2 = \xi_2 \tag{5.11}$$

The inverse of which allows any point in the (η_1, η_2) coordinate system to be expressed in terms of the (ξ_1, ξ_2) coordinate system as

$$\xi_1 = \frac{(1+\eta_1)(1-\eta_2)}{2} - 1 \qquad \xi_2 = \eta_2 \tag{5.12}$$

The inverse transformation is employed when calculating the associated transformation Jacobian matrix $\tilde{\boldsymbol{J}}$. In this, the third coordinate system, the local coordinates have the desired, dual, properties of being bounded, and of representing the triangular element of the initial cartesian system.

$$T^2 = \{(\eta_1, \eta_2) | -1 \leq \eta_1, \eta_2 \leq 1\}$$

Effectively, the second transformation maps the vertical lines of the rectangular element (lines of constant η_1) onto the lines radiating out of the point $(\xi_1 = -1, \xi_2 = 1)$ in the triangular element. The triangular region can be defined by a ray coordinate η_1, with $\xi_2 = \eta_2$. Therefore, the triangular element defines a Cartesian quadrilateral.

Graphically this may seem misleading, the mathematical definition of the triangular region, T^2, is identical to that of the quadrilateral region, Q^2. It is best to view the transformation (5.11) as a mapping from the triangular region to a quadrilateral region in the (η_1, η_2) coordinate system.

Proof of bounded constant limits

As is now known, the requirement of bounded local coordinates is essential to efficiency of the scheme. The proof that follows, detailed in [4], provides the verification that the local coordinates, employed in this thesis, are indeed bounded by constant limits.

Consider Figure (5.1). Here it is implied that $\eta_1 = -1$ along the line $\xi_1 = -1$ and has a value equal to 1 along the line $\xi_1 + \xi_2 = 0$ **except** at the point $\xi_1 = -1, \xi_2 = 1$, where it is multi-valued (referred to as a Ray coordinate). It is important to show that ξ_1 is bounded at this point, and consequently prove the local coordinates are bounded everywhere. This proof is performed by setting $\xi_1 = -1 + \epsilon sin\theta$ and $\xi_2 = 1 - \epsilon cos\theta$. Substituting into (5.11) to give

$$\eta_1 = \frac{2(1-1+\epsilon\sin\theta)}{(1-1+\epsilon\cos\theta)} - 1 = 2\tan\theta - 1$$

As $0 \leq \theta \leq \pi/4$ then $0 \leq \theta \leq 1$ and η_1 is also bounded by these limits. Defining the collapsed

coordinate system, allows for tensorial type expansions to be developed.

The second Jacobian

The second change in coordinate system introduces the transformation Jacobian $\tilde{\boldsymbol{J}}$

$$DET(\tilde{\boldsymbol{J}}) = DET(\frac{\partial(\xi_1, \xi_2)}{\partial(\eta_1, \eta_2)}) = \begin{vmatrix} \frac{\partial \xi_1}{\partial \eta_1} & \frac{\partial \xi_2}{\partial \eta_1} \\ \frac{\partial \xi_1}{\partial \eta_2} & \frac{\partial \xi_2}{\partial \eta_2} \end{vmatrix} = \frac{1 - \eta_2}{2} \tag{5.13}$$

The matrix $\tilde{\boldsymbol{J}}$, and its determinant, are easier to compute than $\boldsymbol{J}$ (and its respective determinant) and is free of the requirement of straight edges.

5.5.3 Development of bases

Having produced the collapsed coordinate system, the basis proposed by Dubiner can now be presented . The basis arose due to the need of a high-order representation upon both a structured and unstructured grid. Only the latter, unstructured expansions, are considered here.

The unstructured expansion basis is a product of a one dimensional tensor $\psi_i(z)$ and a two-dimensional tensor, $\psi_{ij}(z)$. The unstructured basis is given by

$$\phi_{ij}(\xi_1, \xi_2) = \psi_i(\eta_1)\psi_{ij}(\eta_2) \tag{5.14}$$

where the functions $\psi_i(\eta_1)$ and $\psi_{ij}(\eta_2)$ are technically referred to as the *orthogonal principal functions*[2].

Inspection reveals that the basis, ϕ_{ij}, is a function of (ξ_1, ξ_2) but the basis is actually calculated in terms of the collapsed coordinate system (η_1, η_2), by using equation (5.12)

5.5.4 Orthogonal principal functions

The principal functions,ψ_i and ψ_{ij}, that comprise the basis are defined by

$$\psi_i(\eta_1) = P_i^{0,0}(\eta_1) \tag{5.15}$$

[2]for the three dimensional case $\psi_{ij\gamma}(t)$ is included, which is a three dimensional tensor. The basis is a product of all three tensors

$$\psi_{ij}(\eta_2) = \frac{(1-\eta_2)^i}{2} P_j^{2i+1,0}(\eta_2) \tag{5.16}$$

where P is the Jacobian polynomial (stated below). The product of equation (5.15) and equation (5.16) yields the original L^2 orthogonal Dubiner basis,

$$\phi_{ij}(\xi_1,\xi_2) = P_i^{0,0}(\eta_1)\frac{(1-\eta_2)^i}{2} P_j^{2i+1,0}(\eta_2) \tag{5.17}$$

Inspection of equation (5.1) reveals that the derivative, with respect to both coordinates, is also required. The derivatives of the basis are given by

$$\frac{\partial \phi_{ij}(\xi_1,\xi_2)}{\partial \eta_1} = \frac{\partial P_i^{0,0}(\eta_1)}{\partial \eta_1}\frac{(1-\eta_2)^i}{2} P_j^{2i+1,0}(\eta_2) \tag{5.18}$$

$$\frac{\partial \phi_{ij}(\xi_1,\xi_2)}{\partial \eta_2} = P_i^{0,0}(\eta_1)[\frac{(1-\eta_2)^i}{2}\frac{\partial P_j^{2i+1,0}(\eta_2)}{\partial \eta_2} - \frac{i}{2}P_j^{2i+1,0}(\eta_2)\frac{(1-\eta_2)^{(i-1)}}{2}] \tag{5.19}$$

5.5.5 Jacobi polynomials

The Legendre polynomials, $P_i^{0,0}$, were defined in Chapter 4. The k^{th} order Jacobi polynomial is generated from the expression.

$$P_k^{\alpha,\beta}(\xi) = \frac{1}{2^k}\sum_{i=0}^{k}\begin{pmatrix} k+\alpha \\ i \end{pmatrix}\begin{pmatrix} k+\beta \\ k-i \end{pmatrix}(\xi-1)^{k-i}(\xi+1)^i \tag{5.20}$$

The derivatives of the polynomial, required for the area integral, are given by

$$b_{1,k}\frac{dP_k^{\alpha,\beta}(\xi)}{d\xi} = b_{2,k}P_k^{\alpha,\beta}(\xi) + b_{3,k}P_{k-1}^{\alpha,\beta}(\xi) \tag{5.21}$$

where

$$b_{1,k} = (2k+\alpha+\beta)(1-\xi^2) \qquad b_{2,k} = k(\alpha-\beta-(2k+\alpha+\beta)\xi) \qquad b_{3,k} = 2(k+\alpha)(k+\beta) \tag{5.22}$$

5.5.6 Polynomial space

If the polynomial basis is denoted by $\phi_{ij}(\xi_1, \xi_2)$, then the polynomial space, $\mathcal{P}_L$, in which the Dubiner basis is complete, is defined by

$$\mathcal{P}_L = Span\{\xi_1^i, \xi_2^j\}_{ij \in \mathcal{Q}} \tag{5.23}$$

where

$$\mathcal{Q} = \{(ij) | 0 \leq i, j; i < L, i + j < M\}, \qquad L \leq M \tag{5.24}$$

Here L and M represent the order of approximation. As the computational domain is given by $\Omega = \bigcup_i T_i$ and elements overlap on edges only, it can be stated that the approximation space is defined by

$$\mathcal{S}_\delta = \{W \in L_2(\Omega) : W|T_i \in \mathcal{P}(T_i) \forall T_i\} \tag{5.25}$$

where the approximate solution, over each element e, $\boldsymbol{U}_a^e$, and test function W are such that: $N \in \mathcal{S}_\delta$ and $\boldsymbol{U}_a \in \mathcal{S}_\delta$

5.5.7 The approximate solution

The unknown vector, $\boldsymbol{U}$, is approximated in each triangular domain, e,by

$$\boldsymbol{U} \approx \boldsymbol{U}_a^e = \sum_{ij} \tilde{\boldsymbol{U}}_{ij} \phi_{ij}(\xi_1, \xi_2) \tag{5.26}$$

where $\tilde{\boldsymbol{U}}_{ij}$ is the expansion coefficient corresponding to the polynomial $\phi_{ij}(\xi_1, \xi_2)$.

5.5.8 The number of unknowns

The the minimum number of unknowns, to form a complete basis, per element, is provided by the formula

$$DoF = \frac{(1 + order)(2 + order)}{2} \tag{5.27}$$

The degrees of freedom (DoF) and are used as the unknown coefficients.

5.6 The area integral

The area-integral, expressed in terms of the new coordinate system, becomes

$$\frac{1}{4}\int_{-1}^{1}\int_{-1}^{1}[[2(y_3-y_1)+(y_1-y_2)(1+\eta_1)]\frac{\partial N}{\partial \eta_1}+(y_1-y_2)(1-\eta_2)\frac{\partial N}{\partial \eta_2}] \quad \boldsymbol{F}_1 \tag{5.28}$$

$$+[2(x_1-x_3)+(x_2-x_1)(1+\eta_1)]\frac{\partial N}{\partial \eta_1}+(x_2-x_1)(1-\eta_2)\frac{\partial N}{\partial \eta_2}] \quad \boldsymbol{F}_2 \tag{5.29}$$

$$d\eta_1 d\eta_2 \tag{5.30}$$

5.7 Evaluation of the mass matrix

The mass matrix reappears here in far more complex form

$$\int_{\Omega_e} N_i N_j d\Omega = \int_{\Omega_e} N_i N_j |\tilde{\boldsymbol{J}}||\boldsymbol{J}|\, d\eta_1 d\eta_2 \tag{5.31}$$

where $\boldsymbol{J}$ and $\tilde{\boldsymbol{J}}$ denote the previously defined Jacobians from the first mapping and second mappings respectively. Due to the orthogonality of the basis, the resulting matrix, acquired from equation (5.31) is diagonal, so that inversion is therefore trivial, and achieved by division.

5.8 Characteristic decomposition

Prior to discussing the implementation of the boundary conditions, it is necessary to define the local characteristic decomposition. Consider the matrix $\boldsymbol{A}_n$ where

$$\boldsymbol{A}_n = \sum_{i=1}^{2} n_i \frac{\partial \boldsymbol{F}^i}{\partial \boldsymbol{U}} = n_x \frac{\partial \boldsymbol{F}^1}{\partial \boldsymbol{U}} + n_y \frac{\partial \boldsymbol{F}^2}{\partial \boldsymbol{U}} \tag{5.32}$$

Expressed in full this becomes

$$\boldsymbol{A}_n = \begin{pmatrix} 0 & 0 & 0 \\ 0 & 0 & n_x \\ 0 & n_x & 0 \end{pmatrix} + \begin{pmatrix} 0 & 0 & -n_y \\ 0 & 0 & 0 \\ -n_y & 0 & 0 \end{pmatrix} \tag{5.33}$$

where $\boldsymbol{n} = (n_x, n_y)$ is the unit normal vector. The eigenvalues are computed via the characteristic equation,

$$|\lambda I - \boldsymbol{A}_n| = \begin{vmatrix} \lambda & 0 & n_y \\ 0 & \lambda & -n_x \\ n_y & -n_x & \lambda \end{vmatrix} = 0 \tag{5.34}$$

where I denotes the corresponding identity matrix. From (5.34) we get

$$\lambda(\lambda^2 - n_x^2) + n_y(-\lambda n_y) = 0 \tag{5.35}$$

$$\Rightarrow \lambda^3 - \lambda n_x^2 - \lambda n_y^2 = 0 \tag{5.36}$$

$$\Rightarrow \lambda(\lambda^2 - 1) = 0 \tag{5.37}$$

So that the eigenvalues of the matrix, $\boldsymbol{A}_n$, are

$$\lambda_1 = -1 \qquad \lambda_2 = 0 \qquad \lambda_3 = 1 \tag{5.38}$$

The eigenvalues are essential to the boundary treatment, particularly when deriving the numerical flux.

5.9 Boundary conditions

The boundary conditions are imposed through the boundary integral

$$\int_{\Gamma_e} \boldsymbol{F}^n N_i d\Gamma = \int_{\Gamma_e} \begin{bmatrix} \boldsymbol{n} \wedge \boldsymbol{E}_*^s \\ -\boldsymbol{n} \wedge \boldsymbol{H}_*^s \end{bmatrix} N_i d\Gamma \tag{5.39}$$

Where Γ represents the edge/boundary of the element. The right-hand side of integral (5.39) is employed for determining both near and far field conditions. The internal boundaries, however, are to be imposed via the Roe flux.

5.9.1 Roe flux

To determine the Roe flux, we need to find the component parts of equation (3.36). Our starting point, in finding the matrix $|\boldsymbol{A}|$, is equation (5.33)

$$\boldsymbol{A}_n = \begin{pmatrix} 0 & 0 & -n_y \\ 0 & 0 & n_x \\ -n_y & n_x & 0 \end{pmatrix} = \boldsymbol{P} \begin{bmatrix} -1 & & \\ & 0 & \\ & & 1 \end{bmatrix} \boldsymbol{P}^{-1} \tag{5.40}$$

We then continue by using the eigenvectors of $\boldsymbol{A}_n$ to form the matrix $\boldsymbol{P}$

For $\lambda = -1$

$$\begin{pmatrix} -1 & 0 & -n_y \\ 0 & -1 & n_x \\ -n_y & n_x & -1 \end{pmatrix} \tag{5.41}$$

solving yields $\boldsymbol{v}_1 = (n_y, -n_x, 1)$

For $\lambda = 0$

$$\begin{pmatrix} 0 & 0 & -n_y \\ 0 & 0 & n_x \\ -n_y & n_x & 0 \end{pmatrix} \tag{5.42}$$

again, upon solving $\boldsymbol{v}_2 = (n_x, n_y, 0)$

For $\lambda = 1$

$$\begin{pmatrix} 1 & 0 & -n_y \\ 0 & 1 & n_x \\ -n_y & n_x & 1 \end{pmatrix} \tag{5.43}$$

solving yields $\boldsymbol{v}_3 = (-n_y, n_x, 1)$. The matrix $\boldsymbol{P}$ becomes

$$\boldsymbol{P} = \begin{pmatrix} -n_y & n_x & n_y \\ n_x & n_y & -n_x \\ 1 & 0 & 1 \end{pmatrix} \tag{5.44}$$

with

$$\boldsymbol{P}^{-1} = \frac{1}{2} \begin{pmatrix} -n_y & n_x & 1 \\ 2n_x & 2n_y & 0 \\ n_y & -n_x & 1 \end{pmatrix} \tag{5.45}$$

The matrix $|\boldsymbol{A}|$ can now be determined.

$$|\boldsymbol{A}| = \boldsymbol{P}|\Lambda|\boldsymbol{P}^{-1} = \begin{pmatrix} n_y^2 & -n_x n_y & 0 \\ -n_x n_y & n_x^2 & 0 \\ 0 & 0 & 1 \end{pmatrix} \tag{5.46}$$

The final form of Roe flux is given by,

$$\boldsymbol{F}^{roe}(\boldsymbol{U}_L, \boldsymbol{U}_R) = \frac{1}{2}\left((\boldsymbol{F}^n{}_R + \boldsymbol{F}^n{}_L) - |\boldsymbol{A}|\,(\boldsymbol{U}_R - \boldsymbol{U}_L)\right) \tag{5.47}$$

$$\boldsymbol{F}^{roe}(\boldsymbol{U}_L, \boldsymbol{U}_R) = \frac{1}{2} \begin{pmatrix} -n_y H_z^R - n_y H_z^L - n_x n_y E_y^L + n_y^2 E_x^L - n_y^2 E_x^R + n_y n_x E_y^R \\ n_x H_z^R + n_x H_z^L + n_x^2 E_y^L - n_y n_x E_x^L + n_y n_x E_x^R - n_x^2 E_y^R \\ H_z^R + H_z^L + n_x E_y^L - n_y E_x^L + n_x E_y^R - n_y E_x^R \end{pmatrix} \tag{5.48}$$

where L and R denote the left- and right-hand-side elements sharing an (internal) edge (in a counter-clockwise manner) and the normal vector $\boldsymbol{n}$ is outwardly pointing.

5.9.2 Near and far-field boundary conditions

Clearly, the evaluation of integral (5.39) is dependent upon the terms $\boldsymbol{n} \wedge \boldsymbol{E}_*^s$ and $\boldsymbol{n} \wedge \boldsymbol{H}_*^s$, as dipected in figure 3.1. These terms are found via the use of characteristic boundary analysis [76]. Characteristic

boundary conditions [77] are employed primarily due to the simplicity involved, but their failing point is that they are only accurate for close to perpendicular incident waves [78]. And result in boundary conditions that are only imposed in a weak sense. The accuracy achieved via this type of boundary treatment is not as high as the far field treatment presented in the subsequent chapter.

5.9.3 Perfect electrical conducting boundary

The first boundary condition under consideration is the near field. In this thesis the scatterer is to be replaced with a perfect electric conductor. Referring to figure (3.1) (for clarity of sub- and superscripts) and substituting equation (2.19) into equation (2.24) results in

$$\mathbf{n} \times \mathbf{E}^s = -\mathbf{n} \times \mathbf{E}^i \qquad \mathbf{n} \cdot \mathbf{H}^s = -\mathbf{n} \cdot \mathbf{H}^i \tag{5.49}$$

Consider an arbitrary node x that is situated on a PEC boundary. The characteristic boundary treatment allows $\boldsymbol{n} \wedge \boldsymbol{E}_*^s$ and $\boldsymbol{n} \wedge \boldsymbol{H}_*^s$ to be determined at this point x. The Rankine-Hugoniot condition, detailed for the general case in chapter three, along a PEC interface is given by

$$-[|\mathbf{U}|] = [|\mathbf{F}|] \tag{5.50}$$

From equation (5.50) we have, for both the electric and magnetic fields,

$$[|\boldsymbol{H}|] = [|\, \boldsymbol{n} \wedge \boldsymbol{E}|], \qquad [|\boldsymbol{E}|] = -[|\, \boldsymbol{n} \wedge \boldsymbol{H}|]. \tag{5.51}$$

The 'jump' terms are represented by

$$[|\boldsymbol{H}|] = \boldsymbol{H}^* - \boldsymbol{H}^l, \qquad [|\boldsymbol{E}|] = \boldsymbol{E}^* - \boldsymbol{E}^l \tag{5.52}$$

Substituting, accordingly, equations (5.52) into equations (5.51), gives

$$\boldsymbol{n} \wedge \boldsymbol{E}^* = -\boldsymbol{n} \wedge \boldsymbol{E}^i \tag{5.53}$$

$$(\mathbf{H}^* - \mathbf{H}^L) = -\mathbf{n} \wedge (\mathbf{E}^* - \mathbf{E}^L) \tag{5.54}$$

And finally by substituting equation (5.53) into (5.54), and then taking the curl, the desired form is achieved

$$\boldsymbol{n} \wedge \boldsymbol{H}^* = \boldsymbol{n} \wedge \boldsymbol{H}^L + \boldsymbol{n} \wedge (\boldsymbol{n} \wedge [\boldsymbol{E}^i + \boldsymbol{E}^L]) \tag{5.55}$$

And so for the TE case,

$$\begin{bmatrix} \boldsymbol{n} \wedge \boldsymbol{E}^s_* \\ -\boldsymbol{n} \wedge \boldsymbol{H}^s_* \end{bmatrix} = \begin{pmatrix} -n_y H^L_z \\ n_x H^L_z \\ -n_x E^i_y + n_y E^i_x \end{pmatrix} - \begin{pmatrix} n_y(n_x E^L_y - n_y E^L_x + n_x E^i_y - n_y E^i_x) \\ n_x(n_x E^L_y - n_y E^L_x - n_x E^i_y + n_y E^i_x) \\ 0 \end{pmatrix} \tag{5.56}$$

Here L denotes the value on the left hand side of the characteristic (refer to figure 3.1) and i represents the incident field.

5.9.4 Far field

To ensure that no waves are reflected back into the computational domain and thereby contamination the solution, a far field condition is to be enforced. Initially the far field condition is enforced with the use of the The Rankine-Hugoniot conditions. The far field is better represented later in the thesis.

The far field condition is represented along the interface where $\lambda = 1$. Substituting for $\lambda = 1$ in the Rankine-Hugoniot equation we get

$$[|\,\mathbf{H}|\,] = [|\,\mathbf{n} \wedge \mathbf{E}|\,] \qquad [|\,\mathbf{E}|\,] = -[|\,\mathbf{n} \wedge \mathbf{H}|\,] \tag{5.57}$$

Once again the jump can be represented by,

$$[|\boldsymbol{H}|] = \mathbf{H}^R - \mathbf{H}^{**} \qquad [|\boldsymbol{E}|] = \mathbf{E}^R - \mathbf{E}^{**} \tag{5.58}$$

Upon substitution of equations (5.58) into (5.57), the following expressions are derived,

$$(\mathbf{H}^R - \mathbf{H}^{**}) = \mathbf{n} \wedge (\mathbf{E}^R - \mathbf{E}^{**}) \tag{5.59}$$

$$(\mathbf{E}^R - \mathbf{E}^{**}) = \mathbf{n} \wedge (\mathbf{H}^R - \mathbf{E}^{**}) \tag{5.60}$$

To reduce the unknowns (thereby increase the simplicity), the conditions from the PEC boundary condition are employed, allied to the material interface conditions, to result in

$$2\boldsymbol{n} \wedge \boldsymbol{E}^* = \boldsymbol{n} \wedge \boldsymbol{E}^L - \boldsymbol{n} \wedge (\boldsymbol{n} \wedge \boldsymbol{H}^L) \tag{5.61}$$

$$2\boldsymbol{n} \wedge \boldsymbol{H}^* = \boldsymbol{n} \wedge \boldsymbol{H}^L + \boldsymbol{n} \wedge (\boldsymbol{n} \wedge \boldsymbol{E}^L) \tag{5.62}$$

The final form of the far field boundary condition, for the TE case, is given by

$$\begin{bmatrix} \boldsymbol{n} \wedge \boldsymbol{E}^s_* \\ -\boldsymbol{n} \wedge \boldsymbol{H}^s_* \end{bmatrix} = \frac{1}{2} \begin{pmatrix} -n_y H^L_z \\ n_x H^L_z \\ n_x E^L_y - n_y E^L_x \end{pmatrix} + \frac{1}{2} \begin{pmatrix} n_y(n_x E^L_y - n_y E^L_x) \\ n_x(n_x E^L_y - n_y E^L_x) \\ H^L_z \end{pmatrix} \tag{5.63}$$

Where L denotes the value on the left hand side of the characteristic (refer to diagram 3.1 for clarity).

5.10 Treatment of boundary integral

Given the theory it still remains a non-trivial task to ensure that the correct procedure upon a boundary edge is being applied. As the basis is calculated in terms η_1 and η_2 careful thought is required when implementing boundary integrals. For correct boundary representation, the edge (from the local triangle in the (ξ_1, ξ_2)-coordinate system) upon which the integration is to be performed must be identified. Once identified, each edge is mapped to a one-dimensional reference edge. A mapping of the general edge to a normalised edge element is now incorporated into the discussion, along with the details required to evaluate an edge integral. Consider the boundary integral

$$\int_{\Gamma_e} \begin{bmatrix} \boldsymbol{n} \wedge \boldsymbol{E}^s_* \\ -\boldsymbol{n} \wedge \boldsymbol{H}^s_* \end{bmatrix} N_i d\Gamma \tag{5.64}$$

This integral, upon completion of the mapping, becomes

$$\int_{\Gamma_e} \begin{bmatrix} \boldsymbol{n} \wedge \boldsymbol{E}^s_* \\ -\boldsymbol{n} \wedge \boldsymbol{H}^s_* \end{bmatrix} N_i d\Gamma = \int_{-1}^{1} \begin{bmatrix} \boldsymbol{n} \wedge \boldsymbol{E}^s_* \\ -\boldsymbol{n} \wedge \boldsymbol{H}^s_* \end{bmatrix} N_i \frac{l}{2} d\gamma \tag{5.65}$$

where $d\gamma$ is edge dependent and l is the length of the edge under analysis, with respect to the original coordinate system. The validity of integral (5.65) is now examined. Consider the transformation given by

$$\begin{bmatrix} \xi_1 \\ \xi_2 \end{bmatrix} = \frac{1}{2}(1-\gamma)\begin{bmatrix} \xi_1^1 \\ \xi_2^1 \end{bmatrix} + \frac{1}{2}(1+\gamma)\begin{bmatrix} \xi_1^2 \\ \xi_2^2 \end{bmatrix} \tag{5.66}$$

where $\gamma\epsilon[-1,1]$. When $\gamma = -1$ let $(\xi_1,\xi_2) = (\xi_1^1,\xi_2^1)$ and when $\gamma = +1$ then the coordinates $(\xi_1,\xi_2) = (\xi_1^2,\xi_2^2)$. Now if we employ the chain rule we get

$$dx = \frac{\partial x}{\partial \xi_1}d\xi_1 + \frac{\partial x}{\partial \xi_2}d\xi_2 \tag{5.67}$$

From equation(5.66) it can be shown that

$$d\xi_1 = \frac{1}{2}(\xi_1^2 - \xi_1^1)d\gamma \qquad d\xi_2 = \frac{1}{2}(\xi_2^2 - \xi_2^1)d\gamma \tag{5.68}$$

Combining equations (5.67) and (5.68) yields

$$\frac{dx}{d\gamma} = \frac{\partial x}{\partial \xi_1}\frac{(\xi_1^2 - \xi_1^1)}{2} + \frac{\partial x}{\partial \xi_2}\frac{(\xi_2^2 - \xi_2^1)}{2} \tag{5.69}$$

Similarly, an expression for $dy/d\gamma$ is given by

$$\frac{dy}{d\gamma} = \frac{\partial y}{\partial \xi_1}\frac{(\xi_1^2 - \xi_1^1)}{2} + \frac{\partial y}{\partial \xi_2}\frac{(\xi_2^2 - \xi_2^1)}{2} \tag{5.70}$$

All that now remains is to express $d\Gamma$ in terms of the new element. Considering the figure (5.1), it can seen by inspection that for any boundary edge of the element

$$d\Gamma^2 = dx^2 + dy^2 \tag{5.71}$$

thus, for any edge,

$$d\Gamma^2 = (\frac{\partial x}{\partial \xi_1}\frac{(\xi_1^2 - \xi_1^1)}{2} + \frac{\partial x}{\partial \xi_2}\frac{(\xi_2^2 - \xi_2^1)}{2})^2 + (\frac{\partial y}{\partial \xi_1}\frac{(\xi_1^2 - \xi_1^1)}{2} + \frac{\partial y}{\partial \xi_2}\frac{(\xi_2^2 - \xi_2^1)}{2})^2 \tag{5.72}$$

Now $d\Gamma$ is derived for each edge that can arise

The horizontal line AB: The horizontal line has end coordinates given by $(\xi_1^1,\xi_2^1) = (-1,-1)$ and $(\xi_1^2,\xi_2^2) = (1,-1)$. Employing equation (5.69) and equation (5.70) yields

$$\frac{dx}{d\gamma} = \frac{\partial x}{\partial \xi_1} \qquad \frac{dy}{d\gamma} = \frac{\partial y}{\partial \xi_1} \tag{5.73}$$

The derivatives $\frac{\partial x}{\partial \xi_1}$ are found, via equation (5.8), as

$$\frac{\partial x}{\partial \xi_1} = -\frac{x_1}{2} + \frac{x_2}{2} \tag{5.74}$$

and, similarly,

$$\frac{\partial y}{\partial \xi_1} = -\frac{y_1}{2} + \frac{y_2}{2} \tag{5.75}$$

Finally, by employing equation (5.72), we find that

$$\frac{d\Gamma}{d\gamma} = \sqrt{(-\frac{x_1}{2} + \frac{x_2}{2})^2 + (-\frac{y_1}{2} + \frac{y_2}{2})^2} = \sqrt{(\frac{x_2}{2} - \frac{x_1}{2})^2} = l/2 \tag{5.76}$$

The expressions for the vertical and diagonal edges are found in an analogous manner.

The diagonal line BC: Here $(\xi_1^1, \xi_2^1) = (1, -1)$ and $(\xi_1^2, \xi_2^2) = (-1, 1)$, giving

$$\frac{d\Gamma}{d\gamma} = \sqrt{(\frac{x_3}{2} - \frac{x_2}{2})^2 + (\frac{y_3}{2} - \frac{y_2}{2})^2} = l/2 \tag{5.77}$$

The vertical line CA: Here $(\xi_1^1, \xi_2^1) = (-1, 1)$ and $(\xi_1^2, \xi_2^2) = (-1, -1)$, leading to

$$\frac{d\Gamma}{d\gamma} = \sqrt{(\frac{x_3}{2} - \frac{x_1}{2})^2 + (\frac{y_3}{2} - \frac{y_1}{2})^2} = \sqrt{(\frac{y_3}{2} - \frac{y_1}{2})^2} = l/2 \tag{5.78}$$

Integrals over these three edges can now be performed.

5.10.1 The basis upon a boundary

There now follows a description for the precise formulation of the basis upon each edge. Upon identification of the edge, where the integral is to be evaluated, it remains to identify (η_1, η_2). The one-dimensional form of the boundary integral implies that one or other of (η_1, η_2) is constant. The constant value of a coordinate can be determined, by inspection, and is dependent upon the edge where the integral is to be evaluated and the choice of quadrature. The basis is defined in terms of the collapsed coordinate system (η_1, η_2), the values of the coordinates on each edge are determined by

inspection and are as follows

The horizontal line AB

$$\xi_1 = \gamma \qquad \xi_2 = -1 \tag{5.79}$$

making use of the transformation from equation (5.11), we get

$$\eta_1 = \gamma \qquad \eta_2 = -1 \tag{5.80}$$

Therefore, for the horizontal edge, we have

$$\sum_{i=1}^{nip} \frac{l}{2} W_i f(\gamma, -1) \tag{5.81}$$

This then provides the approximation to the integral upon this edge of the triangle.

The vertical line CA

$$\xi_1 = \gamma \qquad \xi_2 = -1 \tag{5.82}$$

again making use of the transformation from equation (5.11)

$$\eta_1 = -1 \qquad \eta_2 = \gamma \tag{5.83}$$

again we therefore get,

$$\sum_{i=1}^{nip} \frac{l}{2} W_i f(-1, \gamma) \tag{5.84}$$

The treatment of the boundary integrals is now complete.

The diagonal line BC

$$-\xi_1 = \xi_2 = \gamma \tag{5.85}$$

Once again making use of the transformation from equation (5.11)

$$\eta_1 = 1 \qquad \eta_2 = \gamma \tag{5.86}$$

The approximation for the line integral becomes

$$\sum_{i=1}^{nip} \frac{l}{2} W_i f(1,\gamma) \tag{5.87}$$

Again this expression can be directly incorporated into the scheme to represent the boundary integral upon this edge.

5.11 Treatment of area integral

Consider the area integral

$$\int_e \sum_{j=1}^{2} \frac{\partial W}{\partial x_j} \boldsymbol{F}^j d\Omega \tag{5.88}$$

When considering the variational equation (3.8), as a consequence of evaluating each integral in the collapsed coordinate system, the area integral must be recast in terms of this collapsed coordinate system. The major consideration here is the partial derivative which must undergo two changes of coordinate system.

The first change of coordinate system, from the cartesian (x, y) coordinate system to the local (ξ_1, ξ_2) coordinate system, results in the introduction of a Jacobian. This Jacobian has been derived perviously. The majority of the complexity arises from expressing each derivative in terms of the collapsed coordinate system. To do this the chain rule is applied.

$$\frac{\partial N}{\partial \xi_1} = \frac{\partial N}{\partial x}\frac{\partial x}{\partial \xi_1} + \frac{\partial N}{\partial y}\frac{\partial y}{\partial \xi_1} \qquad \frac{\partial N}{\partial \xi_2} = \frac{\partial N}{\partial x}\frac{\partial x}{\partial \xi_2} + \frac{\partial N}{\partial y}\frac{\partial y}{\partial \xi_2} \tag{5.89}$$

In matrix form, we get

$$\begin{bmatrix} \frac{\partial N}{\partial \xi_1} \\ \frac{\partial N}{\partial \xi_2} \end{bmatrix} = \begin{bmatrix} \frac{\partial x}{\partial \xi_1} & \frac{\partial y}{\partial \xi_1} \\ \frac{\partial x}{\partial \xi_2} & \frac{\partial y}{\partial \xi_2} \end{bmatrix} \begin{bmatrix} \frac{\partial N}{\partial x} \\ \frac{\partial N}{\partial y} \end{bmatrix} \tag{5.90}$$

where the two by two matrix is the Jacobian $\boldsymbol{J}$. The expressions $\frac{\partial N}{\partial x}$ and $\frac{\partial N}{\partial y}$ are easily retrievable from equation (5.89). It follows that

$$\begin{bmatrix} \frac{\partial N}{\partial x} \\ \frac{\partial N}{\partial y} \end{bmatrix} = \boldsymbol{J}^{-1} \begin{bmatrix} \frac{\partial N}{\partial \xi_1} \\ \frac{\partial N}{\partial \xi_2} \end{bmatrix} \tag{5.91}$$

where $\boldsymbol{J}^{-1}$ is the inverse of the Jacobian matrix, $\boldsymbol{J}$, and

$$\boldsymbol{J}^{-1} = \frac{1}{det\ J}\begin{bmatrix} y_3 - y_1 & y_1 - y_2 \\ x_1 - x_3 & x_2 - x_1 \end{bmatrix} \tag{5.92}$$

It is now possible to express the derivative in terms of the (ξ_1, ξ_2) coordinate system. A second mapping must now occur. The newly formed derivative again undergoes a similar treatment. Again, via a variation of equation (5.89), the second mapping from (ξ_1, ξ_2) to (η_1, η_2), yields

$$\begin{bmatrix} \frac{\partial N}{\partial \xi_1} \\ \frac{\partial N}{\partial \xi_2} \end{bmatrix} = \tilde{\boldsymbol{J}}^{-1}\begin{bmatrix} \frac{\partial N}{\partial \eta_1} \\ \frac{\partial N}{\partial \eta_2} \end{bmatrix} \tag{5.93}$$

where

$$\tilde{\boldsymbol{J}} = \begin{bmatrix} \frac{\partial \xi_1}{\partial \eta_1} & \frac{\partial \xi_2}{\partial \eta_1} \\ \frac{\partial \xi_1}{\partial \eta_2} & \frac{\partial \xi_2}{\partial \eta_2} \end{bmatrix} \tag{5.94}$$

Here the inverse of the transformation, equation (5.12), comes to the fore, this equation enables the partial derivatives to be found, such that

$$\begin{bmatrix} \frac{\partial N}{\partial \xi_1} \\ \frac{\partial N}{\partial \xi_2} \end{bmatrix} = \frac{1}{det\tilde{\boldsymbol{J}}}\begin{bmatrix} 1 & 0 \\ \frac{1}{2}(1+\eta_1) & \frac{1}{2}(1-\eta_2) \end{bmatrix}\begin{bmatrix} \frac{\partial N}{\partial \eta_1} \\ \frac{\partial N}{\partial \eta_2} \end{bmatrix} \tag{5.95}$$

The original derivatives are now expressed with respect to the relevant coordinate system.

$$\begin{bmatrix} \frac{\partial N}{\partial x} \\ \frac{\partial N}{\partial y} \end{bmatrix} = \frac{1}{4}\frac{1}{|\boldsymbol{J}||\tilde{\boldsymbol{J}}|}\begin{bmatrix} (y_3 - y_1) & (y_1 - y_2) \\ (x_1 - x_3) & (x_2 - x_1) \end{bmatrix}\begin{bmatrix} 1 & 0 \\ \frac{1}{2}(1+\eta_1) & \frac{1}{2}(1-\eta_2) \end{bmatrix}\begin{bmatrix} \frac{\partial N}{\partial \eta_1} \\ \frac{\partial N}{\partial \eta_2} \end{bmatrix} \tag{5.96}$$

Note that the determinants of the Jacobians will disappear, due to the relationship.

$$dxdy = |\boldsymbol{J}|d\xi_1 d\xi_2 = |\boldsymbol{J}||\tilde{\boldsymbol{J}}|d\eta_1 d\eta_2 \tag{5.97}$$

This completes the treatment for the area integral.

5.12 Polynomial expansions for the continuous modal basis

The basis to be described subsequently would see employment in a ***continuous*** spectral/*hp* Galerkin scheme. The analysis of this basis serves to highlight the deficiencies of the origonal Dubiner basis.

In order that a C^0 continuous basis is constructed the orthogonal functions are decomposed into interior and boundary modes, themselves further reduced into vertex and edge modes. This, allied to the fact that the interior modes are zero on the boundaries, ensures the completeness of the basis [55].

Principal functions of the C^0 continuous basis

$$\psi_i^a(z) = \begin{cases} \frac{(1-z)}{2} & i = 0 \\ \frac{(1-z)}{2}\frac{(1+z)}{2}P_{i-1}^{1,1}(z) & 1 \le i \le I-1 \\ \frac{(1+z)}{2} & i = I \end{cases} \tag{5.98}$$

$$\psi_{ij}^b(z) = \begin{cases} \psi_{j(z)}^a & i = 0, \quad 0 \le j \le J \\ \frac{(1-z)}{2}^{i+1} & 1 \le i \le I-1, \quad j = 0 \\ \frac{(1-z)}{2}^{i+1}\frac{(1+z)}{2}P_{j-1}^{2i+1,1}(z) & 1 \le i \le I-1, \quad 1 \le j \le J-1 \\ \psi_j^a(z) & i = I, \quad 0 \le j \le J \end{cases} \tag{5.99}$$

Employing the triangular expansion, equation (5.14),in conjunction with the above Principle functions for a C^0 continuous basis, allows for the modes at the vertices, the edges and the interior of the element to be derived. Again, it then becomes a matter of identifying where on the element the integral is to be evaluated, so that the appropriate form of the basis can be applied.

Vertex modes

The Vertex modes are given by

$$Vertex\ A: \quad \frac{(1-\eta_1)}{2}\frac{(1-\eta_2)}{2} \tag{5.100}$$

$$Vertex\ B: \quad \frac{(1+\eta_1)}{2}\frac{(1-\eta_2)}{2} \tag{5.101}$$

$$Vertex\ C: \quad \frac{(1+\eta_2)}{2}, \tag{5.102}$$

By inspection it can be seen that the vertex modes are indeed the linear finite element basis, having a value of unity at one vertex and varying linearly to zero at the others.

Edge modes

The edge modes are defined as

$$Edge\ AB: \quad \frac{(1-\eta_1)}{2}\frac{(1+\eta_1)}{2}P_{p-1}^{1,1}(\eta_1)\frac{1-\eta_2}{2}^{p+1} \qquad (0<p<P_1) \tag{5.103}$$

$$Edge\ AC: \quad \frac{(1-\eta_1)}{2}\frac{(1-\eta_2)}{2}\frac{(1+\eta_2)}{2}P_{q-1}^{1,1} \qquad (0<q<P_2) \tag{5.104}$$

$$Edge\ BC: \quad \frac{(1+\eta_1)}{2}\frac{(1-\eta_2)}{2}\frac{(1+\eta_2)}{2}P_{q-1}^{1,1} \qquad (0<q<P_2) \tag{5.105}$$

Inspection reveals that the edge modes contribute from a local edge only, and are zero upon on all other edges (and vertices).

Interior modes

The interior modes, that contribute from a cubic representation and higher, are defined by

$$Interior \ : \quad \frac{(1-\eta_1)}{2}\frac{(1+\eta_1)}{2}P_{p-1}^{1,1}(\eta_1)\frac{1-\xi_2}{2}^{p+1}\frac{(1+\xi_2)}{2}P_{q-1}^{2p+1,1}(\xi_2) \tag{5.106}$$

By inspection it can be seen that the interior modes are zero on the boundary of the triangle.

The C^0 continuous basis is to be compared with the L^2 basis. This comparison will provide evidence that the, as the order of the approximation increases, the C^0 continuous basis will diverge from the exact solution. This analysis will prove the importance of basis selection.

5.12.1 LU decomposition

A direct consequence of employing the C^0 continuous basis is that the mass matrix becomes 'full', so a method of matrix inversion needs to be employed. LU-decomposition provides the means to decompose an $N \times N$ matrix, $\boldsymbol{A}$, into a product of a lower triangular matrix $\boldsymbol{L}$ and an upper triangular matrix $\boldsymbol{U}$, such that the system $\boldsymbol{A}x = \boldsymbol{B}$ can be solved

$$\boldsymbol{LU} = \boldsymbol{A} \tag{5.107}$$

Consider the system below

$$[\underline{\underline{M}}]\ \{\underline{\Delta U}\} = \{\underline{RHS}\} \tag{5.108}$$

The inversion of the matrix $\underline{\underline{M}}$ is sought by LU-decomposition. If we write the consistent matrix $\underline{\underline{M}}$ as a product of $\underline{\underline{L}}$ and $\underline{\underline{U}}$, equation (5.108) becomes

$$([\underline{\underline{L}}][\underline{\underline{U}}])\ \{\underline{\Delta U}\} = \{\underline{RHS}\} \tag{5.109}$$

let

$$[\underline{\underline{U}}]\ \{\underline{\Delta U}\} = \{\underline{B}\} \tag{5.110}$$

therefore, upon substitution

$$[\underline{\underline{L}}]\ \{\underline{B}\} = \{\underline{RHS}\} \tag{5.111}$$

First solve $[\underline{\underline{L}}]\{\underline{B}\} = \underline{RHS}$. The first term is given, than a formula for any entry

$$B(1) = \frac{RHS(1)}{L(1,1)} \tag{5.112}$$

$$B(i) = \frac{1}{L(i,i)}\{RHS(i) - \sum_{j=1}^{i-1} L(i,j)B(j)\} \tag{5.113}$$

for $i = 2, ..., n$. Now solve $\underline{U}\Delta U = \underline{B}$. The solution is achieved by back substitution. The first (or final) entry is given by

$$\Delta U = \frac{B(N)}{U(N,N)} \tag{5.114}$$

$$\Delta U = \frac{1}{U(i,i)}\{B(i) - \sum_{j=i+1}^{N} U(i,j)\Delta U(j) \tag{5.115}$$

This algorithm provides the means to invert the mass matrix.

5.13 Electrical length

The electrical length is a measure of the number of wavelengths which occupy a specified length scale of the scattering body. For the circular scatter's employed in this Chapter the electrical length is given by the diameter. Clearly, the larger the electrical length the greater the computational challenge.

5.14 The radar cross section

The analytic solutions presented in this thesis are obtained from the work of Balanis [30]. Such a derived output is the radar cross section $\chi(\phi)$. The scattering width, or the radar cross section, RCS, per unit length, for a transverse electric problem is defined by

$$\chi(\phi) = \frac{|H_z^s|^2}{|H_z^i|^2} \tag{5.116}$$

and

$$\chi(\phi) = \frac{|E_z^s|^2}{|E_z^i|^2} \tag{5.117}$$

for the TM problem. These expressions cannot be evaluated directly from the computational solution as they require far field data. The use of a near-field to far-field transformation [79] allows the scattering width to be calculated as

$$\chi(\phi) = \frac{\omega}{4}|\int_{\Gamma_c}(W_2\cos\phi - W_1\sin\phi + W_3)e^{i\omega(x'cos\phi+y'sin\phi)}d\Gamma|^2 \tag{5.118}$$

where (x', y') represent the coordinates of a general point on the scatterer and $\boldsymbol{W} = (W_1, W_2, W_3)$ is given by

$$\boldsymbol{W} = \begin{bmatrix} n_y H_z^s \phi \\ -n_x H_z^s \phi \\ n_y E_x^s - n_x E_y^s \end{bmatrix} e^{i\omega(x'cos\phi+y'sin\phi)} \tag{5.119}$$

For the above equations r and ϕ represent the cylindrical polar coordinates of a general observation point in the far field. For a meaningful description of the far field scattering, the scattering width is expressed in decibels. This is achieved by

$$RCS = 10 \log_{10} \Phi(\phi) \tag{5.120}$$

For the results that are to be presented, concerning the RCS, the axis labels are as follows, the horizontal, x, axis denotes ϕ, the cylindrical coordinate and the vertical, y, axis represents the RCS intensity.

5.15 Analytical Solutions

Existing analytical solutions, where they exist, to the scattering problems will be used to verify the numerical simulations. Analytical solutions are available for the TM and TE scattering observed from circular cylinders of infinite extent in the z-direction. Classical texts such as Balanis [30] provide a means to derive the desired analytical solution across the computational domain. The analytic results, used in this thesis, are due to Balanis [30] and can be found, for the transverse magnetic case on page 612 and are given by equation 11-137, similarly for the transverse electric case the exact solutions are to be found on page 625 and are given by equation 11-155.

5.16 Results

5.16.1 Numerical convergence for the PEC

Initially, the numerical convergence of the scattering width is assessed by considering the scattering of 2λ PEC circular discs, for both the TE and TM polarisations (other electric lengths are considered, such as 12λ). The analysis is performed upon the domains depicted by figures (5.3) and (5.4). The analysis then moves on to consider two other forms of scatterer, a PEC cavity figure (5.39) and two PEC aerofoils depicted by figures (5.28) and (5.32).

5.16.2 The meshes

The first mesh to be employed is depicted in figure (5.2). The mesh consists of 15580 elements and is employed for the results of figures (5.5), (5.6) and (5.7). A mesh consisting of this elemental quantity serves to prove that a denser mesh clearly requires a lower order of approximation for an acceptable solution, here an order of p=0 provides an excellent solition.

The figure (5.3) contains 682 unstructured elements and can be considered, along with the 158 element mesh of figure (5.4), as an annulus which has an inner radius of 1λ and an outer radius of 2λ.

The remaining figures have the number of elements from which the meshes are constructed below them.

Convergence upon meshes

Figure (5.8) depicts the numerical convergence of the TM scattering width with polynomial orders of $p = 0, 1, 2, 3, 4$ and 5 on the computational domain depicted in figure (5.3). It is clearly seen that with an increase in the order comes an increase in the symmetry and an ever closer approximation to the exact solution. It is also noted that, for this simulation, once the converged solution is achieved, for $p = 4$, increasing the order of approximation does not provide any notable increase in the accuracy of the result, the scattering width remains constant. Figure (5.9) compares the exact solution with the converged numerical, TM, solution, the comparison is favourable for the RKDG method.

Depicted in figure (5.10), again performed on the 682 element mesh, is the converged transverse electric scattering width distribution, plotted against the exact solution. The results obtained from the TE distributions are in agreement with those obtained from the TM case, in that they compare favourably with the exact solution.

The results obtained by analysing the 158 element mesh, depicted in figure (5.4), are consistent with those exhibited by the 682 element mesh. The difference being, as expected, the comparison between the converged numerical approximation and the exact solution, clearly a better domain representation will provide more accurate results.

Figure (5.11) proves that the numerical solutions, for the TM case, tend to a converged, symmetric, distribution by increasing the polynomial order $p = 0, .., 4$. Figure(5.12) provides a comparison of the converged, $p = 4$ approximation, and the exact solution.

Similarly, for the TE simulation a comparison with the exact solution and the converged numerical solution is provided by figure (5.13).

Figure (5.14) provides a plot for the difference between the exact solution and for $p = 0, .., 4$. As expected this figure shows that as the order increases the difference between the exact solution and the numerical solution tends to zero.

The lack of symmetry exhibited in figure (5.13) is a result of the poor boundary representation, and is investigated in the following chapter where curved elements are introduced.

Figures (5.15) and (5.16) provide a comparison between the 158 and 682 element meshes. The comparison proves that if the order of the approximation is $p = 0$, figure (5.15), then the mesh density, and representation of the near boundary, has an important role. To exemplify this point consider figure (5.16), we see, as expected, that better domain and boundary representation added to more elements per wavelength provide for more accurate numerical solutions. Figure (5.16) shows that as the order

of approximation is increased then the representation of the domain has diminishing effect. Close inspection of figure (5.16) reveals, as expected, that the distribution obtained from the denser mesh provides a more accurate solution, but the difference with the coarser mesh is minimal.

The constant approximation proves that if the solution domain is represented with more elements then a higher accuracy is achieved, but to counter this figure (5.16) shows that an increase in the polynomial order negates the need for a large amount of elements.

5.16.3 Comparison between the L^2 and C^0 Dubiner bases

The mesh chosen for this comparison of bases is again represented by figure (5.3).

The initial comparison, figure (5.17), shows that if a low-order approximation is employed then the numerical distributions are very similar, however as expected (from the theory of Warburton, Lometev [55]) the disparity between the two bases increases with an increase in the order of approximation, this is emphasised in figure (5.18). This increase in error for the C^0 basis is a direct consequence of the fact that the basis is not defined within each element only, the basis for element e adversely affects the numerical approximation in neighbouring element $e + 1$. From this analysis it can be proven that as the order of approximation is increased, for the C^0 continuous basis, the numerical solution diverges from the exact solution.

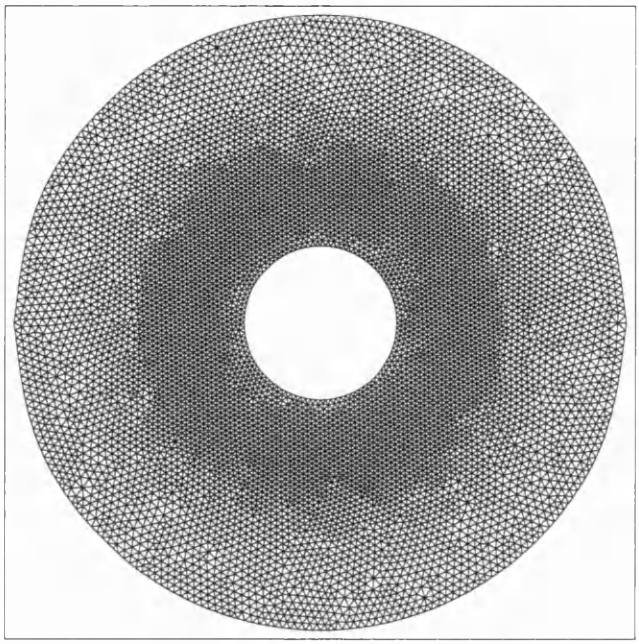

Figure 5.2: Scattering by a circular cylinder of electrical length 2λ: an unstructured mesh consisting of 15580 elements

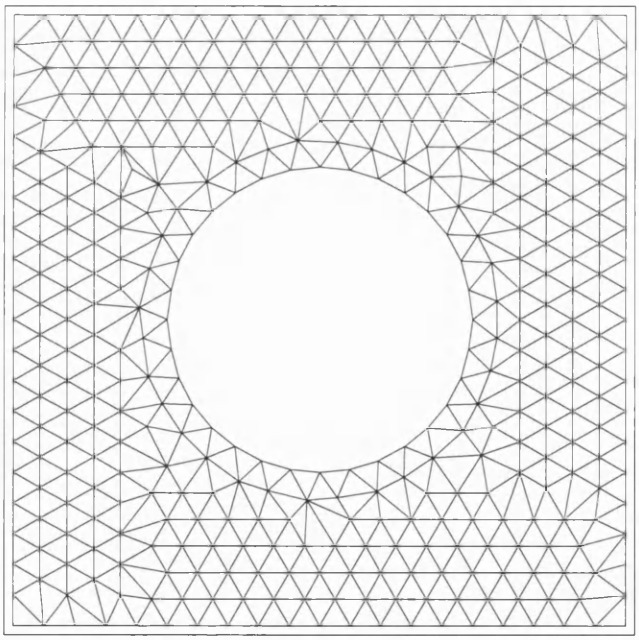

Figure 5.3: Scattering by a circular cylinder of electrical length 2λ: an unstructured mesh of 682 elements

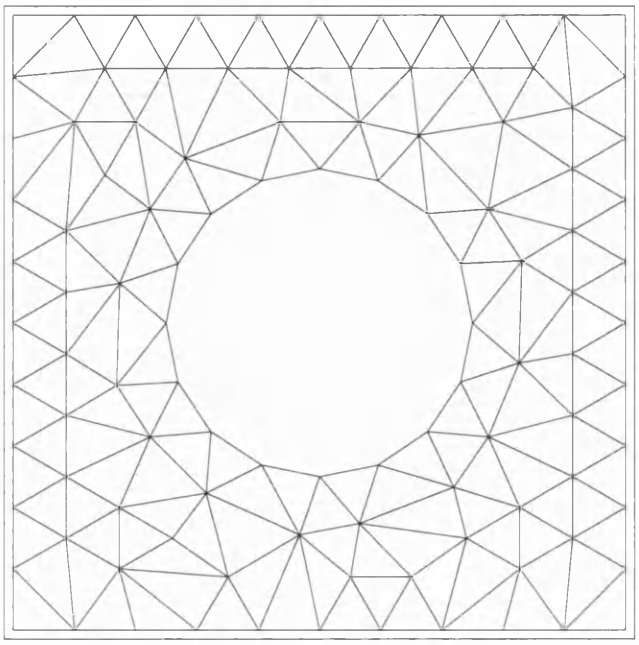

Figure 5.4: Scattering by a circular cylinder of electrical length 2λ: an unstructured mesh of 158 elements

Refinement

The previous chapter saw the imposition of refinement techniques. The results achieved from this analysis proved that an increase in polynomial order is preferable to refining the mesh, this result is to be further analysed here, for two dimensional space.

The refinement procedure employed is of a form consistent with the analysis of the previous chapter, the initial mesh is depicted in figure (5.4), the first refinement is produced by refining this initial mesh by approximately a factor of four (resulting in 650 elements) and the final mesh is achieved by refining the initial mesh by a factor of 16 (in actuality 2514 elements). The results, depicted in figures (5.19-5.24) are consistent with the findings of the previous chapter; high-order representation is preferable to mesh refinement. But to consider this statement further, it is clear that as the polynomial order increases, then so does the computational cost. Naturally as the polynomial order increases, the error, in approximation, decreases and this type of refinement is faster than for simple h refinement. The advantages become more apparent as a higher and higher accuracy levels are required. It is also worth considering that for the levels of accuracy of interest to industry (which could be fairly low) there is little to choose between h and p refinement (this is again evident in the one-dimensional example considered in the previous Chapter.

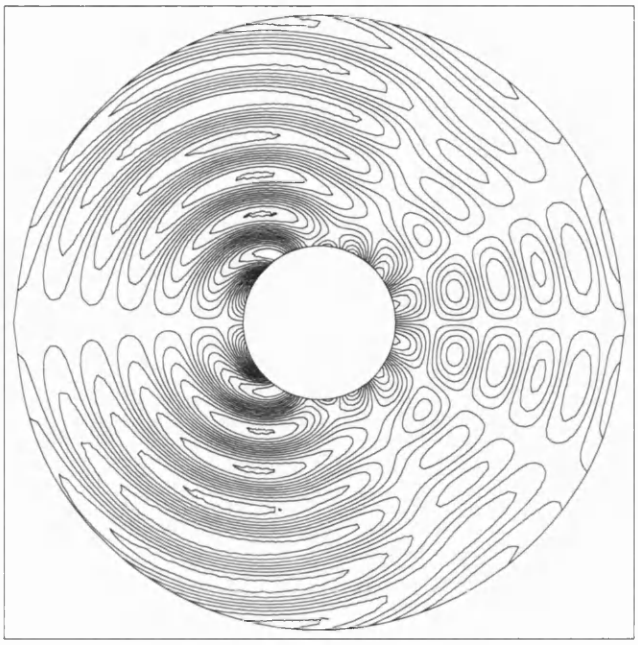

Figure 5.5: Scattering by a circular cylinder of electrical length 2λ: contours of E_x for converged solution of $p = 0$

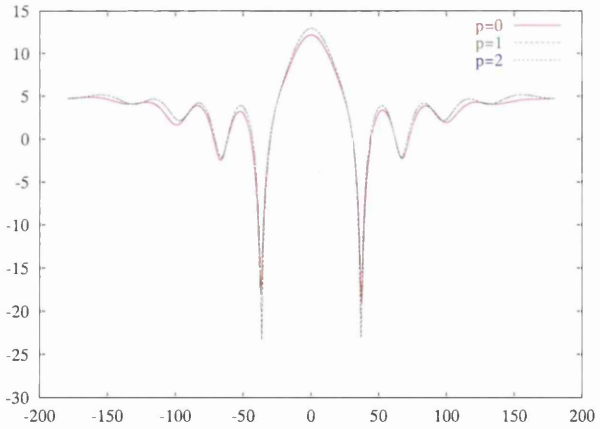

Figure 5.6: Scattering of a TE wave by a circular disc of electrical length 2λ on mesh of 15580 elements: convergence of the RCS distribution with increase in P

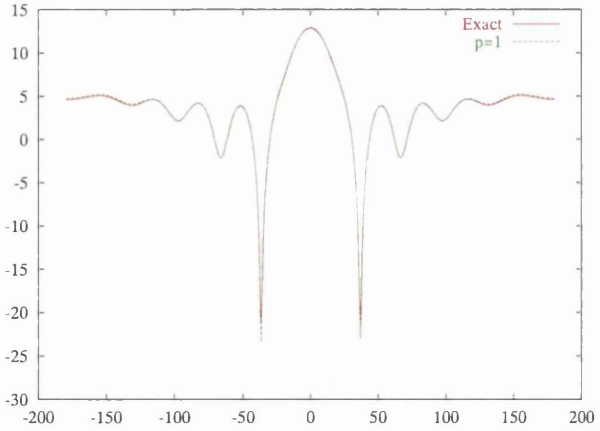

Figure 5.7: Scattering of a TE wave by a circular disc of electrical length 2λ on mesh of 15580 elements: comparison of exact solution with p=1 approximation

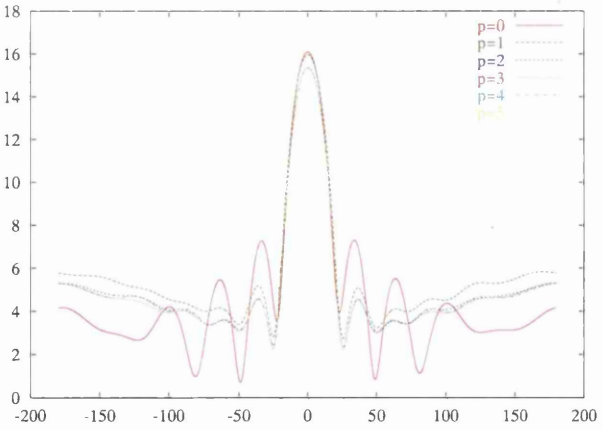

Figure 5.8: Scattering of a TM wave by a circular cylinder of electrical length 2λ on mesh of 682 elements: convergence of the RCS distribution with increase in P

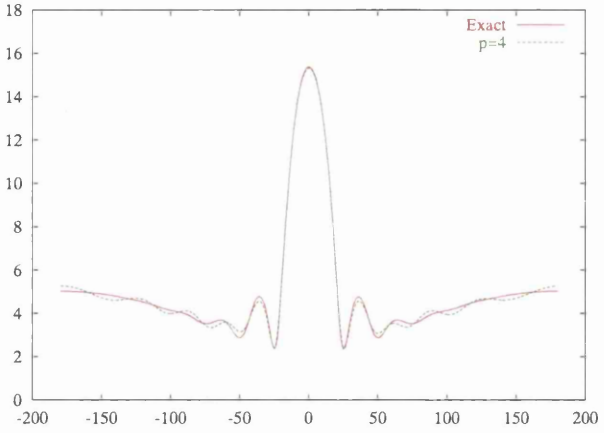

Figure 5.9: Scattering of a TM wave by a circular cylinder of electrical length 2λ: comparison between exact RCS and converged numerical solution on the 682 element mesh

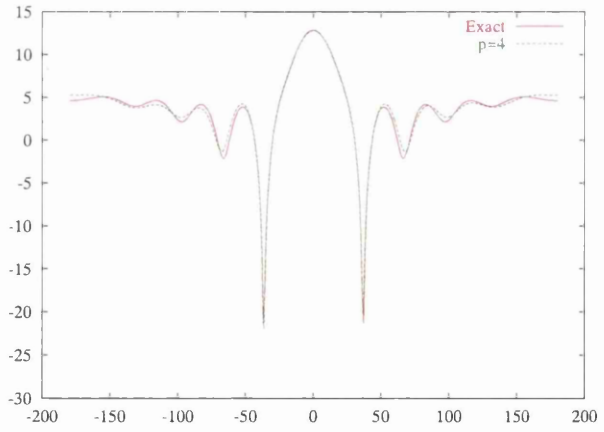

Figure 5.10: Scattering of a TE wave by a circular cylinder of electrical length 2λ: comparison between exact RCS and the converged numerical solution on the 682 element mesh

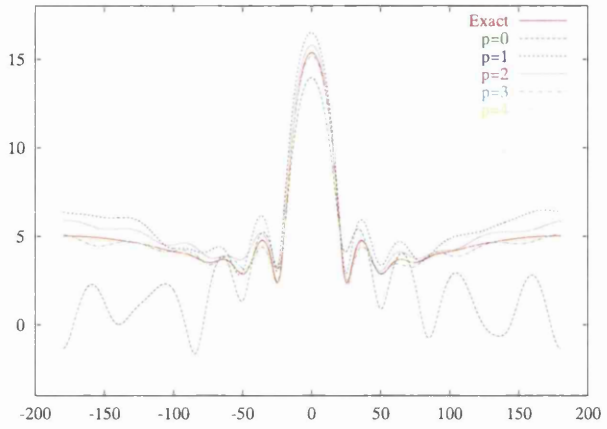

Figure 5.11: Scattering of a TM wave by a circular cylinder of electrical length 2λ on mesh of 158 elements: convergence of the RCS distribution with increase in P

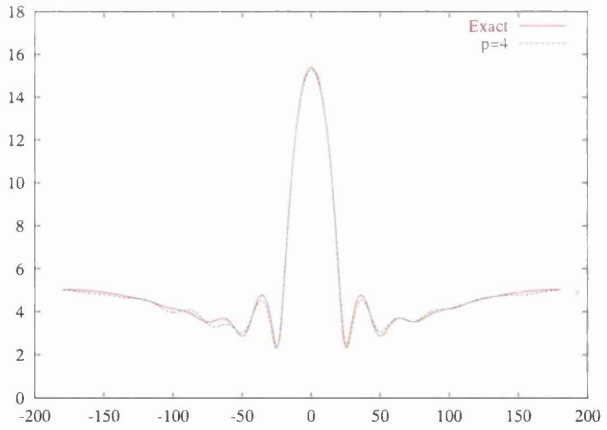

Figure 5.12: Scattering of a TM wave by a circular cylinder of electrical length 2λ: comparison between exact RCS and converged RCS for 158 element mesh

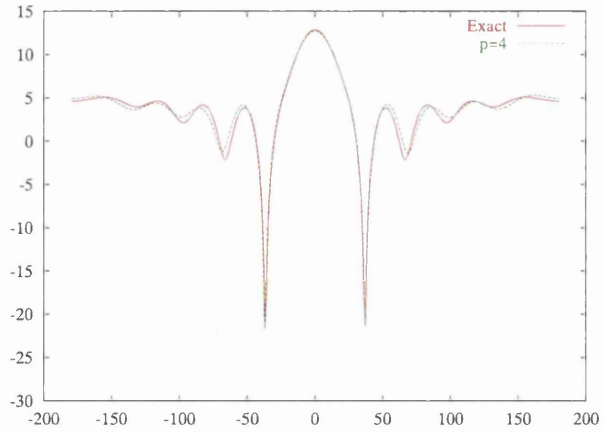

Figure 5.13: Scattering of a TE wave by a circular cylinder of electrical length 2λ: comparison between exact RCS and converged RCS for 158 element mesh

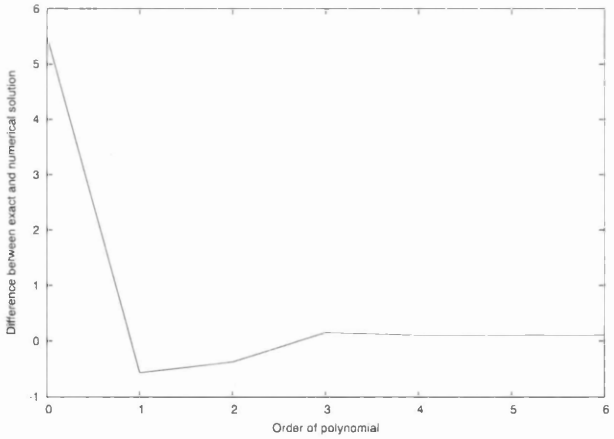

Figure 5.14: Scattering of a TE wave by a circular cylinder of electrical length 2λ on mesh of 158 elements: the difference between the exact solution and that for the range of P values

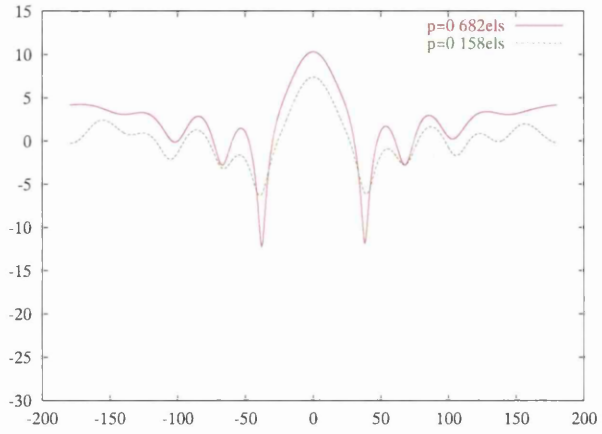

Figure 5.15: Scattering by a circular cylinder of electrical length 2λ: comparison between 682 element mesh RCS and 158 element mesh with a $p = 0$ uniform approximation

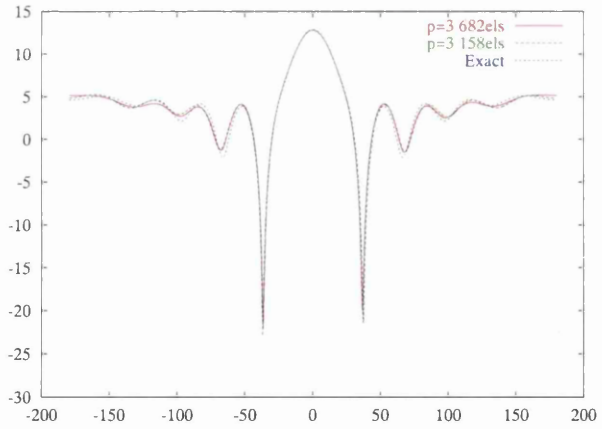

Figure 5.16: Scattering by a circular cylinder of electrical length 2λ: comparison between exact RCS and converged solution for the 682 element mesh and the 158 element mesh, with a $p = 3$ uniform approximation

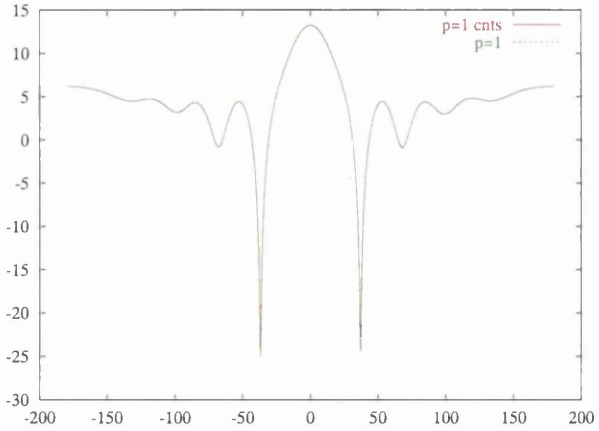

Figure 5.17: Scattering by a circular cylinder of electrical length 2λ: comparison of RCS distributions for the C^0 expansion basis and L^2 basis, with a $p = 1$ approximation

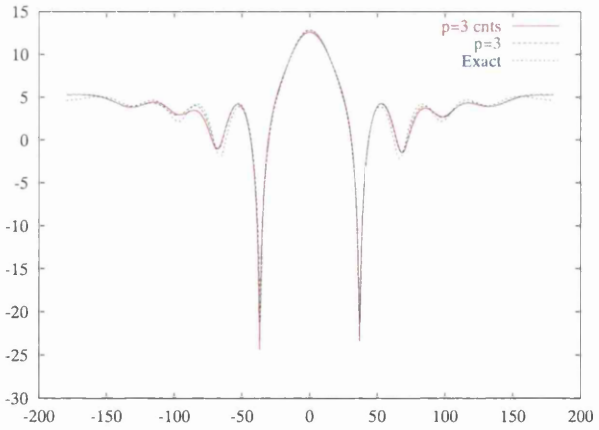

Figure 5.18: Scattering by a circular cylinder of electrical length 2λ: comparison, with the exact solution, of RCS distributions for the C^0 expansion basis and L^2 basis, with $p = 3$

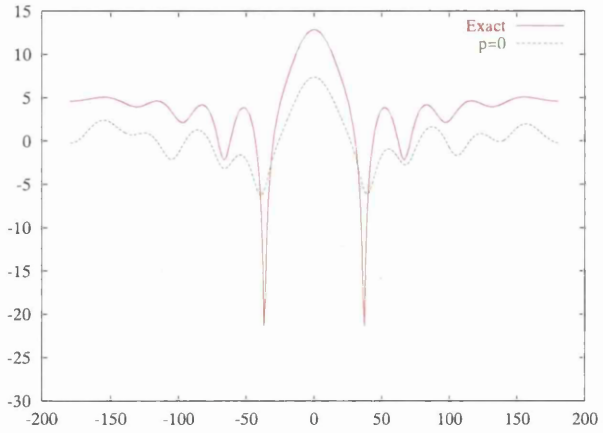

Figure 5.19: Refinement both h and p; scattering of a TE wave by a circular annulus of electrical length 2λ on 158 element mesh: the scattered width distributions for p=0

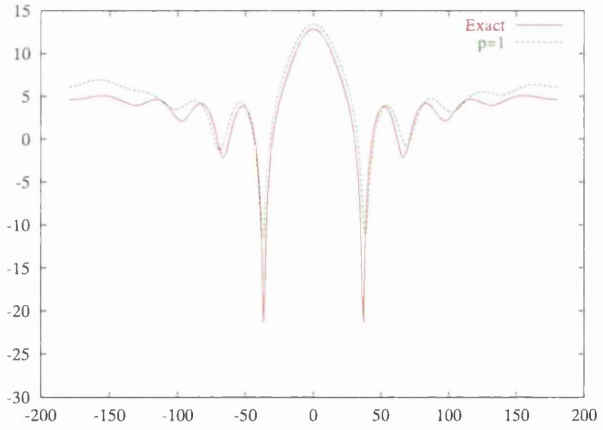

Figure 5.20: p-Refinement; scattering of a TE wave by a circular annulus of electrical length 2λ on 158 element mesh: the scattered width distributions for p=1

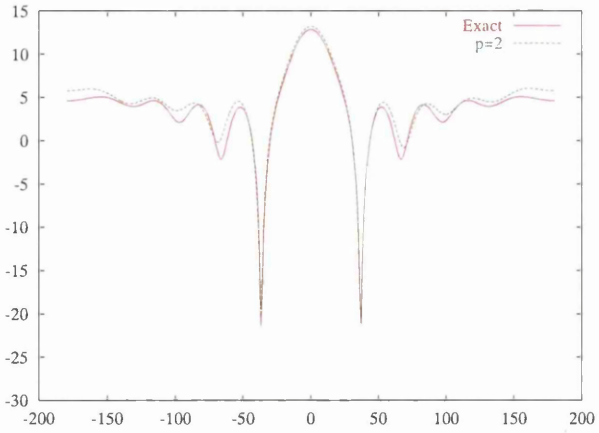

Figure 5.21: p-Refinement; scattering of a TE wave by a circular annulus of electrical length 2λ on 158 element mesh: the scattered width distributions for p=2

5.16.4 Verifying the numerical solutions

Each numerical solution, that involves a PEC disc, and hence the numerical scheme as a whole, is verified by a comparison with the analogous exact solution. The numerical solutions take the form of a scattering width distribution. For the first example, converged 2λ distributions are compared with the corresponding analytical solution.

The comparisons, with the exact solution, involve both the TE and TM polarisations. Figures (5.9), (5.10), (5.12) and (5.13) depict the converged RCS distribution, involving an order $p = 4$ approximation. These distributions are plotted against what would be the exact solution. Inspection of these figures shows that the numerical performance of the 2λ TE and TM scattering problems is excellent. The figure (5.5) shows the contours for the converged TE solution.

Problems of a larger electrical wavelength are more relevant to industry, and are now to be considered. Numerical solutions are sought for circular cylinder of electrical length 10λ.

The computational domain, containing 882 elements, involves a greater element composition than the two previous, investigated, meshes. The increase in elements is a direct consequence of the decrease in λ. The mesh has the same spatial dimensions as the 658 and 158 element meshes; an inner radius of one and outer radius of two, here however λ equals 0.2.

For the simulation where the order of the approximation is $p = 7$, then the numerical results are in excellent accordance with the exact solution, refer to figure (5.26). For the first time an order higher than $p = 5$ was required to produce a converged accurate solution.

Figure (5.27), involves a PEC cylinder of diameter 12λ on the unstructured mesh containing 682

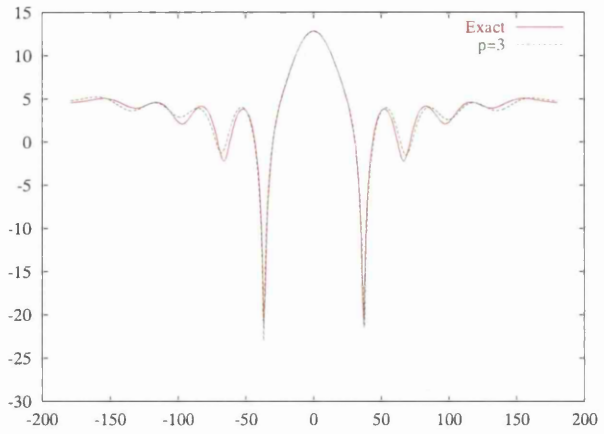

Figure 5.22: p-Refinement; scattering of a TE wave by a circular annulus of electrical length 2λ on 158 element mesh: the scattered width distributions for p=3

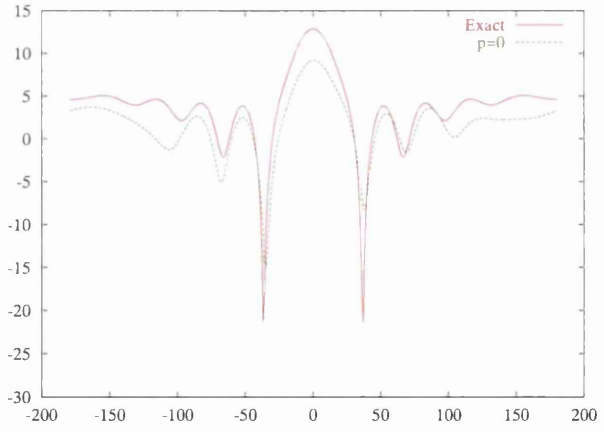

Figure 5.23: h-Refinement; scattering of a TE wave by a circular annulus of electrical length 2λ on first refined mesh of 650 elements: the scattered width distributions for p=0

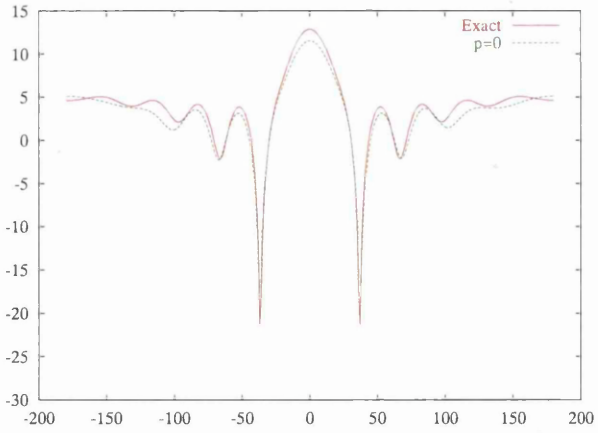

Figure 5.24: h-Refinement; scattering of a TE wave by a circular annulus of electrical length 2λ on final refined meshof 2514 elements: the scattered width distributions for p=0

elements (figure 5.3), the convergence will improve in accuracy with, amongst other factors, a better domain representation on the far field boundary, this is to be investigated in the next chapter.

Figure 5.25: Scattering of a TE wave by a circular cylinder of electrical length 12λ on mesh of 1082 elements: contours of E_x for converged solution

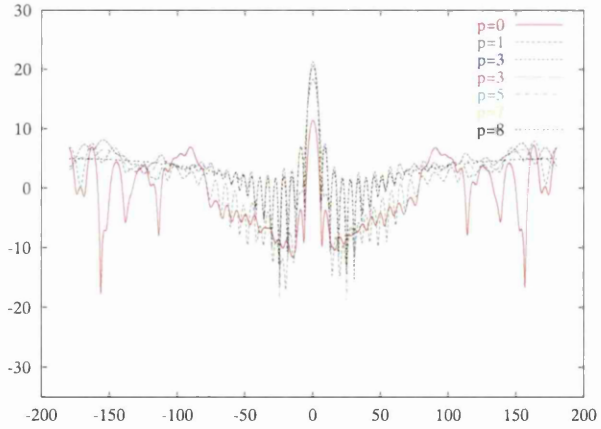

Figure 5.26: Scattering of a TE wave by a cylinder of electrical length 10λ on mesh of 882 elements: convergence of the RCS distribution with increase in P

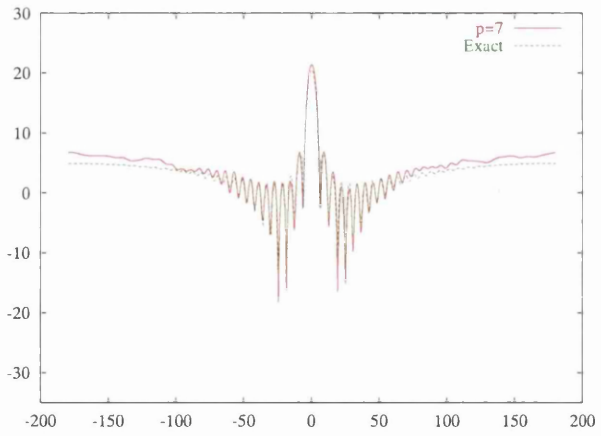

Figure 5.27: Scattering of a TE wave by a cylinder of electrical length 12λ on mesh of 682 elements: the converged RCS distribution compared with the exact solution

5.17 Scattering by two further objects

The perfectly electrical conductors now take a more complex form. The scatterers now consist of objects with no comparable analytical solutions. The simulations are performed upon an open cavity as in figure(5.38) and two aerofoils, one a NACA0012 aerofoil, figure (5.28) and the other a very coarse representation of an aerofoil, termed the NACA aerofoil and depicted in figure (5.30). The meshes are generated via the advancing front technique [80]. The meshes are again unstructured.

5.17.1 The PEC aerofoil

The following analysis involves simulating the scattering of a transverse electric wave by a perfectly conducting NACA aerofoil. The cord length, c, of the scatterer is given by $c = 2\lambda = 1$. The unstructured mesh is compiled from 432 triangular elements. The NACA0012 aerofoil mesh is refined near the leading and trailing edges of the aerofoil. The refinement exists so as to provide the required geometrical definition.

The scattering involves two separate cases. The first simulation involves illumination from the front of the aerofoil and the second, illumination from the rear.

Figure (5.29) depicts the contours achieved by the scattering of the E_y wave upon the NACA0012 aerofoil, depicted in figure (5.28). As with the previous simulations the order of the approximation is increased until a convergence of the RCS is obtained. The figure (5.32) depicts the numerical solution tending to the converged solution as the order of approximation increases. This numerical

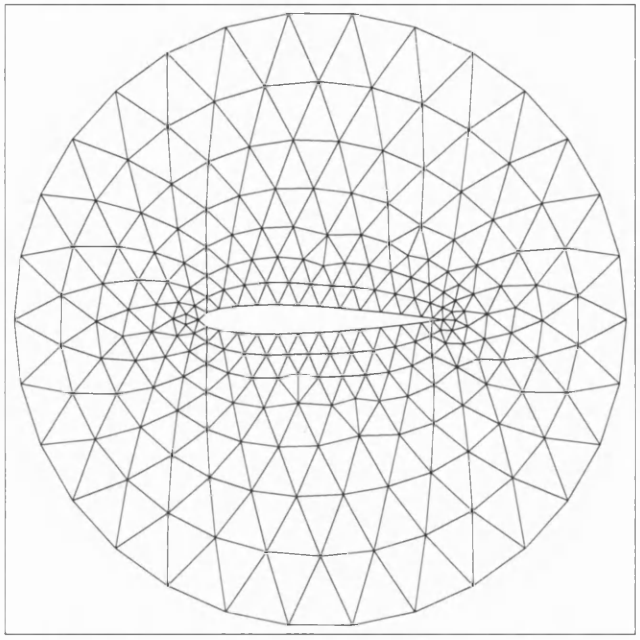

Figure 5.28: Scattering by a NACA0012 aerofoil of electrical length 2λ: the mesh consists of 432 elements

convergence is achieved by, arbitrarily, illuminating the front of the aerofoil.

The coarse NACA mesh is introduced to highlight the fact that as the order of the approximation increases acceptable solutions can be achieved, even upon such a coarse mesh. This fact is proved in the figures (5.31), where the front of the aerofoil is illuminated.

It comparison naturally follows involving the converged numerical solutions achieved from both the coarse NACA and NACA0012 aerofoils. Figures (5.33) and (5.34) provide such a comparison. The comparison, when considering illumination from the front, is good, but when comparing illumination from the rear the comparison is not excellent. This difference again highlights the importance of domain representation, the aerofoil requires more elements at the rear of the aerofoil, as is evident upon examination of figure (5.30) (compared with figure (5.28)). It is worth considering at this point, that the nature of the discontinuous Galerkin method would allow for mesh refinement at in this area (or any area of interest) and/or increased order of representation.

5.17.2 Open cavity

The final simulation is performed upon an semi-open cavity. The cavity consists of two parallel walls connected at their right-hand end, as depicted in figure (5.36). An analysis of the transverse electric

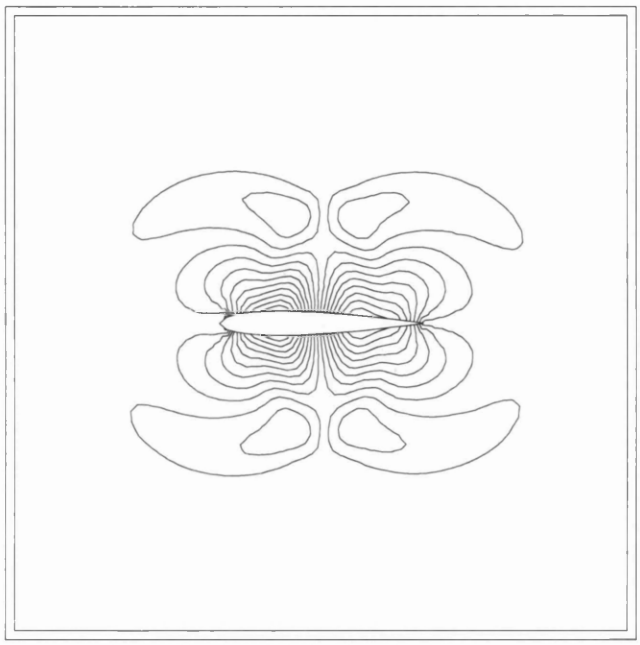

Figure 5.29: Scattering by a NACA0012 aerofoil of electrical length 2λ: E_y contours

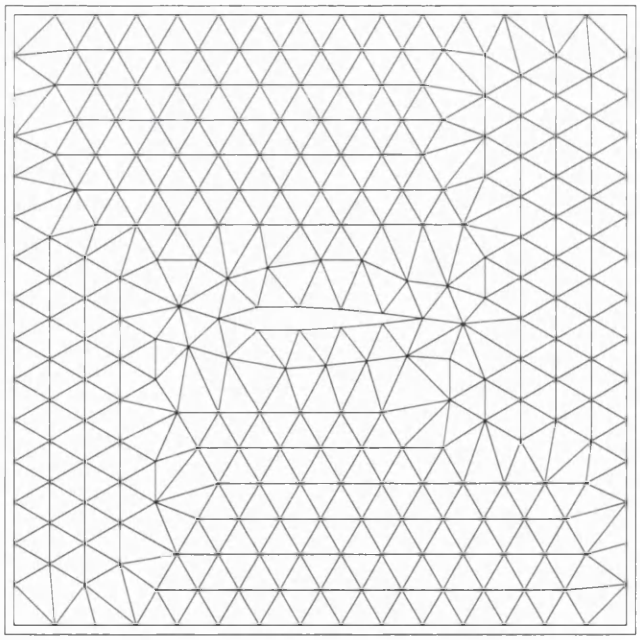

Figure 5.30: Scattering by a NACA aerofoil of electrical length 1λ: the mesh consists of 472 elements

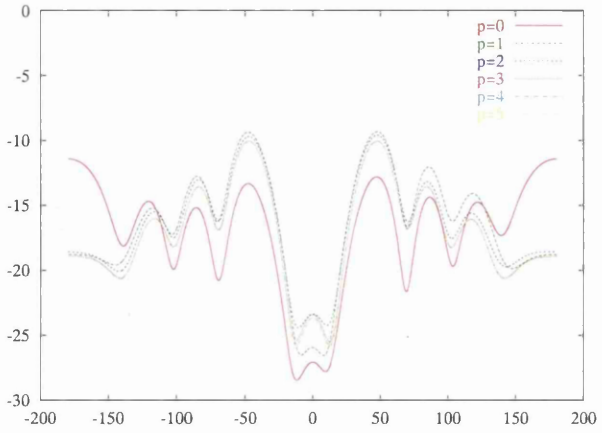

Figure 5.31: Scattering by a NACA aerofoil of electrical length 1λ: RCS distributions when aerofoil is illuminated from the front.

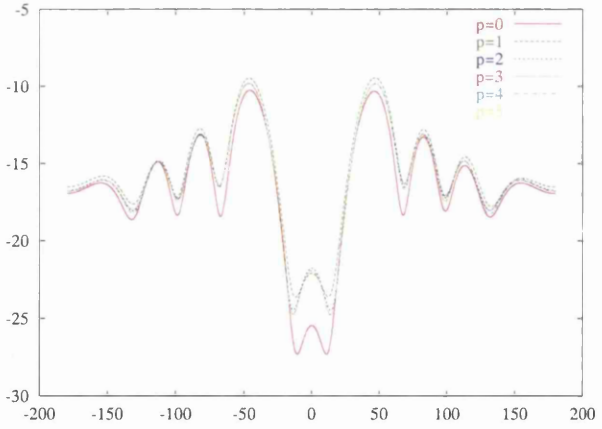

Figure 5.32: Scattering by a NACA0012 aerofoil of electrical length 2λ: RCS distributions when aerofoil is illuminated from the front.

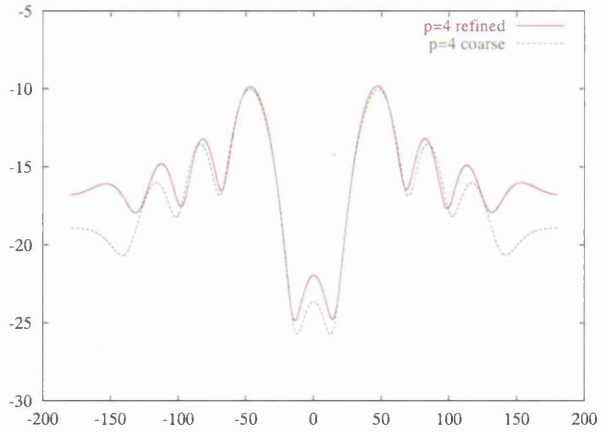

Figure 5.33: Scattering by NACA aerofoils: comparison between the converged RCS distributions of the NACA aerofoils, from the front

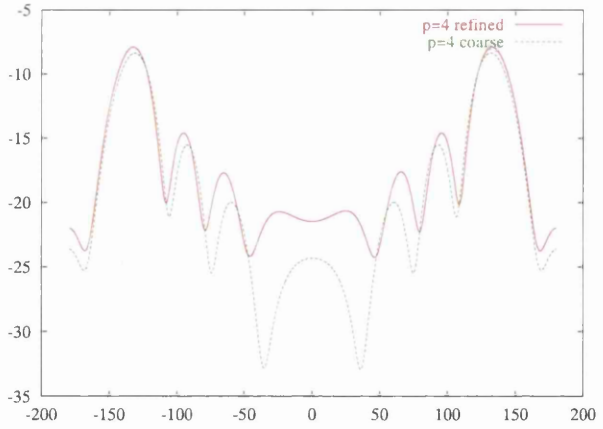

Figure 5.34: Scattering by NACA aerofoils: comparison between the converged RCS distributions of the NACA aerofoils, from the rear

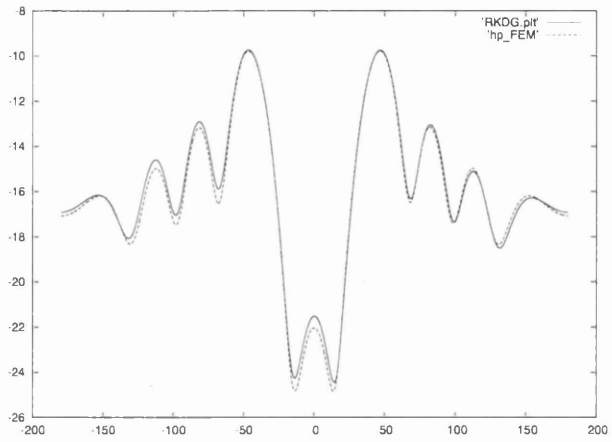

Figure 5.35: Scattering by NACA0012 aerofoils: comparison between the converged RCS distributions of the RKDG scheme and a hp-FEM scheme, from the rear

RCS distribution is to be performed. The incident wave propagates along the $x-$axis. The mesh itself is an unstructured grid which is comprised of 377 triangles.

Following standard procedure, the order of the approximation is increased until convergence of the RCS distribution is achieved. It can be seen, from figure (5.37), that an order four and five approximation provide very similar distributions, and due to the computational cost, here an order $p = 4$ approximation suffices.

Figure (5.38) proves that a converged numerical distribution is achieved when an order $p = 5$ approximation is used, as an order $p = 5$ and order $p = 6$ approximation provide identical distributions. Recalling that the computational cost of attaining an order five approximation greatly exceeds that of an order four approximation, it makes computational sense that the analysis should remain at an order four approximation.

Figure (5.38) proves that a numerical convergence is achieved for this example.

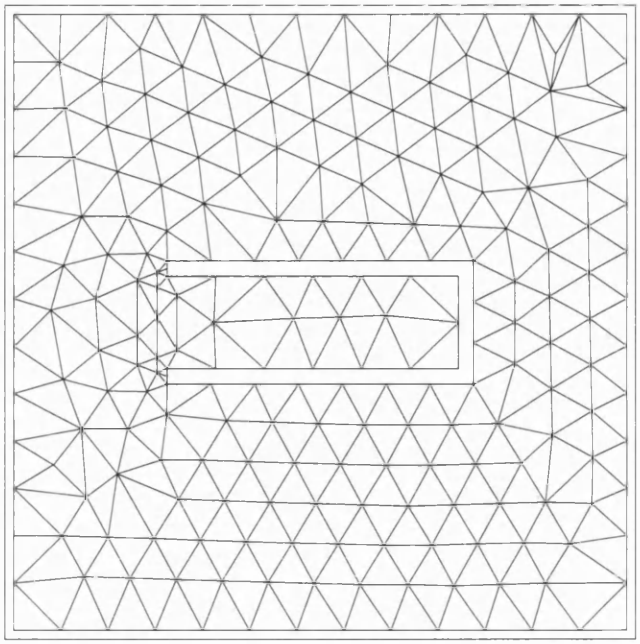

Figure 5.36: Scattering by a semi-open cavity: the mesh consisting of 377 triangles.

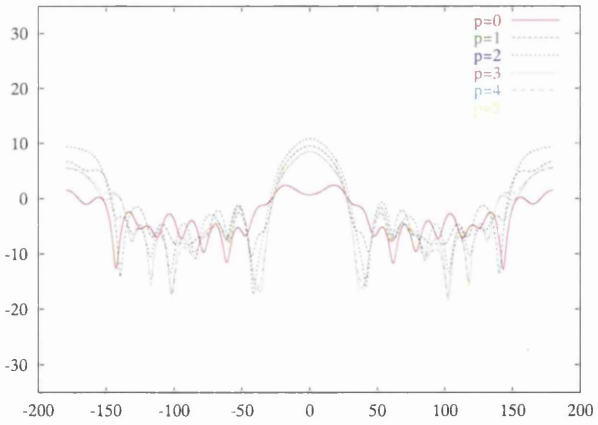

Figure 5.37: Scattering by a semi-open cavity: convergence of the RCS for an incident wave propagated along the x-axis.

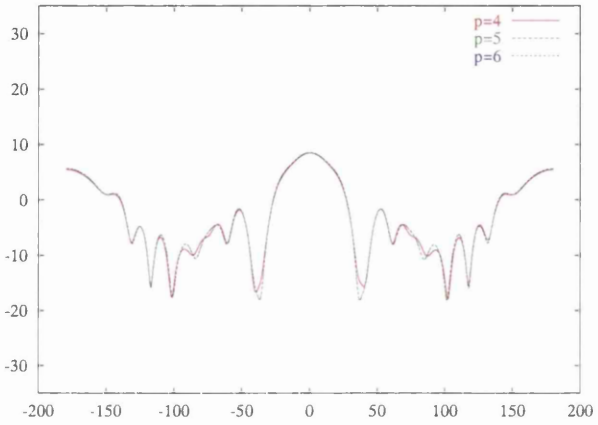

Figure 5.38: Scattering by a semi-open cavity: convergence of the numerical solution for an incident wave propagated along the x-axis.

Chapter 6

Perfectly Matched Layers and Blending Functions

6.1 Introduction to chapter

This chapter is mainly concerned with an alternative approach to the far field boundary condition that was implemented in Chapter Five. This alternative approach yields an increase in the accuracy of the numerical solution, but at a computational cost. The theory regarding this far field boundary formulation will be discussed shortly. The mathematical description of the far field boundary, as it appears in implementation, is then presented.

As expected, the accurate representation of an infinite domain has received much attention in the past. Characteristic boundary conditions were earlier employed to represent the far field boundary. This method, however, is limited in application for the specified reasons. More elaborate far field schemes consist of, for example, radiation boundary conditions or an asymptotic expansion of the far-field solution. Another type of method, that attacks the problem from a different angle, is the buffer or sponge layer procedure, a far field representation of this type involves outgoing waves being damped and decelerated or accelerated to supersonic speeds [78].

In the context of solving Maxwell's equations in the time-domain, Berenger proposed a novel way to derive the desired absorbing boundary conditions. Berenger suggested that an unphysical splitting of Maxwell's equations would introduce, beneficial, additional degrees of freedom which would allow for layer construction. The layers could then maintain absorbtion properties, irrespective of the angle of propagation. The layers are defined in such a way that any waves entering the layers are completely absorbed (without reflections). These layers have been termed perfectly matched layers (PMLs).

While the imposition of PMLs has been wide spread, the initial method is by no means free

of problems. It was relatively recently proven that the unphysical splitting of Maxwell's equations results in a set of equations that are only weakly well-posed and therefore result in unstable schemes [81, 78]. This discovery has focused the attention towards other, alternative, well-posed formulations of the electromagnetic PML. Naturally the alternate approaches involve unsplit PML methods. At the time of writting, there currently exists two types of unsplit PML methods, the first relies upon mathematical arguments whilst the second involves a physical reasoning [82].

Regardless of the original, erroneous, approach [81], the PML method has proven extremely beneficial for wave-like problems. The development of efficient, robust and accurate methods with which to truncate the computational domain is becoming ever more important, especially for high-order methods. As High-order methods produce an improved interior solution, it would be counter-productive if they were hampered by artificial reflections.

The chapter concludes with a discussion on how to model curved elements. Real life simulation often entails the modelling of a curved boundary. The curvature of the elements is achieved via blending functions. The blending functions are to be stated and the results obtained are then presented and discussed.

6.1.1 Constructing the PML

As is known, the problem presented by a typical scattering problem involves an infinite domain. The accurate representation of this infinite domain is of great importance. The technique to be presented here absorbs the outgoing waves, therefore yielding an accurate model, with no reflection. Theoretically imposing a PML boundary entails a computational domain that is surrounded by a rectangle, which itself is formed from a structured mesh of triangles. Within the PML the z-component of the electromagnetic field is split into component parts. The rectangular shape of the truncated far field boundary is constant, and the minimum distance from the scatterer is $\frac{3}{2}\lambda$. The thickness of the PML is given by λ. The system is stable if the CFL numbers provided in [83] are satisfied. The mathematical theory to obtain a solution within the PML medium is subsequently described.

6.1.2 Mathematical detail for the PML

Original formulation

In accordance with Berenger [84], the Maxwell equations in an absorbing layer can be written as

$$\frac{\partial \boldsymbol{E}}{\partial t} - curl\boldsymbol{E} + \sigma \boldsymbol{E} = 0 \tag{6.1}$$

$$\frac{\partial \boldsymbol{H}}{\partial t} + curl\boldsymbol{E} + \sigma^* \boldsymbol{H} = 0 \tag{6.2}$$

where σ and σ^* are the electric and magnetic conductivity respectively. Traditionally the layers that absorb the outgoing waves satisfy the condition

$$\sigma = \sigma^* \tag{6.3}$$

The above formulation has since been improved upon, and this improvement is discussed below. Berenger proposed a novel technique in which the theoretical reflection factor of a plane wave striking a vacuum-layer interface is zero at any frequency and at any angle of incidence. Assuming TM polarisation, the Maxwell equation set in a PML medium is obtained by introducing a new degree of freedom. The component E_z is split into the component parts of E_{zx} and E_{zy} resulting in an electromagnetic field of $(H_x, H_y, E_{zx}, E_{zy})$. There now exists four unknown components to the EM field. When the scattered field enters the PML medium the waves are governed by the following equation set

$$\frac{\partial H_x}{\partial t} + \frac{\partial (E_{zx} + E_{zy})}{\partial y} + \sigma_y H_x = 0 \tag{6.4}$$

$$\frac{\partial H_y}{\partial t} - \frac{\partial (E_{zx} + E_{zy})}{\partial x} + \sigma_x H_y = 0 \tag{6.5}$$

$$\frac{\partial E_{zx}}{\partial t} - \frac{\partial H_y}{\partial x} + \sigma_x E_{zx} = 0 \tag{6.6}$$

$$\frac{\partial E_{zy}}{\partial t} + \frac{\partial H_x}{\partial y} + \sigma_y E_{zy} = 0 \tag{6.7}$$

Investigating this set of equations led Berenger to deduce that the choice of σ_x and σ_y[1] is extremely important. The values σ_x and σ_y can be considered as the absorption coefficients in their respective direction (discussed subsequently). A similar procedure is adopted for the TE case, here H_z is split into component parts and the desired unknowns are $(E_x, E_y, H_{zx}, H_{zy})$.

6.1.3 The absorption coefficient

The absorption coefficient, σ, for the relevant direction, x or y, is defined as

[1]Note the fact that if $\sigma_x = \sigma_y$ then the Maxwell equations in a classical absorbing layer are achieved

$$\sigma_x = \frac{18dist_x^3}{\lambda^4} \quad \sigma_y = \frac{18dist_y^3}{\lambda^4} \tag{6.8}$$

where $dist_{x/y}$ represents the distance from the far field boundary to a point in the PML, in the relevant direction. For the propagation of the electromagnetic wave in free space σ_x and σ_y are zero.

6.1.4 A new idea

Following the work outlined in [6], we discuss where the scheme employed in this thesis differs from Berenger's. A simplification of the equation set (6.4-6.7) is possible. The simplification arises on the assumption that the component E_{zx} can be rewritten as

$$E_{zx} = E_z - E_{zy} \tag{6.9}$$

substituting this expression into the equation set (6.4-6.7) yields, for this thesis, the equations that are required to be solved for a numerical solution in a PML.

$$\frac{\partial H_x}{\partial t} + \frac{\partial E_z}{\partial y} + \sigma_y E_x = 0 \tag{6.10}$$

$$\frac{\partial H_y}{\partial t} - \frac{\partial E_z}{\partial y} + \sigma_x H_y = 0 \tag{6.11}$$

$$\frac{\partial E_z}{\partial t} + \frac{\partial H_x}{\partial x} - \frac{\partial H_y}{\partial y} + \sigma_x E_z + E_{zy}(\sigma_y - \sigma_x) = 0 \tag{6.12}$$

$$\frac{\partial E_{zy}}{\partial t} + \frac{\partial H_x}{\partial y} + \sigma_y E_{zy} = 0 \tag{6.13}$$

This set of equations provide the framework the for the perfectly matched layer boundary condition enforced in this thesis. The above equation set is easily derived from the previous equation set (6.4-6.7) by substituting equation (6.9) where relevant. The first three equations are Maxwell's equations, in free space, with a source term. Thus the first three equations are solved as previously specified, the final equation, however, requires a appropriate numerical approximation.

This equation set, for Maxwell's equations in the PML medium, differs from the set obtained in Berenger's PML because Berenger split, for the two-dimensional TM case, the component E_z into two sub-components, E_{zx} and E_{zy}, giving

$$E_z = E_{zx} + E_{zy} \tag{6.14}$$

and

$$H_z = H_{zx} + H_{zy} \tag{6.15}$$

for the TE case. Therefore by employing equation (6.9) we get a different formulation, where as previously stated, only the final equation (6.13) requires a numerical approximation.

6.1.5 Mathematical detail

For a numerical solution in a PML medium, the system of equations may be written, in conservation form, as

$$\frac{\partial \boldsymbol{U}}{\partial t} + \frac{\partial \boldsymbol{F}(\boldsymbol{U})}{\partial x} + \frac{\partial \boldsymbol{G}(\boldsymbol{U})}{\partial y} + \Sigma(\boldsymbol{U}) = 0 \tag{6.16}$$

where, for the TM case

$$\boldsymbol{U} = (U_1, U_2, U_3, U_4) = (H_x, H_y, E_z, E_{zy}) \tag{6.17}$$

$$F(\boldsymbol{U}) = (0, -E_z, -H_y, 0) \qquad G(\boldsymbol{U}) = (E_z, 0, H_x, H_x) \tag{6.18}$$

$$\Sigma(\boldsymbol{U}) = (\sigma_y H_x, \sigma_x H_y, \sigma_x E_z + (\sigma_y - \sigma_x) E_{zy}, \sigma_y E_{zy}) \tag{6.19}$$

and for the TE case

$$\boldsymbol{U} = (U_1, U_2, U_3, U_4) = (E_x, E_y, H_z, H_{zy}) \tag{6.20}$$

$$F(\boldsymbol{U}) = (0, -H_z, -E_y, 0) \qquad G(\boldsymbol{U}) = (H_z, 0, E_x, E_x) \tag{6.21}$$

$$\Sigma(\boldsymbol{U}) = (\sigma_y E_x, \sigma_x E_y, \sigma_x H_z + (\sigma_y - \sigma_x) H_{zy}, \sigma_y H_{zy}) \tag{6.22}$$

As detailed in Chapter Two, a unified formulation provides a better platform from which to form the variational statement. The equation set in conservation form becomes

$$\frac{\partial \boldsymbol{U}}{\partial t} + \nabla \mathbb{F}(\boldsymbol{U}) + \Sigma(\boldsymbol{U}) = 0 \tag{6.23}$$

where $\mathbb{F} = (\boldsymbol{F}(\boldsymbol{U}), \boldsymbol{G}(\boldsymbol{U}))$. Adhering to the discontinuous Galerkin method, the variational formulation is

$$\frac{\partial}{\partial t}\int_e \boldsymbol{U} W d\Omega = \int_e \sum_{j=1}^{2} \frac{\partial W}{\partial x_j}\mathbb{F}(\boldsymbol{U})^j d\Omega - \int_{\Gamma_e} \mathbb{F}^n(\boldsymbol{U}) W d\Gamma - \int_e \Sigma(\boldsymbol{U}) W d\Omega \tag{6.24}$$

Investigation of equation (6.24) reveals that the PML variational statement differs to the variational statement in Chapter Five by the appearance of the integral of a sum over the element [6].

6.2 The area integral

The final term on the RHS of equation (6.24) can be considered as an area integral. This integral is evaluated in manner similar to that of the mass matrix.

$$\int_e \Sigma(\boldsymbol{U}) W d\Omega = \sum_{n=1}^{nip}\sum_{m=1}^{nip} \Sigma(\boldsymbol{U}) W |\boldsymbol{J}||\tilde{\boldsymbol{J}}| W_n W_m \tag{6.25}$$

Care is needed to ensure that the element under consideration is contained in the PML medium.

6.3 The nature of the PML equations

The Maxwell equations are a hyperbolic system of equations and this factor infers that upwind type schemes be employed for the approximate solution [6]. Unfortunately, Maxwell's equation in a PML medium do not represent a hyperbolic system, but de la Bourdonnaye [85] proved that incorporating the divergence and a compatibility equations yielded a system that is hyperbolic in the medium, resulting in a well posed problem [6].

6.3.1 Numerical flux of the fourth equation

In free space, the TE components E_x, E_y and H_z, of $\boldsymbol{U}$, are found as previously stated, the remaining component H_{zy} is not required in free space. At the interface between the free space and the PML medium, H_{zy} needs to be evaluated, and is dependent upon E_x, E_y and H_z and found via Rankine-Hugoniot jump conditions.

Numerical flux in the PML

The formulation that is now presented follows closely that outlined in the text of F. Bonnet and F. Poupaud [6].

The Rankine-Hugoniot jump relations are employed to calculate the numerical flux. From equation (5.32) the Jacobian matrix $\boldsymbol{A}$, for the PML formulation, is given by

$$\boldsymbol{A} = \begin{pmatrix} 0 & 0 & 0 & n_x \\ 0 & 0 & -n_y & 0 \\ n_y & n_y & 0 & 0 \\ -n_x & 0 & 0 & 0 \end{pmatrix} \tag{6.26}$$

Employing the characteristic equation, $|\lambda I - \boldsymbol{A}| = 0$, it follows

$$\Longrightarrow \qquad \lambda[\lambda(\lambda^2) - n_x(n_x\lambda)] - n_y[-n_y(-n_y\lambda)] = 0 \tag{6.27}$$

the eigenvalues are thus

$$\lambda = \pm 0, \quad \lambda = \pm 1 \tag{6.28}$$

It follows from the Rankine-Hugonoit condition that:- For$\underline{\lambda = 0}$

$$\boldsymbol{n} \wedge (\boldsymbol{E}^{**} - \boldsymbol{E}^{*}) = 0 \qquad \boldsymbol{n} \wedge (\boldsymbol{H}^{**} - \boldsymbol{H}^{*}) = 0 \tag{6.29}$$

For $\underline{\lambda = -1}$

$$\boldsymbol{n} \wedge (\boldsymbol{E}^{*} - \boldsymbol{E}^{L}) = -\boldsymbol{n} \wedge \boldsymbol{n} \wedge (\boldsymbol{H}^{*} - \boldsymbol{H}^{L}) \qquad \boldsymbol{n} \wedge (\boldsymbol{H}^{*} - \boldsymbol{H}^{L}) = -\boldsymbol{n} \wedge \boldsymbol{n} \wedge (\boldsymbol{E}^{*} - \boldsymbol{E}^{L}) \tag{6.30}$$

For $\underline{\lambda = 1}$

$$\boldsymbol{n} \wedge (\boldsymbol{E}^{R} - \boldsymbol{E}^{**}) = \boldsymbol{n} \wedge \boldsymbol{n} \wedge (\boldsymbol{H}^{R} - \boldsymbol{H}^{**}) \qquad \boldsymbol{n} \wedge (\boldsymbol{H}^{R} - \boldsymbol{H}^{**}) = -\boldsymbol{n} \wedge \boldsymbol{n} \wedge (\boldsymbol{E}^{R} - \boldsymbol{E}^{**}) \tag{6.31}$$

The approximation of the fourth numerical flux can now be presented. Let ϕ be the approximate flux required, then, for the TM case

$$\phi = H_x^* n_y \tag{6.32}$$

Clearly the flux is determined by the value of H_x^*. This value is found with the use of the Rankine-Hugonoit jump relations and transforming, via an appropriate change of variables (X, Y) in the respective normal and tangential directions, the bi-dimensional Riemann problem into a one-dimensional Riemann problem [86], consider

$$\frac{\partial \tilde{\boldsymbol{U}}}{\partial t} + \frac{\partial \boldsymbol{F}(\tilde{\boldsymbol{U}})}{\partial X} = 0 \tag{6.33}$$

where now $\tilde{\boldsymbol{U}} = (H_X, H_Y, E_z)$ and $F(\tilde{\boldsymbol{U}}) = (0, -E_z, -H_Y)$. The expression

$$H_y = \frac{1}{2}(H_Y^L + H_Y^R) + \frac{1}{2}(E_z^R - E_z^L) \tag{6.34}$$

is achieved directly from the Rankine-Hugoniot equations. Then since

$$H_x = n_x H_X - n_y H_Y \tag{6.35}$$

it must follow that

$$H_x^* = n_x H_X^* - n_y H_Y^* \tag{6.36}$$

with

$$H_X^* = \frac{1}{2}(H_X^L - H_X^R) \tag{6.37}$$

Therefore

$$H_x^* = \frac{1}{2}(H_x^L + H_x^R) - \frac{1}{2}(E_z^R - E_z^L) \tag{6.38}$$

The numerical flux, in the terms of the original variables (x, y), can then be written as

$$\phi = \frac{1}{2}(H_x^L + H_x^R) n_y - \frac{1}{2}(E_z^R - E^L) n_y^2 \tag{6.39}$$

and this is incorporated in the fourth equation that for the TM case.

6.3.2 Boundary conditions

The boundary condition at the outer surface of the PML medium is that of a PEC. A PEC condition is enforced for the reason that if any wave exists after going through the PML medium then it is reflected off the PEC and further absorbed. The perfectly conducting condition is detailed in Chapter Two and for the TM case

$$E_z = 0 \tag{6.40}$$

while for the TE case

$$n_x E_y - n_y E_x = 0 \tag{6.41}$$

The PML medium need not conclude with a PEC condition, other choices exist. As expected the other options offer the traditional advantages and disadvantages of efficiency etc. One possibility is to end the PML medium with an absorbing boundary condition. These considerations are possibilities for further research.

PEC conclusion of solution domain

If the Rankine-Hugoniot conditions are employed, along with the PEC condition, equation (6.40), the TM boundary flux that concludes the PML domain becomes

$$\int_{Fe} \mathbb{F}(\boldsymbol{U}) W d\Gamma = \int_e \begin{pmatrix} 0 \\ 0 \\ n_y H_x - n_x H_y \\ n_y H_x \end{pmatrix} W d\Gamma \tag{6.42}$$

and for transverse electric polarisation, with use of equation (6.41), we obtain

$$\int_{Fe} \mathbb{F}(\boldsymbol{U}) W d\Gamma = \int_e \begin{pmatrix} n_y H_z \\ -n_x H_z \\ 0 \\ n_y E_x \end{pmatrix} W d\Gamma \tag{6.43}$$

This concludes the treatment for the PML medium.

6.4 Blending Functions

The blending functions for triangular elements are now presented. Blending methods typically involve adding extra points on the boundaries of the elements and thereby allow for a better representation of the geometry, for this thesis the edges on a curved boundary are completely represented. When an unstructured mesh is employed the blending function method reduces to the linear approximation for elements with straight sides.

Due to the addition of the PML, the blending functions are only applied to the elements that comprise the boundary of the scatterer, and only PEC cylinders are considered. The blending functions are given by

$$\begin{bmatrix} x \\ y \end{bmatrix} = \sum_{i=1}^{3} \upsilon_i \begin{bmatrix} x_i \\ y_i \end{bmatrix} + \upsilon_1\upsilon_2 \begin{bmatrix} g_1^x(\upsilon_3 - \upsilon_2, x_1, x_2) \\ g_1^y(\upsilon_3 - \upsilon_2, y_1, y_2) \end{bmatrix} + \tag{6.44}$$

$$\upsilon_2\upsilon_3 \begin{bmatrix} g_2^x(\upsilon_3 - \upsilon_2, x_2, x_3) \\ g_2^y(\upsilon_3 - \upsilon_2, y_2, y_3) \end{bmatrix} + \upsilon_3\upsilon_1 \begin{bmatrix} g_3^x(\upsilon_1 - \upsilon_3, y_3, y_1) \\ g_3^y(\upsilon_1 - \upsilon_3, y_3, y_1) \end{bmatrix} \tag{6.45}$$

Here the expression

$$g_i^x(\tau, x_j, x_k) = \frac{4}{1-\tau^2} \left[\tilde{g}_3^x(\tau) - \tfrac{1-\tau}{2} x_j - \tfrac{1+\tau}{2} x_k \right] \tag{6.46}$$

and

$$g_i^y(\tau, y_j, y_k) = \frac{4}{1-\tau^2} \left[\tilde{g}_3^y(\tau) - \tfrac{1-\tau}{2} y_j - \tfrac{1+\tau}{2} y_k \right] \tag{6.47}$$

define the difference between the true edge and the approximation when straight sides are assumed. The exact shape of the edge, determined by $\tilde{g}_i^x(\upsilon)$ and $\tilde{g}_i^y(\upsilon)$, is defined in terms of a non-dimensional parameter υ which varies from -1 to 1 from vertex j to k.

6.5 Results

The perfectly matched layers consist of a structured mesh. This mesh surrounds the unstructured mesh, as depicted in figure (6.1). The thickness of the PML is choosen to be between 2λ and 3λ. A

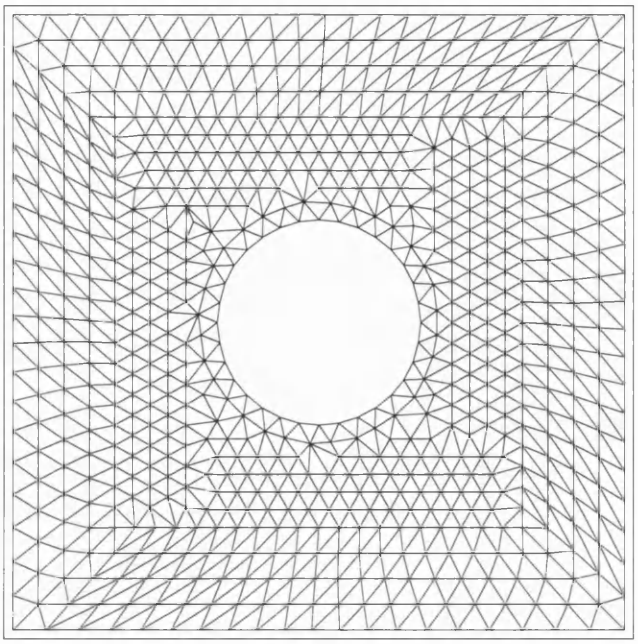

Figure 6.1: Scattering by a circular cylinder of electrical length 2λ: an unstructured mesh of 682 elements

mesh consisting of 158 unstructured elements is also employed (not including elements in the PML).

The results presented here consist of the analysis performed upon the perfect electrically conducting cylinders, encountered in the previous chapter. Again, the electrical length of the cylinder is 2λ, unless otherwise stated. The scattering width distributions are then presented, with relevant comparisons, to the initial characteristic far field condition, presented in the previous chapter, made.

The figure (6.2) provides the contours of the y-component of the electric field, the contours are not so well defined in the PML medium due to a less fine mesh being employed. Figure (6.3) highlights the discrepancies between the results achieved from the previous chapter and the RCS distribution when a PML condition is enforced. The figure (6.4) shows that the converged RCS distribution, with the PMLs applied, on the 682 element mesh is now indistinguishable from the exact solution, unlike the results achieved from the previous chapter. The RCS distribution depicted in figure (6.5) shows that, for a larger electrical length, the RCS distribution is all but identical to the exact solution.

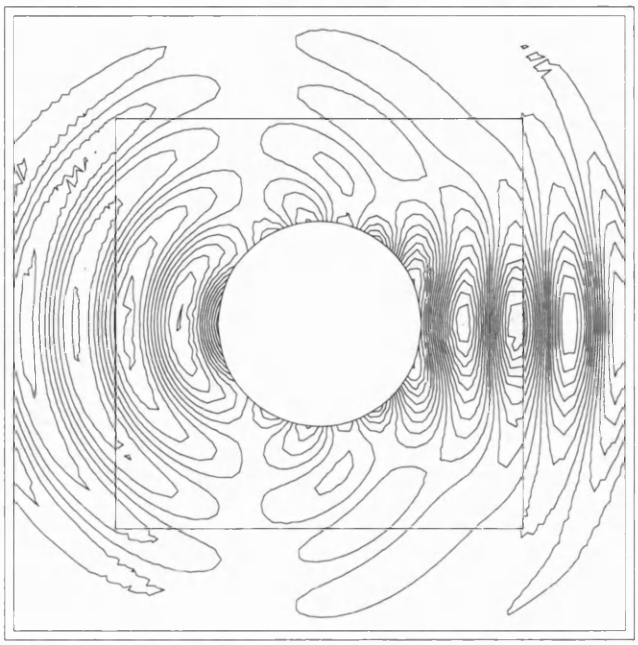

Figure 6.2: Scattering by a circular cylinder of electrical length 2λ: the contours of E_y

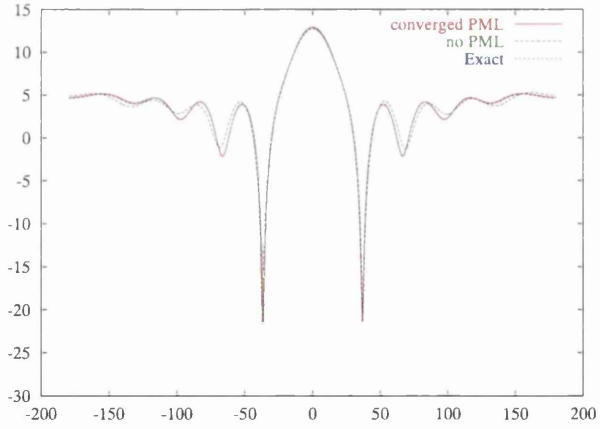

Figure 6.3: Scattering by a 682 element circular cylinder of electrical length 2λ: the comparison between the converged PML boundary condition, the converged characteristic boundary condition and the exact solution, for $p = 4$

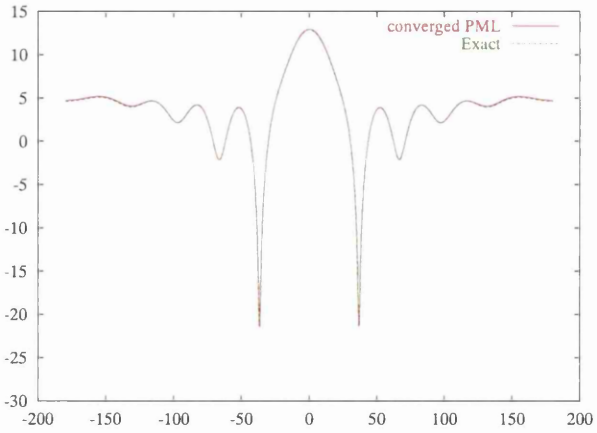

Figure 6.4: Scattering by a 682 element circular cylinder of electrical length 2λ: comparison between the converged numerical solution and the exact solution, obtained from a PML boundary condition, for $p = 4$

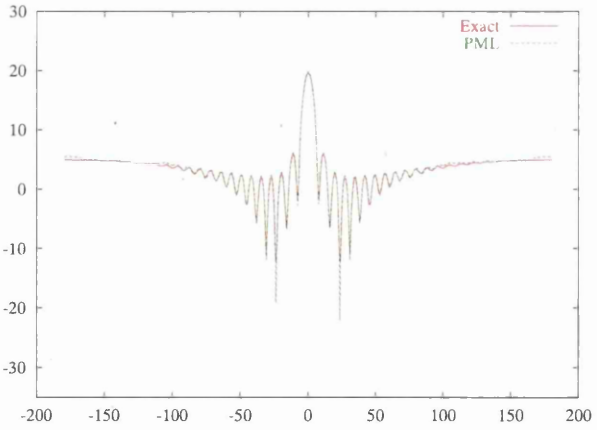

Figure 6.5: Scattering by a 158 element circular cylinder of electrical length 10λ: comparison between the converged numerical solution and the exact solution, obtained from a PML boundary condition, for $p = 4$

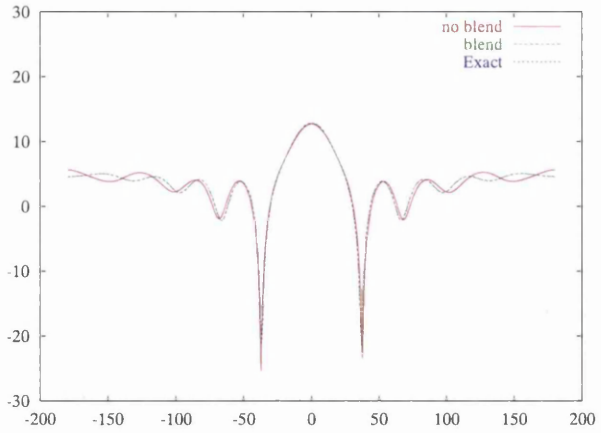

Figure 6.6: Scattering by a circular cylinder of electrical length 2λ, on the 682 element mesh: the comparison between a linear and blended approximation, for differing approximations

6.5.1 Results achieved from blending techniques

The final examples, presented in this thesis, involve an improvement in computational domain representation. Blending techniques provide an increase in the capability of accurately representing the domain. The figures (6.6) and (6.7) provide a comparison between a linear geometry approximation and the numerical solution achieved from the blending techniques. The comparisons provided entail the relevant converged TE RCS distributions.

It can be gathered from the results that an increase in the domain representation provides a much higher quality of solution. Figure (6.6) shows a quadratic approximation, with blending applied, plotted against an order four approximation, the quadratic yields the more accurate approximation.

Figure (6.8) shows that for the converged RCS distribution, a solution is achieved that is identical to the exact solution for the blending example, whilst the linear result is incorrect.

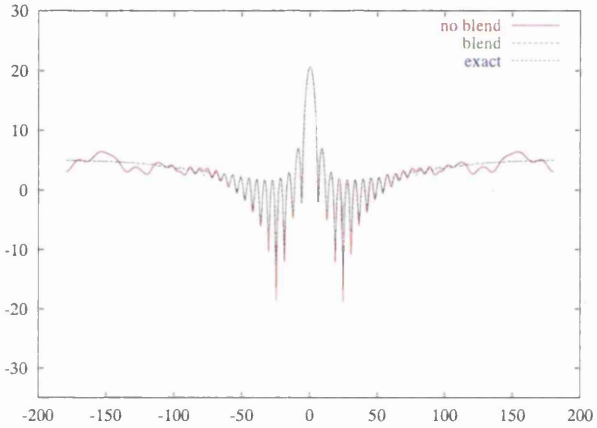

Figure 6.7: Scattering by a circular cylinder of electrical length 10λ on the 158 element mesh: the comparison between the converged RCS distributions, for both a linear and blended approximation

Chapter 7

Conclusion and further work

7.1 Introduction to chapter

This thesis has discussed the formulation and verification of a fully unstructured, high-order, accurate scheme suitable for time-domain approximate solutions of Maxwell's equations. The majority of the discussion has focused upon a precise formulation of the scheme with regards to computational electromagnetics. The scheme under consideration was the fourth order Runge-Kutta discontinuous Galerkin finite element method. It was the aim to present a description and analysis of this method so that efficient and accurate numerical solution to Maxwell's equations could be found. The work produced by Warburton, Hesthaven Shu, and Karnadiakis [55, 4, 73, 44, 45, 46, 55] amongst others, was of invaluable benefit and the theory detailed in Chapters Four, and Five relied upon their achievements.

The results achieved, in relation to the cost at which they were obtained, suggest that the Runge-Kutta discontinuous Galerkin method appears a most promising numerical method, even providing numerical solutions where the one-dimensional Taylor-Galerkin scheme could not.

To follow some brief detail on the results achieved and then a short description on some further analysis that could be performed as either an extension or a variation of this work.

7.1.1 Discussion concerning Chapter Four

It has been shown, toward the end of Chapter Four, that a RKDG comparison with a Taylor-Galerkin scheme proved most favourable. Indeed the RKDG method is capable of providing acceptable numerical solutions where the TG scheme is not. The one-dimensional problem also served to provide a collection of CFL numbers, for various orders of approximation. These CFL numbers can be referred to when requiring solutions to problems that require a particular order of approximation. The

error analysis also means that a numerical solution, for certain order numerical approximations upon selected elemental lengths, can be supplied that can meet pre-requisites of acceptable error.

Chapter four also showed, for the examples analysed, that employing an approximation higher than $p = 4$ is unnecessary. The results obtained from an order five polynomial are nearly indistinguishable from an order four approximation, but the cost of employing an order five polynomial greatly exceeds that of an order four representation. This finding was also partially evident from the results achieved in Chapter Five (not so for the large electrical lengths). The table below highlights the minimum number of elements required to provide a numerical solution that was comparable with the exact solution

Order	Element per λ
1	20
2	5
3	4
4	2
5	2

Note that the same number of elements is required for an order 4 polynomial as that for an order 5 polynomial.

Chapter Four also provided an analysis between the benefits of h-type refinement and p-type refinement. It was shown that considerably less unknowns were required for p-refinement strategies, whereas the same amount of unknowns was required for a $p = 0$ approximation upon the final h-refinement mesh and still no convergence was achieved. Hence it is clearly better to increase the polynomial order as opposed to refining the mesh, this was further endorsed for the two-dimensional case.

Finally the Taylor-Galerkin comparison serves to prove, that the RKDG method will provide more acceptable approximations when a high-order of accuracy is required. The Taylor-Galerkin scheme was unable to provide acceptable solutions when five elements per wavelength were required, conversely the RKDG method still provides accurate solutions, albeit at an increase in computational cost, when only two elements per wavelength are permitted.

7.1.2 Discussion concerning Chapter Five

In chapter Five we saw the analysis and verification of the two-dimensional RKDG method for the numerical solution of Maxwell's equations. Chapter five employed a basis due to Dubiner [63]. The results, primarily the RCS distributions, obtained whilst investigating the PEC annulus were plotted

and verified. The scheme was validated by comparing the scattering widths to known analytical solutions. The scheme was then employed to consider scatterers which have no analytical solutions. For all of these examples it was shown that, upon a constant mesh, in accordance with the one-dimensional case, increasing, uniformly, the order of approximation led to convergence of the solution.

A similar refinement analysis to the one-dimensional case was also performed in this chapter. The analysis involved a comparison, upon unstructured meshes consisting of 2508 elements, 682 elements and 158 elements[1]. As expected, the results obtained proved favourable for p-type analysis.

It was also seen that for the problems involving a large electrical length that a higher-order of approximation was required.

7.1.3 Discussion concerning Chapter Six

The previous chapter saw the RKDG theory extended to include perfectly matched layers and, via blending functions, a superiour representation of the circular annulus. The blending technique provided an increase in the accuracy of the geometry representation, and, as a result the correct representation of the scatterer is maintained and a true converged solution is achieved.

The results acquired are as expected, blending techniques provide an increase in the accuracy of the solution, allied to an increase in efficiency. The larger electrical length with no blending shows that approximating the boundary to a high standard is important. It is therefore evident that improving the geometry representation provides for an improved numerical solution.

The analysis for the perfectly matched layer technique again produced the expected improvement in accuracy. The technique can be expensive due to the increase in the number of unknowns, but it was shown that the PML provides excellent solutions.

7.2 Future work

7.2.1 Additions to the scheme presented

There still exists a great amount of analysis that could be performed for RKDG schemes. To emphasise a natural extension of the scheme presented in the previous chapters, would see an extension to three spatial dimensions. In three dimensions the theory would remain similar, a three dimensional basis proposed by Dubiner, whose implementation naturally follows on from the two-dimensional basis, could be readily applied. Clearly the boundaries of the elements would consist of tetrahedral faces and the area integrals would become volume integrals, other such considerations would materialise.

[1] Partially as a result of the inability to generate unstructured meshes that exactly provide a factor of 4 and 16 refinement

An interesting variation to the scheme presented would see the perfectly electrical boundary, that concludes the perfectly matched layer medium, replaced by an absorbing boundary condition. This new formulation would be especially important for problems with a large electrical length. [2]

7.3 Other aspects that could be investigated

7.3.1 Quadrature-free formulation

In chapter Three, section 3.8.2, quadrature-free discontinuous Galerkin methods were briefly discussed. An investigation of recent literature suggests that this method appears highly promising. The work of Atkins and Shu, during 1998 [29], provided the initial analysis of quadrature-free RKDG methods. The basic premise of the scheme is to employ a local basis that can be easily manipulated. The basis can be comprised of the the Taylor expansions. The integration of the product of polynomials, in this local basis, can be pre-determined and therefore stored. A similarity transformation allows the data for only one reference element to be stored. This type of formulation results in simpler coding and a significant increase in the speed of computation [26].

7.3.2 Differing time steps

In the event *hp*-refinement is to be performed, for a given region of the computational domain, then the time steps employed should vary, different time steps are required for different order approximations and different size elements, in order to maintain the benefits of adaptivity and parallelisability. Incorporating this idea into a numerical scheme would involve identifying the order of approximation in a particular element and then using the most efficient time increment. A similar procedure would be required for identifying the elemental length of each element and then applying the the relevant time step.

Enforcing this condition however is expensive in terms of the efficiency and in the programming, it would however be of interest to see the outcome of such an analysis.

7.3.3 Modal over nodal

Finally this thesis employed a modal basis but there does exist another option. A nodal basis as described in [87] is such an alternative, here the identification of a nodal set suitable for high-order

[2] For large electrical lengths the PML approach close to the scatterer can produce small oscillations but the PML/ABC exhibits now additional oscillations. Therefore a comparison between the two procedures would be interesting.

representation upon unstructured grids is provided. A comparison between the two possible bases would be interesting.

Bibliography

[1] L. Pierce Williams. *Michael Faraday: A Biography*. Da Capo Press, 1987.

[2] Arindam Chatterjee John L. Volakis and Leo C. Kempel. *Finite Element Method for Electromagnetics*. IEEE, 1998.

[3] K. S. Yee. Numerical solution of the initial boundary value problems in isotropic media. *IEEE transactions on atennas and propagation*, 14:302–307, 1966.

[4] S. J. Sherwin and G. E. Karniadakis. A triangular spectral element method; applications to the incompressible Navier-Stokes equations. *Computer Methods in Applied Mechanics and Engineering*, 123:189–229, 1995.

[5] D. W. Halt and R. K. Agarwal. A compact Higher Order Characteristic-Based Euler Solver for Unstructured Grids. 1991. AIAA 29th Applied Aerodynamics Conference, AIAA 91-3234.

[6] F. Bonnet and F. Poupaud. Berenger absorbing boundary condition with time finite-volume scheme for triangular meshes. *Applied numerical mathematics*, 25:333–354, 1997.

[7] O. Hassan K. Morgan and J. Peraire. A time domain unstructured grid approach to the simulation of electromagnetic scattering in piecewise bhomogeneous media. *Compt. Methods Appl. Mech. Engrg*, 134:17–36, 1996.

[8] B. Enguist and A. Majda. Absourbing Boundary Conditions for the Numerical Simulation of Waves. *Math. Comp.*, 31:629–651, 1977.

[9] A. Bayliss and E. Turkel. Radiation Boundary Conditions for Wave-Like Equations. *Comm. Pure Appl. Math.*, 33:707–725, 1980.

[10] R. L. Higdon. Numerical Absorbing Boundary Conditions for the Wave Equation. *Math. Comp.*, 49:65–90, 1987.

[11] K. W. Thompson. Time Dependant Boundary Conditions for Hyperbolic Systems. *J. Comput. Phys.*, 68:1–24, 1987.

[12] S. K. Lee T. Colonius and P. Moin. Boundary Conditions for Direct Computation of Aerodynamic Sound Generation. *AIAA Journal*, 31:1574–1582, 1993.

[13] S. Ta'asan and D. M. Nark. An Absourbing Buffer Zone Technique for Acoustic Wave Propagation. 1995.

[14] K. Mazaheri and P. L. Roe. Numerical Wave Propagation and Steady-State Solutions: Soft Wall and Outer Boundary Conditions. *AIAA Journal*, 35:965–975, 1997.

[15] J. B. Freund. Proposed Inflow/Outflow Boundary Conditions for Direct Computation of Aerodynamic Sound. *AIAA Journal*, 35:740–742, 1997.

[16] D. Givoli. Non-Reflecting Boundary Conditions. *J. Comput. Phys.*, 94:1–29, 1991.

[17] R. Courant. Variational methods for the solution of problems and vibrations. *Bull. Amer. Math*, 49:1–23, 1943.

[18] A. K. Bahrani P. L. Alett and O. C. Zienkiewicz. Application of finite elements to the solution of Helmholtz's equation. *Proc. IEEE*, 115:1762–1766, 1968.

[19] G. E. Karniadakis and R. D. Henderson. *The handbook of fluid dynamics.* CRC press, 1998. chapter 29, spectral element methods for incompressible flows.

[20] Cockburn and Shu. Runge-Kutta Discontinuous Galerkin Methods for Convection-Dominated Problems. *Jour. of Scien. Computing*, pages 173–261, 2001.

[21] O. C. Zienkiewicz and K. Morgan. *Finite elements and approximation.* Dover, 2006.

[22] C. B. Quillen I. Lomtev and G. E. Karniadakis. Spectral/hp methods for viscous compressible flows on unstructured 2D meshes. *J. Comput. Phys.*, 144:325–357, 1998.

[23] O. Hassan K. Morgan and J. Peraire. An unstructured grid algorithm for the solution of the Maxwell equations in the time domain. *J. Numer. Methods Fluids*, 19:849–863, 1994.

[24] H. O. Kreiss and J. Olinger. Methods for the Aprroximate Solution of Time-Dependant Problems. *GARB Publ. Ser.*, 10:569–638, 1973. GARB Geneva.

[25] S. J. Sherwin and G. E. Karniadakis. A new triangular and tetrahederal basis for high-order finite element methods. *Int. J. Num. Meth. Eng.*, 38:3775–3802, 1995.

[26] G. karniadakis B. Cockburn and C-W. Shu. The development of discontinuous Galerkin methods. 11, 2000.

[27] A. T. Patera. A spectral method for fluid dynamics: Laminer flow in a channel expansion. *J. Comput. Phys.*, 54:468, 1984.

[28] E. T. Bullister G. E. Karniadakis and A. T. Patera. A spectral element method for soluion of two- and three-dimensional time-dependent equations. page 803, 1985. Proc. Europe-U.S. Conf. on Finite element methods for nonlinear problems.

[29] H. Atkins and C. W. Shu. A quadrature free implementation of the discontinuous Galerkin method for hyperbolic equations. *AIAA J.*, 36:775–782, 1998.

[30] C. A. Balanis. *Advanced Engineering Electromagnetics*. J. Wiley and Sons, 1989.

[31] F. Bassi and S. Rebay. A high-order accurate discontinuous finite element method for the numerical solution to the compresible Navier-Stokes equations. *J. Compu. Physics*, 131:267–279, 1997.

[32] M. Delfour and F. Trochu. Discontinuous Galerkin methods for ordinary differential equations. *Math. Comp.*, 36:455–473, 1981.

[33] W. H. Reed and T. R. Hill. Triangular mesh methods for the neutron transport equation. 1973. Tech. Rep. LA-UR-73-479 Los Alamos scientific lab.

[34] P. LeSaint and P. A. Raviart. On a finite element method for solving the neutron transport equation. *Academic press*, pages 89–145, 1974.

[35] D. Estep and D. French. Global error bounda and global error control approximation for ODE's. *RAIRO, Anal. Numer*, 28:815–852, 1994.

[36] K. Bottcher and R. Rannacher. Adaptive error control in solving ODE's by the DG method. 1996. Tech. report, Uni. Heidelberg.

[37] C. Johnson and J. Pitkaranta. An analysis of the discontinuous Galerkin method for a scalar hyperbolic equation. *Math. Comp.*, 46:1–26, 1986.

[38] T. Peterson. A note on the convergence of the discontinuous Galerkin method for a scalar hyperbolic equation. *SIAM J. Numer. Anal*, 28:133–140, 1991.

[39] N. Yan Q. Lin and A. H Zhou. An optimal error estimate for the discontinuous Galerkin method. *J. Engin. Math.*, 13:101–105, 1996.

[40] G. Jiang and C. W. Shu. On cell entropy inequality for discontinuous Galerkin methods. *Math. Comput.*, 62, 1994.

[41] B. Cockburn and C. W. Shu. TVB Runge-Kutta local projection discontinuous Galerkin finite element method for scalar conservation laws III. *J. Comp. Phys.*, 84:90–113, 1989.

[42] B. Cockburn and C. W. Shu. The Runge-Kutta local projection discontinuous Galerkin finite element method for scalar conservation laws IV. *Math. Comput.*, 54:545–581, 1990.

[43] B. Cockburn and C. W. Shu. The local discontinuous Galerkin method for time-dependant convection diffusion systems. *SIAM J. Numer. Anal.*,, 35:2440–2463, 1998.

[44] T. C. Warburton and G. E. Karniadakis. A discontinuous Galerkin method for the viscid MHD equations. *J. Comput. Phys*, 152:1–34, 1999.

[45] T. Warburton. Application of the discontinuous Galerkin method to Maxwell's equations using unstructured polymorphic hp-finite elements. *J. Comput. Phys.*, 1999.

[46] S. L. Woodruff D. A. Kopriva and M. Y. Hussaini. Discontinuous spectral element approximation of Maxwell's equations. 2000. Proceedings of the international symposium on DG methods.

[47] J. Hesthaven and T. Warburton. High-order accurate methods for time-domain electromagnetics. *Comp. Mod. Engin. Sci.*, 5:395–408, 2004.

[48] K. S. Bey J. T. Oden and A. Patra. a parallel hp-adaptive discontinuous galerkin method for hyperbolic conservation laws. *Appl. Numer. Math.*, 20, 1996.

[49] K. S. Bey and J. T. Oden. hp-version discontinuous Galerkin methods for hyperbolic conservation laws. *Comput. Methods Appl. Mech. Engrg*, 133:259–286, 1996.

[50] C. P. A. Blom. *Method for computational Aeroacoustics*. University of Twents, P.O. Box 217 NL 7500 AE Enschede.

[51] H. Atkins A. Baggag and D. Keyes. Parallel implementation of the discontinuous Galerkin method. *Nasa internal report*, 1999. Contract NAS1-97046.

[52] G. Chavent and G. Salzano. A FEM for the 1D water flooding problem. *J. Comput. Phys.*, 45:307–344, 1982.

[53] B. Cockburn and C. W. Shu. The Runge-Kutta local projection P^1-discontinuous Galerkin method for scalar conservation laws. *Math. Anal. Numer.*, 25:337–361, 1991.

[54] B. Cockburn and C. W. Shu. TVB Runge-Kutta local projection discontinuous Galerkin finite element method for scalar conservation laws II. *Math. Comp.*, 52, 1989.

[55] Y. Du S. J. Sherwin T. C. Warburton, I. Lomtev and G. E. Kariadakis. Galerkin and discontinuous Galerkin spectral/hp methods. *Comput. Methods Appl. Mech. Eng.*, 175:343–359, 1999.

[56] J. S. Hesthaven and D. Gottlieb. Stable spectral methods for conservation laws on triangles with unstructured grids. *Comput. Methods Appl. Mech. Eng.*, 175:361–381, 1999.

[57] K. D. Devine and J. E. Flaherty. Parrallel adaptive hp-refinement techniques for conservation laws. *Appl. Numer. Math.*, 20:367–386, 1996.

[58] J. S. Heathaven and T. Warburton. High-order/spectral methods on unstructured grids I. Time-domain solution of Maxwell's equations. NASA contract NAS1-97046.

[59] A. T. Patera. A spectral method for fluid dynamics. *J. Comput. Phys.*, 54, 1984.

[60] R. D. Henderson and G. E. Karniadakis. Unstructured spectral element methods for simulation of turbulent flows. *J. Comput. Phys*, 122:191–217, 1995.

[61] T. J. Barth and P. O. Frederickson. 1990. Unpublished AIAA Paper No. 90-0013.

[62] A. Harten and S. R. Chakravarthy. Multi-dimensional ENO schemes for general geometries. 1991. ICASE report No. 91-76.

[63] M. Dubiner. Spectral methods on triangles and other domains. *J. Sci. Comput.*, 6:345–390, 1991.

[64] C. Johnson. Numerical Solution of Partial Differential Equations by the Finite Element Method. *Cambridge University Press*, 1987.

[65] Jue Yan and Chi-Wang Shu. Local Discontinuous Galerkin Methods for partail differential equations with higher-order derivatives. *J. Sci. Comput.*, 17(1-4):27–47, 2002.

[66] P. R. M. Lyra and K. Morgan. A Review and comparative study of upwind biased schemes for compressible flow computation. Part one: 1-D first-order schemes. *Archives of computational methods in engineering*, 7:19–55, 2000.

[67] P. L. Roe. Approximate Riemann solvers, parameter vectors and difference schemes. *J. Comp. Physics*, 43:357–372, 1981.

[68] S. K. Godunov. A difference scheme for the numerical computation of discontinuous solutions of hydrodynamic equations. *Math. Sbornik*, 47:271–306, 1959.

[69] S. Osher. Numerical solution of singular pertubation problems and hyperbolic systems of conservation laws. *Holland Mathematical Studies*, 47:179–205, 1981.

[70] P. D. Lax A. Harten and B. van Leer. On Upstream differencing and Godunov-type schemes for hyperbolic conservation laws. *SIAM Review*, 25:35–61, 1983.

[71] J. L. Steger and R. F. Warming. Flux vector splitting of the inviscid gasdynamic equations with application to finite-difference methods. *Journ. of Comput. Phys.*, 40:263–293, 1981.

[72] B. van Leer. Flux-vector splitting for the Euler equations. *Lecture notes in Physics*, 170:507–512, 1982.

[73] B. Cockburn. Discontinuous Galerkin methods for convection dominated problems. 9:69–224, 1994.

[74] G. E. Karniadakis and S. J. Sherwin. Spectral/hp element methods in CFD. 1999. Oxford University Press.

[75] I. A. Abramowitz and I. A. Stegun. *Handbook of Mathematical Functions with Formulas, Graphs and Mathematical Tables*. Dover, 1964.

[76] K. W. Thompson. Time dependant boundary conditions for hyperbolic systems. *J. Comput. Phys.*, 68:1–24, 1987.

[77] A. Mohammadian V. Shankar, W. F. Hall and C. Rowell. Theory and application of time-domain electromagnetics using CFD techniques. 1993. Course notes, University of California.

[78] J. S. Hesthaven. On the analysis and construction of PML's for the linearized Euler equations. *J. Comput. Phys.*, 142:129–147, 1998.

[79] A. Taflove S. C. Hagness. *The electrical Engineer Handbook*, volume 9. Elsevier Academic Press, 2005.

[80] K. Morgan J. Peraire, M. Vahdati and O. C. Zienkiewicz. Adaptive remeshing for compressible flow computations. *J. Compt. Phys.*, 72:449–66, 1987.

[81] S. Abarbanel and D. Gottlieb. A Mathematical Analysis of the PML Method. *J. Comput. Phys.*, 3:357–363, 1996.

[82] B. Yang. *Spectral methods and absorbing boundary conditions for Maxwell's equations.* Phd thesis, Brown University, May 1998.

[83] K. Morgan and J. Peraire. Unstructured grid finite-element methods for fluids. *Rep. Prog. Phys.*, 61:569–638, 1998.

[84] J-P Berenger. A perfectly matched layer for the absorption of EM waves. *Computational Physics*, 114:185–200, 1994.

[85] Armel de La Bourdonnaye. Sur le probleme de Cauchy pour le system de Berenger. *Numerical Analysis*, 322:285–288, 1996.

[86] P. Zhang T.LU and W. Cai. Discontinuous Galerkin methods for dispersive and lossy Maxwell's equations and PMl boundary conditions. *J. Comput Phys.*, 200:549–580, 2004.

[87] J. S. Hesthaven and C. H. Teng. Stable spectral methods on tetrahedral elements. *SIAM J. Sci. Comput.*, 21(6):2352–2380, 1999.